Master's thesis

NTNU
Norwegian University of Science and Technology
Faculty of Engineering
Department of Energy and Process Engineering

Einar Aasli

Numerical Simulation of Fluid-Structure Interaction

Numerisk simulering av fluid-struktur interaksjon

Master's thesis in Energy and Environmental Engineering
Supervisor: Bernhard Müller
June 2021

NTNU
Norwegian University of Science and Technology

Einar Aasli

Numerical Simulation of Fluid-Structure Interaction

Numerisk simulering av fluid-struktur interaksjon

Master's thesis in Energy and Environmental Engineering
Supervisor: Bernhard Müller
June 2021

Norwegian University of Science and Technology
Faculty of Engineering
Department of Energy and Process Engineering

NTNU
Norwegian University of
Science and Technology

NTNU

Norwegian University
of Science and Technology

Department of Energy
and Process Engineering

EPT-M-2021-

MASTER THESIS

for

Student Einar Aasli

Spring 2021

Numerical Simulation of Fluid-Structure Interaction

Numerisk simulering av fluid-struktur interaksjon

Background and objective

The simulation of fluid-structure interaction (FSI) is not only important for flutter of wings and for flow-induced vibrations in power plants, but also for the flapping motion of the soft palate in the human pharynx. During sleep, the soft palate can make contact with the pharynx wall and lead to obstructive sleep apnea (OSA). Also the sound generated by FSI, e.g. FSI of the inhaled air and the soft palate causing snoring, can be of interest. Because of its great importance for public health, OSA has been investigated in a larger interdisciplinary research project entitled "Virtual Surgery in the Upper Airways - New Solutions to Obstructive Sleep Apnea Treatment (VirtuOSA)", which is funded by the Research Council of Norway.

The objective of the master thesis is to reduce an existing immersed boundary method (IBM) for FSI from higher to lower order. Thereby, the IBM approach will also become applicable for non-convex structures. The 2D compressible Navier-Stokes equations model fluid flow including acoustics and heat transfer, while flexible plates are modeled by the Euler-Bernoulli thin beam theory. The new IBM for FSI is to be verified for a FSI benchmark problem. The master thesis will be a part of VirtuOSA.

The following tasks are to be considered:

1. to get a basic understanding of FSI, its mathematical description and its numerical simulation using IBM,
2. to develop and implement a lower order IBM for FSI that is applicable for both convex and non-convex structures,
3. to verify the new IBM for FSI by applying it to a FSI benchmark problem,
4. to investigate the transfer of energy between fluid and structure for an FSI benchmark problem.

-- " --

Within 14 days of receiving the written text on the master thesis, the candidate shall submit a research plan for his project your supervisor.

When the thesis is evaluated, emphasis is put on processing of the results, and that they are presented in tabular and/or graphic form in a clear manner, and that they are analyzed carefully.

The thesis should be formulated as a research report with summary in English, conclusion, literature references, table of contents etc. During the preparation of the text, the candidate should make an effort to produce a well-structured and easily readable report. In order to ease the evaluation of the thesis, it is important that the cross-references are correct. In the making of the report, strong emphasis should be placed on both a thorough discussion of the results and an orderly presentation.

The candidate is requested to initiate and keep close contact with his academic supervisor throughout the working period. The candidate must follow the rules and regulations of NTNU as well as possible directions given by the Department of Energy and Process Engineering.

Risk assessment of the candidate's work shall be carried out, in cooperation with the supervisor, according to the department's procedures. The risk assessment must be documented and included as part of the final report. Events related to the candidate's work adversely affecting the health, safety or security, must be documented and included as part of the final report. If the documentation on risk assessment represents a large number of pages, the full version is to be submitted electronically to the supervisor and an excerpt is included in the report. Those who have a theoretical exercise only need to check this and fill out page 1 of the form provided by the Department of Energy and Process Engineering.

Pursuant to “Regulations concerning the supplementary provisions to the technology study program/Master of Science” at NTNU §20, the Department reserves the permission to utilize all the results and data for teaching and research purposes as well as in future publications.

The master's thesis is to be submitted in NTNU’s examination system Inspera Assessment by 14:00 h on June 11, 2021.

☐ Work to be done in lab (Water power lab, Fluids engineering lab, Thermal engineering lab)
☐ Field work

Department of Energy and Process Engineering, January 12, 2021

_____

Bernhard Müller
Academic Supervisor

Abstract

In this master thesis, a higher order ghost point immersed boundary method (GPIBM) designed for compressible flows and fluid-structure interaction (FSI) applications is reduced to second order to be able to deal with concave geometries. The new ghost point immersed boundary method uses a second order summation by parts (SBP) finite difference method to calculate the spatial derivatives in the compressible Navier-Stokes equations. To remove dispersed wave modes, a second order explicit low pass filter is applied to the variables solved for in the fluid domain every nth time step. The method is tested on the two 2D FSI test problems: an elastically mounted cylinder and a flexible plate behind a cylinder.

In the first problem, a cylinder attached to a spring and a damper is located in a flow field at Reynolds number $Re = 200$, and Mach number $Ma = 0.25$. The resulting governing equations of the structure thus become two second order ordinary differential equation (ODE) similar to that of a harmonic oscillator with two degrees of freedom. Drag and lift forces exerted by the fluid on the cylinder surface appear as external forces in these ODEs. The classic explicit fourth order Runge-Kutta method (RK4) is both used to solve the system of ODEs numerically, and to preform the time integration in fluid solver. Results are compared to those obtained by Yang and Stern [51], Blackburn and Karniadikis [5], and Ringstad [36] using the original higher order GPIBM. In addition, a study of the energy transfer between the fluid and cylinder is conducted.

In the second problem, a flexible plate made of an elastic and compressible material is attached behind a circular cylinder located in a 2D channel. A simplification of the plate model is preformed by assuming it is an Euler-Bernoulli beam, which displacement is restricted to the lateral direction. The difference in pressure force between the top and bottom of the plate exerted by the fluid deforms the plate. The resulting governing equation for the structure is solved numerically by the use of the implicit Newmark method, while time integration in the fluid solver is preformed using the RK4 method. Simulations are set up in accordance with those of FSI1 ($Re = 20$) and FSI2 ($Re = 100$) presented in the article by Turek and Hron [45]. Results are compared. Instabilities thought to originate from errors in the implementation of the test case and possibly artificial added mass effects occur.

Sammendrag

I denne masteroppgaven blir en høyere ordens ghost point immersed boundary metode (GPIBM) designet for kompressibel strømning og fluid-strukturinteraksjon (fluid-structure in- teraction, FSI) applikasjoner redusert til andre orden for å kunne håndtere konkave geometrier. Den nye ghost point immersed boundary metoden bruker en annen ordens summation by parts (SBP) endelig differansemetode for å approksimere de spatial deriverte i de kompressible Navier-Stokes-ligningene. For å fjerne dispererte bølgemoder filtreres løsningen i fluiddomenet med et eksplisitt lavpassfilter av andre orden hvert $n - te$ tids skritt. Metoden er testet på de to 2D FSI-testproblemene: en elastisk montert sylinder og en fleksibel plate bak en sylinder.

I det første problemet er en sylinder festet til en fjær og en demper plassert i et strømningsfelt ved Reynolds-tallet $Re = 200$, og Mach-tallet $Ma = 0.25$. De resulterende ligningene for strukturen blir to andre ordens ordinær differensialligning (ODE) lik en harmonisk oscillator med to frihetsgrader. Drag- og lift-krefter som utøves av væsken på sylinderoverflaten inngår som eksterne krefter i ODEene. Løsningen av ODE systemet og tidsintegrasjonen i fluid løseren utføres ved hjelp av den klassiske eksplisitte fjerde ordens Runge-Kutta-metoden (RK4). Resultatene sammenlignes med resultater oppnådd av Yang og Stern [51], Blackburn og Karniadikis [5], og Ringstad [36] ved bruk av den opprinnelige høyere ordens GPIBM. Det gjennomføres også en studie av energioverføringen mellom fluidet og sylinder.

I det andre problemet er en fleksibel plate laget av et elastisk og kompressibelt materiale festet bak en sirkulær sylinder lokalisert i en 2D kanal. En forenkling av platemodellen er foretatt ved å anta den er en Euler-Bernoulli bjelke begrenset til å bare kunne bevege seg i lateral retning. Forskjellen i trykkraft mellom toppen og bunnen av platen som utøves av væsken, deformerer platen. Den resulterende ligningen for strukturen løses numerisk ved bruk av den implisitte Newmark-metoden, mens tidsintegrering i fluid-løseren blir foretatt ved hjelp av RK4-metoden. Simuleringer er satt opp i samsvar med FSI1 ($Re = 20$) og FSI2 ($Re = 100$) presentert i artikkelen av Turek og Hron [45]. Resultatene blir sammenlignet. Ustabiliteter som antas å være forårsaket av feil i oppsettet av test problemet og muligens også kunstige added-mass-effekter oppstår.

Acknowledgments

First of all I would like to express my sincere gratitude to my supervisor Professor Bernhard Müller for his continuous support and guidance. He has dedicated much time for our weekly meetings and provided valuable feedback on my work. His vast knowledge of CFD has both been of great help and inspiration. The help of PhD student Frederik Kristoffersen, who is currently working on extending the higher order ghost point immersed boundary method to 3D, has also been very appreciated.
I would like to extend my gratitude to PhD student Knut Emil Ringstad for providing me with his FSI codes for an elastically mounted cylinder and a flexible plate behind a cylinder. His codes have served as a framework for my own implementations.
The FSI codes where run on the IDUN/EPIC high performance computing cluster [40] at NTNU. Thanks to Johan Floan for holding his course on parallel computing, despite of Corona restrictions and that I was the only participant. The help by senior engineer Jan Christian Meyer at the NTNU HPC group in running the present code on the HPC cluster has also been much appreciated.

Table of Contents

List of Figures

List of Tables

List of symbols and abbreviations

Symbols

ρ_f	=	Fluid mass density
μ	=	Dynamic fluid viscosity
ν	=	Kinematic fluid viscosity
τ_{ij}	=	Viscous stress tensor
γ	=	Ratio of specific heats
κ	=	Heat conduction coefficient
t	=	Physical time
t'	=	Nondimensional time
x, y	=	Cartesian coordinates in physical domain
ξ,η	=	Transformed coordinates in computational domain
E	=	Specific total energy
H	=	Total entalpy
p	=	Pressure
S_c	=	Sutherland constant
T	=	Temperature
$\boldsymbol{U}$	=	Vector of conservative variables
St	=	Strouhal number
ρ_s	=	Structure mass density

Abbreviations

BC	=	Boundary condition
GP	=	Ghost-point
IP	=	Image point
BI	=	Body intercept
ODE	=	Ordinary differential equation
CFD	=	Computational fluid dynamics
IB	=	Immersed boundary
IBM	=	Immersed boundary method
OSAS	=	Obstructive sleep apnea syndrome
SBP	=	Summation by parts
FSI	=	Fluid-structure interaction
PDE	=	Partial differential equations

1 Introduction

Obstructive Sleep Apnea (OSA) is a disease caused by the collapse of the the soft palate onto the pharynx wall during sleep, which obstructs the airflow as illustrated in figure 1. The condition is recognised by heavy snoring and frequent awakening which patients experience [21]. Clinical research has found that its not only the sleep of the patient and their partner that is effected by OSA. Neurological and cardiovascular complications are also observed in patients, significantly reducing life quality [29]. It is estimated that OSA is effecting around 20% of the adult population (50+) [41], many whom are of not diagnosed. Obesity is the most important risk factor of OSA, and a weight gain of only 10% can increase the risk of development as much as six times [29]. Increasing age is also a risk factor, with a prevalence three times as high for older persons (65+) than middle aged person (30-64) [29]. With older and more obese population, the prevalence of OSA is thought to be an increasing health problem. Today, treatment of OSA mainly consists of weight loss and Continuous positive airway pressure (CPAP) and in some cases also surgery. CPAP treatment involves the use of a sleeping mask that assures continuous airflow through the upper airways by increasing the pressure of air to a higher level than the surrounding atmospheric and has proven to be an effective treatment option. However, the use of the mask is poorly tolerated by patients and is no final cure for the condition [29]. Surgery treatment has been applied successfully, but remains controversial due to its lack of standardized criteria to assess whether a specific surgical intervention will be successful. The rate of success for a procedures relies much upon the specific patient and experience of the surgeon [29].

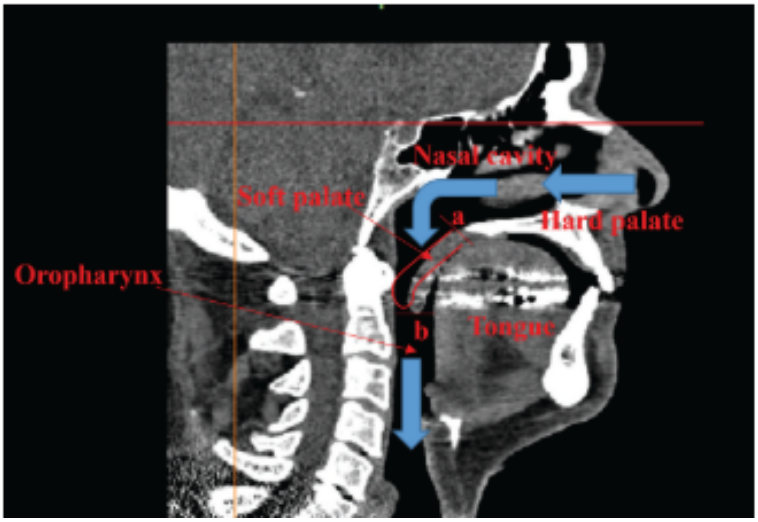

Figure 1: CT image of the upper human airways. "a" and "b" marks the start and end of the soft palate respectively. A schematic depiction of the position of the soft palate during collapse is depicted by the red circumferences, as well as the airflow (blue) [26].

OSA is a major growing health concern [22]. Since there are significant differences between the airways of difference patients and flow in the upper airways is complicated with many difficult features to take into account [17] [25], one lacks sufficient tools to assess which treatment is right, and how surgery should be performed for each specific patient. Due to this, the Norwegian Research Council has granted funding to the research project: *Virtual Surgery in the Upper Airways - New Solutions to Obstructive Sleep Apnea*, also known as VirtuOSA. VirtuOSA is a multidisciplinary collaboration project between The Norwegian University of Science and Technology (NTNU), St. Olavs Hospital and SINTEF Industry. The project aims at developing a software tool that can be

used in diagnostic of OSA and treatment through virtual surgery [14]. VirtuOSA is a continuation of the research project OSASMOD-Modeling of Obstructive Sleep Apnea by Fluid-Structure Interaction in the Upper Airways (2014-2017), which aimed at demonstrating the potential of such a software tool for finding the risk of OSA and predict response of surgery [21].

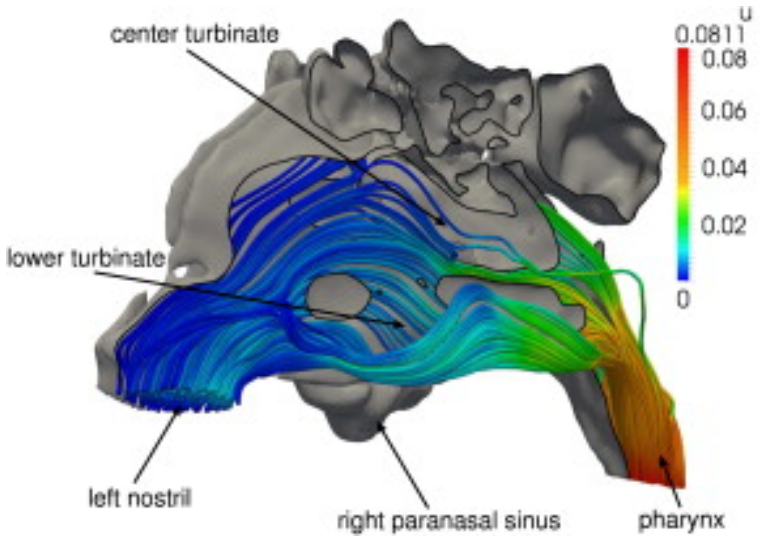

Figure 2: Streamlines in the nasal cavity colored by the velocity magnitude. [24]

The idea behind the software tool is that the geometry of the upper airways of the patient can be obtained through the use of different medical imaging techniques such as Computer Tomography (CT) and Magnetic Resonance Imaging (MRI) [21]. The geometry can then be used to conduct flow simulations, and it can be altered to see the result of surgical interventions (virtual surgery). However, simulating the flow in the upper airways is by no means a trivial task. The flow will interact with the moving and deforming tissue creating a problem of fluid-structure interaction (FSI) [25]. In fluid-structure interaction problems, the governing equations of both the fluid and the solid need to be solved in the same simulation. Even tough the governing equations of both fluid and structure together make up the field of continuum mechanics and their governing equations only differ by their constitutive models, the deformation pattern of fluids and solids are so different that the governing equations are solved in different frames of reference. Stresses in fluids are related to and usually proportional to the rate of deformation experienced by the fluid and can undergo large deformations. Their governing equations are thus described in an Eularian frame of reference where the solution variables such as the velocity are field variables corresponding to the velocity at one point at a certain time. Solids, however, do not undergo large deformations and the stresses are functions of and usually proportional to the deformation itself. This makes it more suitable to describe the governing equations in a Lagrangian frame of reference where one follows the deforming solid itself, and the variable solved for, such as the deformation, is described in terms of a reference configuration [18]. The most reliable approach to an FSI simulation is to reformulate the governing equations for fluid and structure into the same frame of reference and use one solver for both fluid- and solid domain. This is known as the monolithic approach and is unconditionally stable. Despite this, computational fluid dynamics (CFD) and computational solid mechanics (CFM) are distinct fields with sophisticated numerical algorithms developed for their own respective purpose. To utilize software modularity, the so called partitioned approach where distinct solvers for the fluid- and solid domain coupled trough boundary conditions (BCs) is thus often preferred [42].

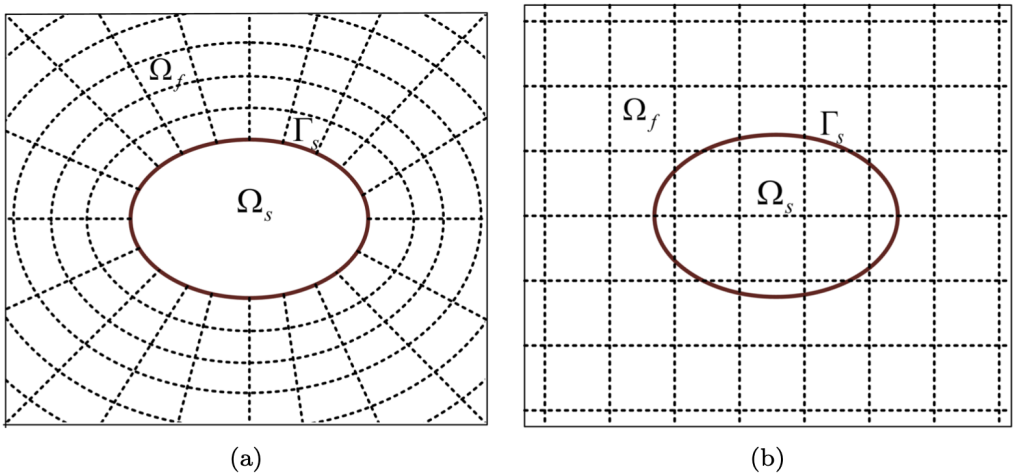

Figure 3: a) Body-conforming grid. b) Cartesian non-conforming grid used in immersed boundary methods [15].

The classical approach in CFD is to use a so called body-conforming grid. Body-conforming grids conform around the structural surface as illustrated in figure 3 a). This allows the grid to align with the flow field and good resolution of the boundary layer due to the possibility of grid clustering in the vicinity of the body [31]. However, the meshing process itself is cumbersome, especially for advanced geometries, and in an FSI simulation, a re-meshing is required for each kinematic change of the structure. A re-meshing algorithm able to take into account arbitrary deformations is difficult to develop, and would be very slow. The re-meshing approach to an FSI-problem is thus often limited to smaller deformations where a robust and fast re-meshing algorithm can be used. For flows in the uppers airways however, one has to be able to account for larger unforeseen deformations of complex tissue. Since no human body is equal, the software tool needs to be applicable to different airway profiles without the need for manual meshing.

There are alternatives to the body conforming. Immersed Boundary (IB) methods first introduced by Peskin in 1972 [34] is a group of methods which make use of a non-conforming Cartesian background grid on which the solid body is allowed to freely move and deform upon (see figure 3 b)). In IB methods, the grid lines simply extends through the boundary. This means that the grid is fixed, and no re meshing is needed. The coupling between the fluid and the grid is accomplished by imposing the boundary conditions on Cartesian grid points adjacent to the immersed boundary. It is how these boundary conditions are incorporated, and as a consequence the effect the solid and fluid have on each other, which constitutes the difference between the IB methods [31].

There are two main categories of IB methods. In the first one, *diffused interface methods*, the boundaries are smeared by distributing singular forces to the surrounding grid points approximating the effect the solid has on the fluid. In the other category, *sharp interface method*, the effect the solid has on the fluid is restricted only to the computational nodes close to the boundary, avoiding the nonphysical smearing effects occurring for the diffused approach [42] [2]. Nodes, volumes or elements (dependent on which CFD method is used) outside the immersed boundary are part of the fluid domain where the governing equations of the fluid are solved, and the ones inside makes up the solid domain where the governing equations of the solid can be solved with any appropriate method.

Inside the category of sharp interface methods there are several worth mentioning which could be relevant for the virtuOSA project, each with their strengths and weaknesses. The cut-cell method for instance is a method where fluid cells cut by the boundary are reshaped according to the local geometry of the interface, creating a body conforming unstructured grid at the interface [42]. This method is conservative and has good accuracy close to the boundary. However, it has proven to be difficult to extend it to complex 3 dimensional geometries due to the many possibilities of the geometrical shape of the cut cells that may arise [42]. Despite this, cut-cell methods have been developed for 3D flows by for example Schneiders et al. [37]. Another type of methods are hybrid Cartesian-immersed boundary methods [42]. In these methods, the force exerted by the solid on the fluid is calculated implicitly by imposing the boundary conditions on the immersed boundary. This is done by reconstructing the velocity, pressure etc. at grid nodes close to the immersed boundary. To do this reconstruction, an interpolation procedure taking into account the boundary conditions on the immersed boundary is used. An example of such hybrid Cartesian-immersed boundary method for compressible flow can be found in Luo et al. [27]. A problem arising for hybrid Cartesian methods are non physical force oscillations at the boundary. More on these nonphysical oscillations later.

In his PhD thesis, associated to the OSASMOD project, E.Khalili [15] together with M.Larsson and B.Müller developed a higher order IB method: Ghost-Point immersed boundary method (GPIBM) for or stationary and moving bodies [9]. The method is a finite difference method in which points in the calculation domain either is defined as fluid, soild or ghost-points. Ghost points are points inside the boundary of the structure close to the boundary used in the finite difference stencil of any of the fluid points. Their values are set by extending a normal probe through the immersed boundary into an image point (IP) in the the fluid domain, and then utilize the boundary condition along this line to get an expression for the value at the ghost point. It is in this way the boundary conditions are imposed for the fluid, and thereby also the effect the structure has on the fluid. The effect the fluid has on the structure is imposed by including the traction from the fluid on the structure in the structural equations. In literature, there exists several Ghost-Cell finite volume methods developed for 2D and 3D simulations. Such methods have been regarded difficult to extend from 2D to 3D for complex geometries [31] because of the challenge of tracking the boundary correctly [28]. To overcome this methods using triangular surface meshes and level set methods have been developed [28]. An example of the first is found in Luo et al. [28] where a ghost-cell immersed boundary method is used for compressible flows, and an example of the latter see Uddin et al.[46] where a level set method is used together with a higher order finite difference method to simulate compressible flow. The flexibility and simplicity of the finite difference IB method makes it suitable for the VirtuOSA project. A more detailed description of the GPIBM is found in section 3.2 [2].

The flow in the upper human airways has been found to be in the weakly compressible flow regime [4]. For flows of such low Mach numbers, these flows can be modelled as incompressible, which allows for larger time steps since the CFL condition is only restricted by the fluid velocity and not the fluid velocity plus the speed of sound. However, there are several benefits to model the flow as compressible. With a compressible solver, the acoustics of the snoring can be studied as well as the heating of the inhaled air. Also, a compressible solver avoids the costly process of solving an elliptical equation for the pressure [35]. In order to have some flexibility, the immersed GPIBM method by Khalili et al. is constructed for compressible flows. It is worth mentioning that most IB algorithms are constructed for incompressible flows, hence the need to construct a new method for the VirtuOSA project. Other examples of IB methods used for compressible flows besides those already mentioned can for instance be found in Chauduri et al. [7], where a ghost cell method is used for shock predictions in the supersonic regime, Ghias et al. [11], where a ghost cell method is used to simulate the flow around a 3D rigid wing at high Reynolds number, or Wang et al. [49], where different interface methods for embedded boundary methods used for FSI applicationns is investigated.

For loose coupling methods for FSI applications, methods where the fluid and structural parts are solved sequentially, a phenomena called the artifcial added mass effect often occurs. The artificial added mass effect is recognised by spikes and oscillations in the traction exerted on the solid by the fluid due to incompatibility of the kinematic and dynamic quantities at the fluid-structure interface [42] [18] [6]. It is these effects that create spurious oscillations for the already mentioned hybrid Cartesian methods. The phenomena seems to be more pronounced for low solid-fluid mass density ratio and slender structures which may be encountered in upper airway flow-simulations [18]. Also, a higher Reynolds number seems to increase this artficial numerical effects [18]. To deal with the artificial added mass effect, subiteration methods where the fluid and structure are solved sequential within each time step until a convergence criteria is met are often used for partitioned FSI algorithms, giving a strong coupling [42]. For compressible flow solvers, Van Brummelen [47] showed that the added mass effct was proportional to the time step used in the subiteration process, while it was only reducible to a threshold value when the time step in the subiteration procedure is lowered for incompressible solvers. Thus, even tough more physics has to be modelled and solved numerically for compressible flow solvers, they seems to be a slight advantage over incompressible solvers for FSI applications for certain coupling methods. Note that no sub-iteration method is used in the GPIBM by Khalili et al. [9], and it is consequently susceptible to this phenomena.

Turbulence is a major challenge in CFD. For direct numerical simulations of turbulent flows, extremely high grid resolution and extremely small time steps are needed, if not instead introducing turbulence modelling in the form of a quite accurate but still very computationally expensive Large Eddy Simulation (LES), or a comparably significantly less computationally expensive but still potentially inaccurate Reynolds Averaged Navier Stokes Simulation (RANS) [35]. The airflow in the upper airways is estimated to be in the laminar to transitional flow regime [24], meaning that intuitively the computational tool developed in the VirtuOSA project needs to be able to in some degree take into account turbulence. However, Aasgrav et al [1]. found that turbulence did not have any impact on the airflow in the upper airways of an OSA patient. Consequently, the flow solver only needs to tackle laminar flow.

The ghost point immersed boundary method developed by Khalili et al. [9] was implemented with a globally fourth order Summation By Parts (SBP) method using a sixth order finite difference stencil in the interior domain which developed into a third order one-sided difference method at the boundary. A SBP operator is a finite difference operator such that the energy of a hyperbolic system is bounded by the initial conditions, thereby assuring stability. In the master thesis of K.Ringstad [36], the globally fourth order SBP method was tested for two FSI test cases: elastically mounted cylinder at $Re = 200$ and $Ma = 0.25$ (case a)) and a flexible plate behind a cylinder (case b)) with parameters adjusted according to FSI1 and FSI2 described in the benchmark paper by Turek and Hron [45]. For case a), the method showed very good results. However, for method b) it was found that for concave geometries, the computational stencil required to approximate the derivatives of the viscous fluxes in the compressible Navier-Stokes equations would often extend beyond the available fluid or ghost nodes [36].

In this master thesis, the globally fourth order SBP method is changed to a second order SBP method. The method is tested on the same test cases, case a and b, as Ringstad did in his master thesis. The elastically mounted cylinder is modelled as a mass-spring-damper system which results in a second order ODE. The fourth order classic Runge-Kutta method (RK4) is used to solve the ODE as well as for the time marching in the fluid solver. Displacement, drag, lift and energy exchange is studied and compared with results obtained by Ringstad using the globally fourth order SBP method, Yang and Stern [51] and Blackburn and Karniadakis [5]. For case b, flexible plate behind a cylinder, simulations using FSI1 (Re=20) and FSI2 (Re=100) parameters are preformed. The plate is modelled as an Euler-Bernoulli beam with finite thickness. The resulting differential equation for the plate displacement is solved using the implicit Newmark method, while the time marching for the fluid is done using the RK4 method. Tip-displacement is studied and comapred

with benchmark results provided by Turek and Hron in [45]. In addition, a study of plate movement, pressure difference along plate and energy transfer between plate and fluid is investigated.

The thesis is built up the following way. In chapter 2 the governing equations for the fluid, the compressible Navier-Stokes equations, and the governing equations for the structure in cases a and b, namely the equation for the mass-spring-damper system and the Euler-Bernoulli beam equation for the plate, are presented. In chapter 3 the ghost point immersed boundary method developed by Khalili et al. [9] and the methods used to discretize the governing equations prsented in chapter 2 for both fluid and structure are presented. Results from the simulations of the taste cases are presented and discussed in chapter 4. At last, conclusions are drawn in 5 and suggestions on future work that should be done but the author did not have time for or is beyond the scope of this thesis are presented in chapter 6.

2 Governing equations

In this chapter, the governing equations of the fluid and structure are presented. First, the compressible Navier-Stokes equations governing the behaviour of the fluid are presented in section 2.1, and a non dimensional perturbation form in transformed coordinates are deduced in section 2.2 and 2.3. Then, the equations for the mass-springer-damper system representing the governing equations for the structure in the elastically mounted cylinder test case are presented in section 2.4. At last, the simplification of the elastic compressible material model to an Euler-Bernoulli beam model for the plate in the flexible plate behind a cylinder test case is reasoned for, and the resulting governing equation for the plate is introduced in section 2.5.

2.1 Compressible Navier-Stokes equations

The following section is taken from the authors Project work [2]. The fluid is as compressible and the problem is solved in two dimensions. Hence the conservation of mass, momentum and energy is stated through the compressible Navier-Stokes equations in an Eulerian frame of reference:

$$\frac{\partial \rho}{\partial t} + \frac{\partial}{\partial x_j}\left[\rho u_j\right] = 0, \tag{1}$$

$$\frac{\partial}{\partial t}\left(\rho u_i\right) + \frac{\partial}{\partial x_j}\left[\rho u_i u_j + p\delta_{ij} - \tau_{ij}\right] = 0, \quad i = 1, 2, \tag{2}$$

$$\frac{\partial}{\partial t}\left(\rho E\right) + \frac{\partial}{\partial x_j}\left[\rho u_j E + u_j p + q_j - u_i \tau_{ij}\right] = 0, \tag{3}$$

where ρ, u_1, u_2, p, E are the mass density, x- and y-velocity components, pressure and specific total energy. δ_{ij} is the Kronecker delta, i.e. =1 if i=j, and =0 else.

Equations (1), (2), (3) only account for four equations in total, yet they contain seven unknowns. In order to establish a closed system of equations more relations have to be established. Further, the fluid is modelled as as a perfect gas:

$$p = \rho R T, \tag{4}$$

$$e = c_v T, \tag{5}$$

where $e = E - \frac{1}{2}(u_1^2 + u_2^2)$ is the specific internal energy. R, c_v, T are the gas constant of the fluid, specific heat at constant volume and temperature, respectively. The specific heats at constant volume c_v and the specific heat at constant pressure are both considered constant. Their ratio $\gamma = \frac{c_p}{c_v} = 1.4$ i.e. approximately the same as for air at room temperature and atmospheric pressure. Due to these assumptions, a relation between the variables solved for in the compressible Navier-Stokes equations can be derived:

$$p = (\gamma - 1)(\rho E - \frac{1}{2}\rho(u_1^2 + u_2^2). \tag{6}$$

The stress tensor τ_{ij} is modelled through the constitutive model of a Newtonian fluid with bulk viscosity equal to zero (Stokes' hypothesis) [50]. This relates the stress tensor to the strain rate tensor by the following equation:

$$\tau_{ij} = \mu(\frac{\partial u_i}{\partial x_j} + \frac{\partial u_j}{\partial x_i}) - \frac{2\mu}{3}\frac{\partial u_k}{\partial x_k}\delta_{ij}. \tag{7}$$

.

The dynamic viscosity is temperature dependent and varies according to Sutherland's law $\frac{\mu}{\mu_0} = (\frac{T}{T_0})^{1.5}[(1+S_c)/(\frac{T}{T_0}+S_c)]$, where S_c is the dimensionless Sutherland constant, $S_c = \frac{110}{T_0}$, T_0 is the stagnation temperature and $\mu_0 = \mu(T_0)$.

At last, the heat flux is modelled through Fourier's law

$$q_j = -\kappa \frac{\partial T}{\partial x_j}, \tag{8}$$

where κ is the thermal conductivity of the fluid. In the simulations done in this project, the Prandtl number is assumed constant namely $Pr = 0.72$. This gives the following relation between the viscosity and the thermal conductivity: $\kappa = \frac{c_p \mu}{Pr} = \frac{c_p \mu}{0.75}$ [15] [36].

2.2 Non-dimensionalization and perturbation form

The following section is taken from the corresponding section of the author's project work [2]. In the last subsection a closed form of the governing equations was derived. However, in this project, the equations are solved in a non-dimensional perturbation form. As a starting point the conservative variable $\boldsymbol{U}$ is defined:

$$\boldsymbol{U}(\boldsymbol{x},t) = \begin{pmatrix} \rho(\boldsymbol{x},t) \\ \rho u(\boldsymbol{x},t) \\ \rho v(\boldsymbol{x},t) \\ \rho E(\boldsymbol{x},t) \end{pmatrix}. \tag{9}$$

where $\mathbf{x} = (x,y)^T$, $u = u_1$ and $v = u_2$ in equations (1)-(3).

For low Mach number flows, small changes in the flow variables might lead to cancellation errors. For instance, if the pressure is expressed in perturbation form $p = p_0 + p'$ where p_0 is the base pressure and p' is the perturbation, p_0 might be so much larger than p' that the computer rounds off the pressure to p_0 thus leading to zero pressure gradient [39] [15]. In order to deal with this, the governing equations are solved in perturbation form with respect to a reference stagnation state. The conservative variable $\boldsymbol{U}'$ is expressed in the form:

$$\boldsymbol{U}'(\boldsymbol{x},t) = \boldsymbol{U}(\boldsymbol{x},t) - \boldsymbol{U}_0(\boldsymbol{x},t) \tag{10}$$

where $\boldsymbol{U}_0(\boldsymbol{x},t) = (\rho_0, 0, 0, (\rho E)_0)$ is the stagnation state vector of the fluid.

Using equation (7) the perturbation form of the viscous stress tensor can be derived:

$$\tau' = (\mu_0 + \mu')(\nabla \boldsymbol{u}' + (\nabla \boldsymbol{u}')^T) - \frac{2}{3}(\mu_0 + \mu')\nabla \cdot \boldsymbol{u}' \boldsymbol{I}, \tag{11}$$

where $\boldsymbol{u} = (u,v)^T$, $\mu = \mu_0 + \mu'$ and I is the identity matrix. The full 2D stress tensor is then equal to:

$$\tau'_{ij} = \begin{pmatrix} \tau'_{xx} & \tau'_{xy} \\ \tau'_{yx} & \tau'_{yy} \end{pmatrix} = \mu \begin{pmatrix} \frac{4}{3}\frac{\partial u'}{\partial x} - \frac{2}{3}\frac{\partial v'}{\partial y} & \frac{\partial u'}{\partial y} + \frac{\partial v'}{\partial x} \\ \frac{\partial u'}{\partial y} + \frac{\partial v'}{\partial x} & \frac{4}{3}\frac{\partial v'}{\partial y} - \frac{2}{3}\frac{\partial u'}{\partial x} \end{pmatrix} \tag{12}$$

.

For convenience, the variables of the governing equation are non-dimensionalised using the speed of sound $c_0 = \sqrt{\gamma R T_0}$ as reference velocity, stagnation density ρ_0 as reference density and cylinder diameter D as reference length-scale. The reference scales for the conservative variables in (9) are then non-dimensionalized using with the following: $\rho_0, c_0, c_0, \rho_0 {c_0}^2$. In addition, the reference temperature T_0 is used to nondimensionalize the temperature T and the reference pressure $p_0 = \rho_0 c_0^2$ is used to non-dimensionalize the pressure.

When it comes to the dynamic viscosity and the thermal conductivity, an at first glance not so evident non-dimensionalization can be derived. Using the already defined length, velocity and density scales, the natural scale for the viscosity would be $\rho_0 c_0 D$. By introducing the stagnation Reynolds number $Re_0 = \frac{D c_0 \rho_0}{\mu_0}$, the scale for the viscosity can be rewritten into $Re_0 \mu_0$. For the thermal conductivity, the natural scale would be $\frac{\rho_0 c_0^3 D}{T_0}$. Using the definition of c_0, the derived scale for the viscosity and the Prandtl number, the scale can be rewritten into $(\gamma - 1) Re_0 Pr \kappa_0$, where κ_0 is the stagnation thermal conductivity [15].

Two important non-dimensional numbers characterising the flow are the Reynolds number and the Mach number defined as $Re = \frac{\rho_0 u_0 D}{\mu_0}$ and $Ma = \frac{u_0}{c_0}$. They are related to the stagnation Reynolds number such that $Re = \frac{Re_0}{Ma_0}$.

Now that the governing equation is reformulated in non dimensional perturbation form it can be expressed in the following conservative flux-form:

$$\boldsymbol{U}'_t + \boldsymbol{F}^{c\prime}{}_x + \boldsymbol{G}^{c\prime}{}_y = \boldsymbol{F}^{v\prime}{}_x + \boldsymbol{G}^{v\prime}{}_y, \tag{13}$$

where the subscripts indicates of which variable the derivative is taken with respect to, c stands for convective and v for viscous.

$$\boldsymbol{F}^{c\prime} = \begin{pmatrix} (\rho u)' \\ (\rho u)u' + p' \\ (\rho u)'v' \\ ((\rho H)_0 + \rho H')u' \end{pmatrix} \qquad \boldsymbol{G}^{c\prime} = \begin{pmatrix} (\rho v)' \\ (\rho v)'u' \\ (\rho v)'v' + p' \\ ((\rho H)_0 + \rho H')v' \end{pmatrix} \tag{14}$$

$$\boldsymbol{F}^{v\prime} = \begin{pmatrix} 0 \\ {\tau_{xx}}' \\ {\tau_{xy}}' \\ {\tau_{xx}}'u' + {\tau_{xy}}'v' + \kappa T'_x \end{pmatrix} \qquad \boldsymbol{G}^{v\prime} = \begin{pmatrix} 0 \\ {\tau_{yx}}' \\ {\tau_{yy}}' \\ {\tau_{yx}}'u' + {\tau_{yy}}'v' + \kappa T'_y \end{pmatrix} \tag{15}$$

where $((\rho H)_0 = (\rho E)_0 + p_0/\rho_0 c_0^2$ is the nondimensional stagnation total enthalpy per unit volume. Note that variables are now non-dimensional. $u' = \frac{u}{c_0} = \frac{(\rho u)'}{(\rho_0 + \rho')}$, $v' = \frac{v}{c_0} = \frac{(\rho v)'}{(\rho_0 + \rho')}$, $T' = \frac{T - T_0}{T_0} = \frac{\gamma p' - \rho'}{1 + \rho}$. For convenience a stagnation density of $\rho_0 = 1$ is used [15] [36].

2.3 Coordinate transformation

The following section is taken from the corresponding section of the author's project work [2]. In order to apply a finite difference method for a Cartesian grid on a general structured grid, and in that way be able to let the spacing in the discretization stencil be constant, the governing equations (13) are transformed. Let (x, y) represent the physical coordinates in the domain, and let (ξ, η) represent the transformed coordinates in a uniform Cartesian grid. Since the calculations happens in the transformed coordinates it can be referred to as the calculation domain. Now, let the physical coordinates depend on the transformed coordinates:

$$x = (\xi, \eta), y = (\xi, \eta).$$

According to the chain rule the differential operators then becomes:

$$\frac{\partial}{\partial x} = \xi_x \frac{\partial}{\partial \xi} + \eta_x \frac{\partial}{\partial \eta},$$
$$\frac{\partial}{\partial y} = \xi_y \frac{\partial}{\partial \xi} + \eta_y \frac{\partial}{\partial \eta},$$

where the subscripts indicate differentiation.

Establishing this coordinate transformation, the coordinate stretching can be summed up by:

$$\begin{pmatrix} \xi_x & \xi_y \\ \eta_x & \eta_y \end{pmatrix} = \begin{pmatrix} x_\xi & x_\eta \\ y_\xi & y_\eta \end{pmatrix}^{-1} = J \begin{pmatrix} y_\eta & -x_\eta \\ -y_\xi & x_\xi \end{pmatrix} \tag{16}$$

where J is the Jacobian determinant of the transformation equal to the ratio of the areas of the computational domain and the physical domain. Formally it is defined as [15]:

$$J = det(\frac{\partial(\xi, \eta)}{\partial(x, y)}) = \frac{1}{x_\xi y_\eta - y_\xi x_\eta}, \tag{17}$$

Applying the coordinate transformation to the compressible Navier-Stokes equations in (10) and rewriting equation (13) the following equations are derived:

$$\hat{\boldsymbol{U}}'_t + \hat{\boldsymbol{F}}'_\xi + \hat{\boldsymbol{G}}'_\eta = 0, \tag{18}$$

$$\hat{\boldsymbol{U}}' = J^{-1}\boldsymbol{U}', \tag{19}$$

where $\hat{\boldsymbol{F}}' = J^{-1}(\xi_x(\boldsymbol{F}^{c\prime} - \boldsymbol{F}^{v\prime}) + \xi_y(\boldsymbol{G}^{c\prime} - \boldsymbol{G}^{v\prime}))$ and $\hat{\boldsymbol{G}} = J^{-1}(\eta_x(\boldsymbol{F}^{c\prime} - \boldsymbol{F}^{v\prime}) + \eta_y(\boldsymbol{G}^{c\prime} - \boldsymbol{G}^{v\prime}))$.

It should be noted that in the simulations conducted, the coordinate transformation is such that grid lines are not curved. This means $x_\eta = 0$ and $y_\xi = 0$. The coordinates ξ and η can hence be referred to as the transformed x and y, respectively [36]. The relation in equation (16) can hence be reduced to the two relations [9]: $J^{-1}\xi_x = y_\eta$ and $J^{-1}\eta_y = x_\xi$.

Using these simplifications for the coordinate transformation, the viscous and the convective parts in equation (18) can be separated into their own residual terms, $\boldsymbol{R}'_v$ and $\boldsymbol{R}'_c$, such that equation (18) becomes

$$\hat{\boldsymbol{U}}'_t + \boldsymbol{R}'_v + \boldsymbol{R}'_c = 0, \tag{20}$$

where $\boldsymbol{R}'_v = -\frac{\partial}{\partial \xi} J^{-1}\xi_x \boldsymbol{F}^{v\prime} - \frac{\partial}{\partial \eta} J^{-1}\eta_y \boldsymbol{G}^{v\prime}$ and $\boldsymbol{R}'_c = \frac{\partial}{\partial \xi} J^{-1}\xi_x \boldsymbol{F}^{c\prime} + \frac{\partial}{\partial \eta} J^{-1}\eta_y \boldsymbol{G}^{c\prime}$.

A visualization of a typical grid for a circular cylinder is shown in figure 4.

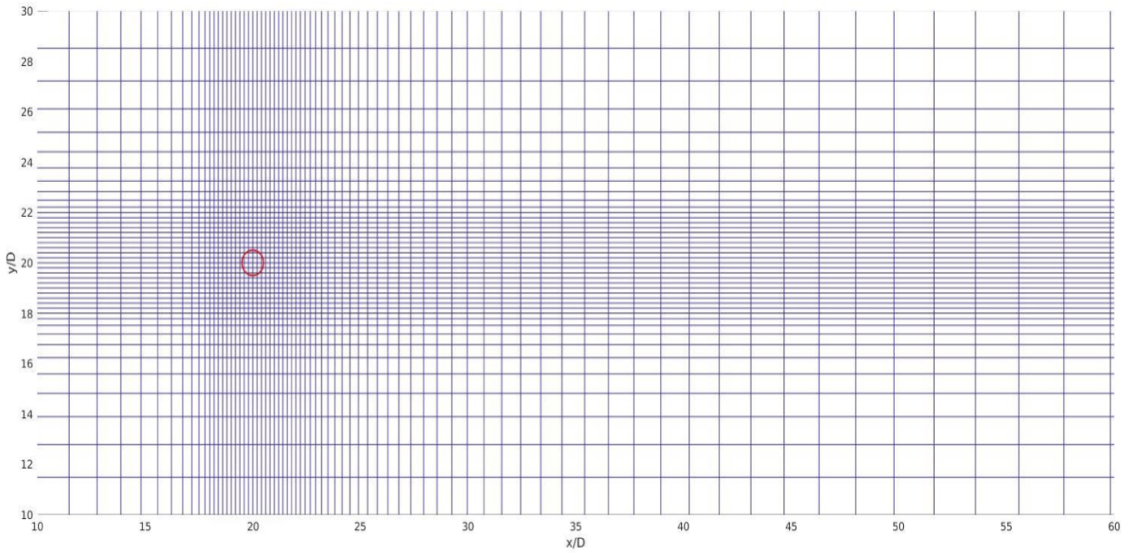

Figure 4: Cartesian grid near a circular cylinder for $(x, y) \in [18D, 22D] \times [18D, 22D]$, and stretched grid away from the cylinder. Every 5th line is plotted [36]

2.4 Mass-spring-damper system

The following section is taken from the corresponding section of the author's project work [2]. As its name indicates, a mass-spring-damper system is a system which can be visually represented by a mass m attached to a spring with stiffness k and a damper with a damping coefficient b, while being subject to external forces. A sketch of such a system depicting a cylinder with diameter D under influence of external forces F_D and F_L is found in figure 5).

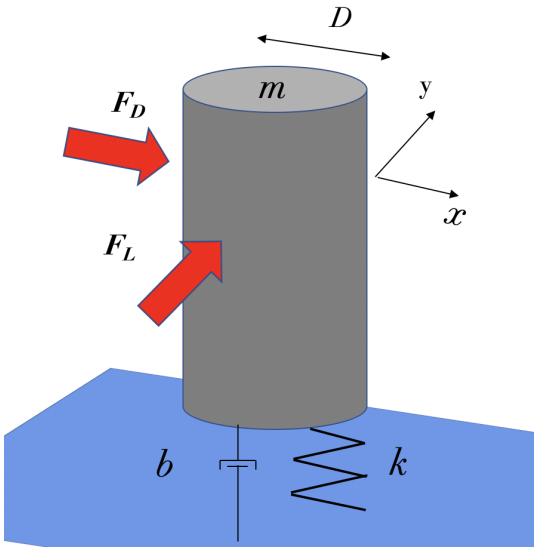

Figure 5: Visual representation of a 2D mass-spring-damper system with a cylinder with a diameter D under the influence of two forces F_D and F_L.

Many vibrating systems can be described using a mass-spring damper model. In this project, the model has been used to model a 2-dimensional elastically mounted cylinder under the influence of a flow-field exerting external forces to the cylinder. The cylinder is modelled as as centroid at position (x_0, y_0) with a circular surface with a diameter D around it marking the immersed boundary. Forces exerted on this surface are to be the external forces, and the movement of the centroid is calculated on the basis of these forces. The cylinder surface follows the movement of the centroid making the cylinder elastically mounted but non-deformable. Applied to this 2D problem, the 2D mass-spring-damper system is described by the 2nd order system:

$$m_s\ddot{x} + b\dot{x} + k(x - x_0) = F_D(t), \tag{21}$$

$$m_s\ddot{y} + b\dot{y} + k(y - y_0) = F_L(t), \tag{22}$$

here $x - x_0$ and $y - y_0$ are the displacement from equilibrium position $x = x_0$ and $y = y_0$, respectively, $F_L(t)$ and $F_D(t)$ are the drag- and lift forces from the fluid on the cylinder respectively, m_s is the cylinder mass and dots indicate derivatives with respect to time.

The drag and the lift force can be related to the governing equations of the fluid by integrating the traction over a control volumes surface $\partial\Omega$ representing the fluid-structure boundary. This yields the following equation for F_L and F_D:

$$\boldsymbol{F}_{external}\begin{pmatrix} F_D \\ F_L \end{pmatrix} = \oint_{\partial\Omega} -p\delta_{ij}n_j + \tau_{ij}n_j dA, \tag{23}$$

where p and τ_{ij} is the pressure and viscous stress tensor at the fluid-solid interface, and n_j is the unit normal vector.

To understand the dynamics of the mass-spring damper system, an important parameter needs to be defined, namely the natural frequency: $f_N = \frac{1}{2\pi}\sqrt{\frac{k}{m}}$. The natural frequency is the frequency in which the mass would oscillate around its equilibrium if no damping or external forces are applied. The energy in the system would then be conserved being exchanged between potential energy $E_{pot} = \frac{1}{2}k(x^2 + y^2)$ in the "spring" and kinetic energy in the moving cylinder $E_{kin} = \frac{1}{2}m(\dot{x}^2 + \dot{y}^2)$. Adding the two forms of energy together gives the total energy the structure system:

$$E_{tot} = E_{kin} + E_{pot} = \frac{1}{2}(k(x^2 + y^2) + m(u^2 + v^2)), \tag{24}$$

where u and v are the velocity components of the cylinder in x- and y-directions, i.e. $\dot{x}$ and $\dot{y}$, respectively.

Multiplying equation (21) and (22) by u and v respectively, and adding them together gives the equation for the rate of change of energy in the system:

$$\frac{\partial E_{tot}}{\partial t} = F_D u + F_L v - bu^2 - bv^2. \tag{25}$$

Again, doing a control volume analysis over the fluid-structure boundary by multiplying the expression inside the integral sign in equation (23) by the interface velocity $u_j = (u, v)$, an expression for the rate of energy change of the structure can be related to the power P transferred from the fluid:

$$P = \int_{\partial\Omega} -pu_j n_j + \tau_{ij}u_j n_j dA = F_D u + F_L v. \tag{26}$$

As can be seen in equation (25), the external forces can both function as sources or sinks for the structure system depending on the sign of the force and the movement of the cylinder. Since drag and lift forces are the only terms which can be deduced both for the fluid and the structure (see equations (26)), they function as the energy-transfer terms between the fluid- and the structure-systems. The damping term in (25) can only be positive consequently always contributes to energy losses, it is a dissipation term.

Non-dimensionalizing (21) and (22) and setting the equilibrium point to $(0, 0)$ gives the following

$$\ddot{q} + 2\zeta \left(\frac{2\pi}{U^*}\right) \dot{q} + \left(\frac{2\pi}{U^*}\right)^2 q = \frac{2}{\pi m^*} c_{D,L}(t), \tag{27}$$

where q indicates the non-dimensional displacement. The other parameters are the non dimensional damping $\zeta = \frac{b}{2\sqrt{km_s}}$, $m^* = \frac{\rho_s}{\rho_f}$ is the dimensionless mass, $U^* = \frac{U}{f_N D}$ and $C_{D,L}$ is the lift- and drag-coefficient. x and y are non-dimensionalized by the cylinder diameter D and t by D/U, giving q and its time-derivatives. Subscript s and f indicate solid and fluid properties.

To make it more suitable for discretization, equation (27) can be rewritten to a set of first order ODEs. Let the non-dimensional displacement vector $\vec{q}$ be defined as:

$$\vec{q} = (x/D, y/D)^T \tag{28}$$

.

Following Ringstad [36], the system is then rewritten from the form $\ddot{\vec{q}} = f(t, \vec{q}, \dot{\vec{q}})$ into $\dot{\mathbf{Q}} = \mathbf{G}(t, \mathbf{Q})$, where $\mathbf{Q} = \begin{pmatrix} \vec{Q}_1 \\ \vec{Q}_2 \end{pmatrix} = \begin{pmatrix} \dot{\vec{q}} \\ \vec{q} \end{pmatrix}$ and t is the physical time. $\vec{Q}_1 = \begin{pmatrix} \dot{x} \\ \dot{y} \end{pmatrix}$ and $\vec{Q}_2 = \begin{pmatrix} x \\ y \end{pmatrix}$.

The time dependence of f and $\mathbf{G}$ is due to the drag and lift components, $c_D(t)$ and $c_L(t)$, respectively. This gives the system of equations:

$$\frac{d}{dt} \begin{pmatrix} \vec{Q}_1 \\ \vec{Q}_2 \end{pmatrix} = \begin{pmatrix} G_1(t, \vec{Q}_1, \vec{Q}_2) \\ \vec{Q}_1 \end{pmatrix} = \mathbf{G}(t, \mathbf{Q}), \tag{29}$$

where the first component of (29) corresponds to equation (27) solved for the acceleration, i.e., $G_1 = -2\zeta \left(\frac{2\pi}{U^*}\right) \vec{Q}_1 - \left(\frac{2\pi}{U^*}\right)^2 \vec{Q}_2 + \frac{2}{\pi m^*} \begin{pmatrix} c_D(t) \\ c_L(t) \end{pmatrix}$ [36].

2.5 Flexible plate model

In the test case *Flexible plate behind a cylinder*, the plate is made of an elastic and compressible material [45] which is deformed by the forces exerted by the surrounding fluid. Its deformation in x- and y-direction can be described by the standard 2D momentum equations for solids containing a Cauchy stress tensor modelled according to the constitutive law of a St. Venant-Kirchhoff material. The density at undeformed configuration is ρ_s and the elasticity is characterised by the Poisson ratio ν_s and the Young modulus E. For further detail the reader is referred to the article by Turek and Hron [45].

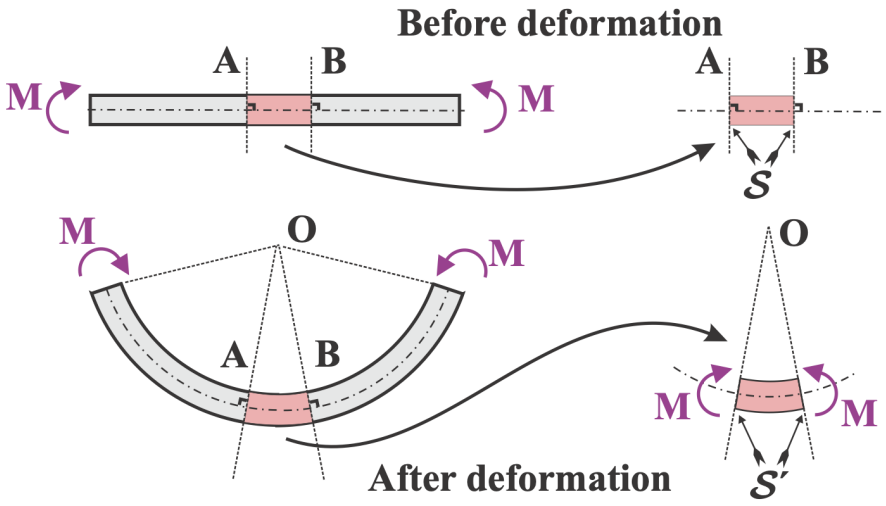

Figure 6: Infinitely long Euler-Bernoulli beam under end bending moments [3]

In the simulations conducted in this thesis, the plate model is simplified and described by the Euler-Bernoulli equation for a cantilever beam of length l and a finite thickness h [36]. This means that only bending momentum and displacement in the lateral direction (y-direction) is taken into account, and that rotary inertia and shear deformation are neglected [13]. Any cross section of the beam will thus remain plane and normal to the deformed axis after deformation as shown in figure 6 where the 90° angle between the mid line and the cross section is drawn before and after deformation [3]. These assumptions are valid for long slender beams which only undergo small deformations [3], but loose their accuracy when the aspect ratio (l/h) is around 10 [8]. Higher vibration modes may become a difficult to approximate even for beams with an aspect ratio of around 30 [8]. However, Garcia [10] showed that the Euler-Bernoulli beam assumption compared well with the results from the benchmark solution for the structural test case provided by Turek and Hron [45].

The displacement of the plate is influenced by the internal shear forces and external forces from the fluid. The lateral displacement from the neutral reference axis can be described by a function $\phi(t, x) = y(t, x) - y_0$, where y_0 is the y-coordinate of the neutral reference axis. Since the beam is only aloud to move in the lateral direction, the external force exerted by the fluid is restricted to the force in y-direction. The pressure load on the plate is assumed to be much larger than the normal viscous normal traction and thus only pressure force is taken into account. Hence the external load is simply the pressure difference, δp, between the two sides of the plate. The internal shear forces are applied to the beam through the variation of the bending momentum, $M(x, t)$, of the beam. The bending momentum on the plate is proportional to the curvature through the

relation $M(x,t) = -EI\frac{\partial^2\phi}{\partial x^2}$, where I is the second moment of inertia and E is Young's modulus [3] [36]. By the assumption made of a constant cross section, the second moment of inertia is constant and relocatable to the Poisson ratio and the beam thickness h [3]. The product $B = EI$ also known as the flexural rigidity is thus a constant equal to $B = \frac{Eh^3}{12(1-\nu_s^3)}$, and is as can be seen related to the material and kinematic properties spescified in the reference paper by Turek and Hron [45]. The momentum balance gives the following equation for the beam displacement:

$$\rho_s h\frac{\partial^2\phi}{\partial t^2} + d\frac{\partial\phi}{\partial t} + B\frac{\partial^4\phi}{\partial x^4} = -\delta p, \tag{30}$$

where ρ_s is the structure density. Damping can also be applied to the equations through the damping term $d\frac{\partial\phi}{\partial t}$, where d is the structural damping. This was not applied in these simulations [36].

Following Ringstad [36], the length and time were non-dimensionalized as for the fluid solver with respect to the reference length D and the reference time scale $\frac{D}{c_0}$. The mass $m = \rho_s h$, damping d and fexural rigidity B were nondimensionalized using the fluid stagnation density ρ_0, stagnation speed of sound c_0, cylinder diameter D, and reference pressure $\rho_0 c_0^2$. These non-dimensional quantities are presented in table 1.

Table 1: Dimensionless variables of equation 30. The apostrophe indicating the dimensionless quantity [36]

B'	$\frac{B}{\rho_0 c_0^2 D^3}$
d'	$\frac{d}{\rho_0 c_0}$
m'	$\frac{\rho_s h}{\rho_0 D}$

The beam is attached to the cylinder at the point $x = 0$ by clamping, and is allowed to move freely in y-direction at the end $x = l$. These boundary conditions read in continuous form [16] and [36]:

$$\phi(t,0) = 0,, \tag{31}$$

$$\frac{\partial\phi(t,0)}{\partial x} = 0, \tag{32}$$

The boundary conditions at the free end can, under the assumption of zero bending moment and zero shear force, be written:

$$\frac{\partial^2\phi(t,l)}{\partial x^2} = 0, \tag{33}$$

$$\frac{\partial^3\phi(t,l)}{\partial x^3} = 0, \tag{34}$$

Just as for the elastic cylinder, the energy transfer from the fluid to the tail can be found by equation (26). The rate of change of energy in the Euler-Bernoulli equation has been evaluated by [16] and reads:

$$\frac{d}{dt}\left(\frac{1}{2}\rho_s h\int_0^L \dot{\phi}^2 dx + \frac{1}{2}B\int_0^L (\phi_{xx})^2 dx\right) = \int_0^L (-\delta p)\dot{\phi}dx - d\int_0^L \dot{\phi}^2 dx \tag{35}$$

The pressure load transfers power to the system through the term $P_s = \int_0^L (-\delta p)\dot{\phi}dx$. This corresponds analytically to the fluid power term $\int_0^L p n_j u_j dx$ of eqn. (26).

3 Discretization

In this chapter, the techniques to discretize the governing equations presented in chapter 2 are explained. First, the numerical methods used in the space and time discretization is outlined in 3.1, then in section 3.2 the ghost point immersed boundary method is explained, and at last the specific implementation of the two test cases: elastically mounted cylinder and flexible plate behind a cylinder are explained in sections 3.3 and 3.4, respectively.

3.1 Numerical methods

3.1.1 Finite difference summation by parts method

To discretize the spatial derivatives in the fluid solver a finite difference method (FDM) is used. Finite difference methods got their advantages and disadvantages compared to other techniques, such as the finite folume method (FVM) and the finite element method (FEM), in the discretization of the PDEs describing the fluid flow. They are in general easier to implement and higher order discretization schemes are easier to develop than for FEM and FVM. However, FDM schemes is not always conservative and rely on a structured grid, preferably a Cartesian [44] [30]. For complex geometries in CFD, unstructured grids which are incompatible with FDM but works well for FVM and FEM are preferred. The ghost point immersed boundary method which is outlined in 3.2 is based on using finite difference methods and avoids the problem of complex geometries.

The energy method is a technique to show that a partial differential equation (PDE) will be well posed and a finite difference method (FDM) is stable [12] [15]. The summation by parts (SBP) property of a numerical scheme assures that an energy estimate can be made, and that the energy is bounded by the initial condition. If a numerical scheme inherits the SBP property it will thus be stable. Central difference schemes even of higher order are easy to obtain for the finite difference method. However, at the boundaries, not enough points are available to apply central difference stencils and adaptions in the way of utilizing one-sided difference stencils needs to be made. It is non-trivial to construct operators for higher order schemes but several exist, cf. Gustafsson [12] or Svärd and Nordström[43]. In the PhD thesis of Khalili [15] and master thesis of Ringstad [36], a locally sixth order method in the interior and globally fourth order accurate method was used with the ghost point immersed boundary method. For problems involving only convex geometries, the method achieved good results. But for non-convex geometries, the wide stencil needed to compute the viscous fluxes where the operators need to be applied consecutively, led to problems. The problem will be further elaborated in section 3.2.1 In the spatial discretization of the governing fluid equations in this thesis, a simple second order SBP operator is thus used. It utilizes second order central difference to approximate the derivative in the interior, and a one sided difference of first order at the boundary.

To illustrate the 2nd order SBP method, consider a one-dimensional uniform grid stretching from x_0 to x_N, consisting of $N+1$ grid-points. Any point x_j on the grid is equal to $x_j = jh$, where $h = \frac{x_N - x_0}{N-1}$ and $j = 0, 1, .., N-1, N$. Now, consider a field of a variable u that can be interpreted as for the velocity in x-direction for instance. The grid function maps u onto the points x_j such that a vector $u_j = u(x_j)$ is defined [12]. The second order SBP operator approximating the derivative

of the vector u_j is then defined by

$$D_2{}^{(1)} = \frac{1}{h}\begin{bmatrix} -1 & 1 & & & & & \\ -\frac{1}{2} & 0 & \frac{1}{2} & & & & \\ & -\frac{1}{2} & 0 & \frac{1}{2} & & & \\ & & \ddots & \ddots & \ddots & & \\ & & & & -\frac{1}{2} & 0 & \frac{1}{2} \\ & & & & & -1 & 1 \end{bmatrix}, \tag{36}$$

where the index 1 indicates that it is an approximation of the first derivative and the subscript (2) indicates that it is of second order.

A problem arises when boundary conditions (BCs) are to be included for an SBP scheme. For simplest and most common way to impose BCs, the injection method, operators get alternated at the boundary and looses their SBP property. Consider for instance the no penetration boundary condition $u(x = 0) = 0$. The upper row of the matrix in (36) is no longer used and the operator $D_2^{(1)}$ is altered and looses its SBP property. This means that an energy estimate can not be made to assure bounded energy. It is thus common to instead use a simultanious approximation term (SAT) to impose the boundary condition weakly [12]. Despite this, the injected boundary conditions are simple to program and SBP operators are useful because of their adaption to the boundary. Hence an altered 2nd order SBP operator is used in the thesis, but will still be referred to as 2nd order SBP.

3.1.2 Explicit filtering

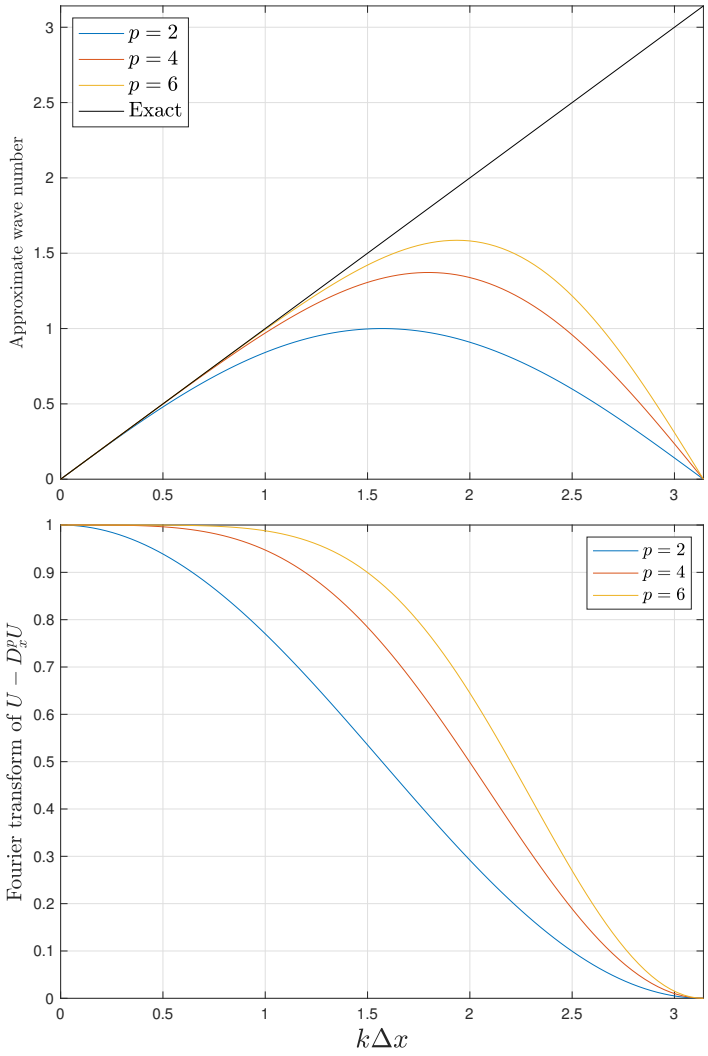

Figure 7: Top: Approximate wave numbers of standard central *pth* order central difference operators of the first derivative, p = 2, 4, 6. Bottom: Fourier transform of low pass filter of orders p = 2, 4, 6 [32] [48]

FDM like the second order central FDM do not transport waves with the correct phase velocity, especially waves with higher wavenumbers. This phenomena, also known as numerical dispersion, is recognised by the wiggles in the solution of the numerical simulation due to the different wavelengths traveling at different speeds. As can be seen in the upper part of figure 7, waves of wave number $k = \pi/\Delta x$ will not even be transported by the central difference scheme, and thus lead to oscillations of wavelength $\Delta x/\pi$ that do not move. Due to this, artificial dissipation in the form of a second order explicit low pass filter in x- and y-direction is added to the residual after a full RK4 stage. This removes the waves with the wavenumbers $\pi/\Delta x$ and$\pi/\Delta y$ in the x- and

y-directions, respectively. The filtering modifies the solution vector in the following way after n time steps:

$$\tilde{\boldsymbol{U}}'_{j,k}{}^{n} = \hat{\boldsymbol{U}}'_{j,k}{}^{n} - [D_{\xi}^{(2)}\hat{\boldsymbol{U}}' + D_{\eta}^{(2)}\hat{\boldsymbol{U}}]^{n}_{j,k}, \tag{37}$$

where n indicates the time step, j and k indicate the spatial grid point, and $D_{\xi}^{(2)}$ and $D_{\eta}^{(2)}$ represent the filter in x-direction and y-direction, respectively. The filtering operator follow the form of the central difference approximation that in x-direction is equal to:

$$D_{\xi}^{p}\hat{\boldsymbol{U}}' = \frac{(-1)^{p/2}}{2^{p}}\delta_{\xi}^{p}\hat{\boldsymbol{U}}', \tag{38}$$

where $\delta_{\xi}U_{i,k} = U_{i+1/2,k} - U_{i-1/2,k}$ is the central difference operator. For the second order filter $p = 2$, the approximation becomes $\delta_{\xi}^{2}\hat{\boldsymbol{U}}'_{j,k}{}^{n} = \frac{\hat{\boldsymbol{U}}'_{j+1,k}{}^{n} - 2\hat{\boldsymbol{U}}'_{j,k}{}^{n} + \hat{\boldsymbol{U}}'_{j-1,k}{}^{n}}{\Delta\xi^{2}}$. D_{η} is defined analogously in y-direction [32] [48]. Note that in this thesis, the filter is only applied to the interior grid-points where the second order central difference operator is used.

A Fourier analysis is done for the *pth* order filter and *pth* order central difference approximation is done in figure 7 [32] [48]. $k\Delta x$ represent the non-dimensional wave number. As can be seen in the upper plot of figure of 7, the second order central difference stencil is able to well predict non dimensional wave numbers up to approximately 0.5. Ideally, the filter should remove all modes higher than this. But as can be observed in the lower figure of 7, the second order filter start to dissipate wave numbers of approximately $k\Delta x = 0.25$. This means that some resolved wave modes are damped as well, meaning that a bit too dissipative filter is used. Due to this, the filter is not applied at each time step.

3.1.3 Explicit Runge-Kutta method

The time integration of the fluid solver in the test cases, and the system of ODEs in equation (29) representing the cylinder movement for an elastically mounted cylinder is done by the classic fourth order explicit Runge-Kutta method (RK4). The rest of the section is taken from the author project work [2].

The method belongs to the class of Runge-Kutta methods where the derivative is approximated by adding together a weighted sum of the derivatives at intermediate stages. To illustrate the method, consider the system of first order differential equations:

$$\frac{d\mathbf{Q}}{dt} = \dot{\boldsymbol{Q}} = \boldsymbol{G}. \tag{39}$$

Let the time be equal to t^n. We wish to calculate $\boldsymbol{Q}$ at time level t^{n+1}. A single full time step is equal to $\Delta t = t^{n+1} - t^n$. Now, let $\mathbf{k}_m, \{m = 1, 2, 3, 4\}$ be estimates of $\dot{\boldsymbol{Q}}(t^n + \Delta t_m)$, where Δt_m corresponds to the following intermediate time steps $(\Delta t_1, ..., \Delta t_4)^T = \left(0, \frac{\Delta t}{2}, \frac{\Delta t}{2}, \Delta t\right)^T$.

The stages are then evaluated by:

$$\mathbf{k}_m = \mathbf{G}(t^n + \Delta t_m, \mathbf{Q}^n + \mathbf{k}_{m-1}\Delta t_m), \{m = 1, 2, 3, 4\}. \tag{40}$$

Here $\mathbf{k}_1$ corresponds to the acceleration and velocity at time t^n, i,e., $\dot{\mathbf{Q}}^n$. From the Runge-Kutta stages, the solution at the new time level is calculated as [36]:

$$\mathbf{Q}^{n+1} = \mathbf{Q}^n + \Delta t\left(\frac{1}{6}\mathbf{k}_1 + \frac{1}{3}\mathbf{k}_2 + \frac{1}{3}\mathbf{k}_3 + \frac{1}{6}\mathbf{k}_4\right). \tag{41}$$

3.1.4 Numerical solution of plate model

The discretization of the Euler-Bernoulli equation (30) is done by discretizing the reference axis into *N joint points* (*jp*). Each joint point is fixed in x-direction and is able to move in y-direction, meaning that its coordinate is equal to $\boldsymbol{s}_i = (x_i, y_0 + \phi_i(x_i, t)$, where $i = 1, ..., N$. The fourth derivative in equation (30) is approximated using the standard second order central difference approximation for double derivatives twice, giving the approximation $\frac{\partial^4 \phi(x_i)}{\partial x^4} = \frac{\phi_{i+2} - 4\phi_{i+1} + 6\phi_i - 4\phi_{i-1} + \phi_{i-2}}{\Delta x^4}$. The time integration of equation (30) is then numerically solved with the second order accurate implicit Newmark method [33] [16]. The Newmark method solves for the velocity and displacement by using the velocity and acceleration evaluated at the old and new time steps weighted by the factors γ and β. The integration from time level n to $n+1$ for a velocity $\dot{\phi}$ and displacement ϕ_i is calculated by [33]:

$$\dot{\phi}_i^{n+1} = \dot{\phi}_i^n + \left((1-\gamma)\ddot{\phi}_i^n + \gamma\ddot{\phi}_i^{n+1}\right)\Delta t, \tag{42}$$

$$\phi_i^{n+1} = \phi_i^n + \dot{\phi}_i^n \Delta t + \left[(\frac{1}{2} - \beta)\ddot{\phi}_i^n + \beta\ddot{\phi}_i^{n+1}\right]\Delta t^2, \tag{43}$$

where $\ddot{\phi}_i$ is the acceleration, and β and γ are coefficients.

The coefficient values used in the simulation are $\gamma = \frac{1}{2}$ and $\beta = \frac{1}{4}$, which yield unconditional stability and the best accuracy of the Newmark methods [16] [36].

The attached plate is clamped corresponding to the boundary conditions (31) and (32). These boundary conditions read in discrete form:

$$\phi_1 = 0, \tag{44}$$

$$\phi_2 = \phi_1 \tag{45}$$

The boundary condition at the free end (33) and (34), are written in discrete form:

$$\phi_{N-1} = 2\phi_{N-2} - \phi_{N-3}, \tag{46}$$

$$\phi_N = 3\phi_{N-2} - 2\phi_{N-3}. \tag{47}$$

.

3.2 Ghost point immersed boundary method

In this thesis, the ghost-point immersed boundary method (GP IBM) developed by Khalili et al. [9] is used. In the computational domain, any grid point is either a fluid-, solid- or ghost-point. Fluid points are points inside the fluid domain and are separated by the other points by the immersed boundary. Inside the solid, there are solid- and ghost-points. Ghost-points are points close to the interface which are given fluid properties by interpolating boundary conditions at the interface. Because the computational stencil of the fluid points at the fluid-solid interface will extend into the solid, they need information from these ghost-points inside the solid The way this is done is by including the ghost-points in their finite-difference stencil and use the fluid properties imposed by approximating the boundary condition. Depending on the width of the computational stencil, the number of layers of ghost points is decided. In this project, a 3 point wide stencil have been used and thus only one layer of ghost points is needed.

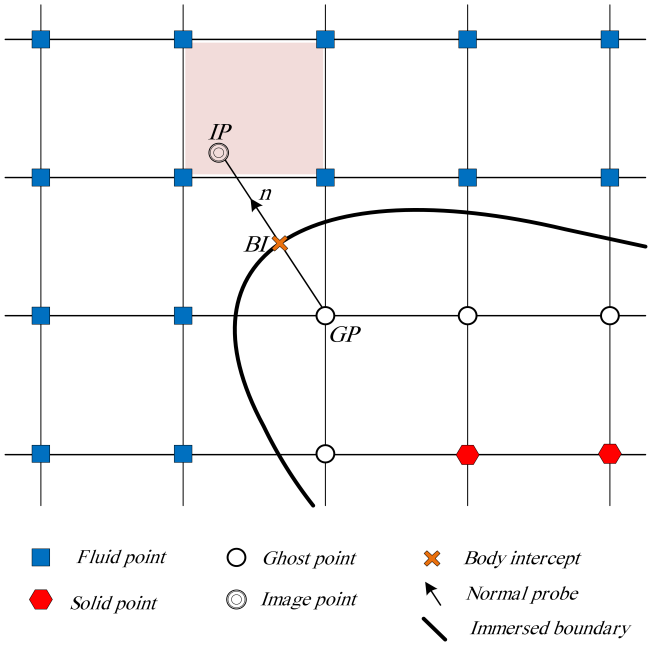

Figure 8: Illustration of the ghost-, image- and boundary intersect-points [9]

Figure 8 illustrates the interpolation process imposing the boundary conditions and giving the ghost-points (GP) their properties. A normal line between the ghost point and the immersed boundary at the body intercept (BI) is extended into the fluid region. At the end of this line inside the fluid domain, an image point (IP) is defined. The distance between the intersection point and the ghost-point is equal to the distance between the intersection and the image point, leaving the intersection point in the middle of the line segment. Using the fluid properties of the the four closest fluid points in a bi-linear interpolation, the fluid property of the image point can be set. In some special cases where the ghost point is very close to the boundary, properties at the BI points can be used in the interpolation scheme. An illustration on this can be found in figure 9 and a more detailed description of this special treatment can be found in the PhD thesis of Khalili [15]. It should be noted that the bi-linear interpolation scheme is of second order accuracy ($O(\Delta x^2)$). In contrast to the higher order GPIBM by Khalili et al. [9], the interpolation scheme should hence no longer an as significant source of error, since it is of the same as the central difference method used in the present method, and fewer layers of ghost points are used.

In the case of a Dirichlet boundary condition of a property ϕ, the value at the ghost point is be set by assuming that the average of the property at the image point and the ghost point is equal to the boundary condition, i.e. $\frac{\phi_{IP}+\phi_{GP}}{2} = \phi_{BI}$. This gives the following formula for a Dirichlet boundary condition (BC):

$$\phi_{GP} = 2\phi_{BI} - \phi_{IP}. \tag{48}$$

In the case of a Neuman boundary condition of a property ϕ, i.e. $\frac{\partial \phi}{\partial n} = \beta$, the finite difference approximation at BI should be equal to β. This means $\frac{\phi_{IP}-\phi_{GP}}{\Delta l} = \beta$, where Δl is the distance between the image point and the ghost point. Rewriting the expression, the formula for ϕ_{GP} becomes:

$$\phi_{GP} = \phi_{IP} - \Delta l \beta. \tag{49}$$

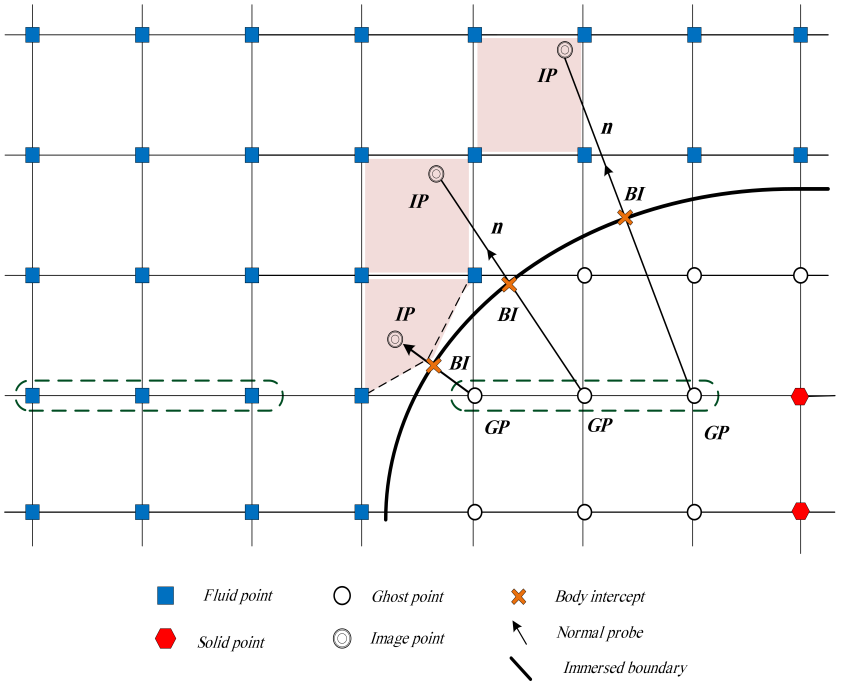

Figure 9: Illustration of points used in the bi-linear interpolation procedure when image points are located at difference distances from the immersed boundary, and points included in the stencil of a sixth order central difference method taken from the PhD thesis of Khalili [15]. In this illustration, three layers of ghost points are used, however in the present thesis only one is used.

Together, the mass conservation equation, the compressible momentum equations and the energy equation (see equations (1)-(3)) contain four unknowns after assuming perfect gas, Newtonian fluid etc. as explained in section 2. This means that four boundary conditions are needed at the immersed boundary which is the cylinder wall or the flexible plate wall in the simulations conducted in this thesis. The main variables solved for contained in the vector $\boldsymbol{U}$ in equation (9) can be described by the velocity components u and v, the density ρ, the temperature T or the pressure p. The cylinder wall is no-slip, adiabatic and has zero normal pressure-gradient (boundary

layer approximation [9] [15]. This gives the following equations for the boundary conditions:

$$\vec{u} = \vec{U}_{wall}, \tag{50}$$

$$\frac{\partial T}{\partial n} = 0, \tag{51}$$

$$\frac{\partial p}{\partial n} = 0, \tag{52}$$

where $\vec{U}_{wall}$ is the prescribed velocity of the wall and n denotes the wall normal direction. Due to the perfect gas law from equation (4) the BC (51) and (52), a boundary condition for ρ can be deduced [9]:

$$\frac{d\rho}{dn} = \frac{\partial(\frac{RT}{p})}{\partial n} = 0. \tag{53}$$

3.2.1 Number of layers of ghost-points

The viscous fluxes in equation (13) contains terms such as ${T_x}'$ and ${u_x}'$ where derivatives are present. Consequently, to be able to approximate the viscous fluxes at the fluid-points close to the boundary, terms like ${T_x}'$ and ${u_x}'$ needs to be approximated at the ghost points. To be able to predict both the viscous and the convective flux derivatives at the fluid points closest to the immersed boundary, it is necessary to adjust the number of ghost points layers accordingly. In figure 9 the determination of the number of layers of ghost points for the globally 4th order SBP method used by E. Khalili in his PhD during the initial development of the the GP IBM method [15], and by K. Ringstad in his master-thesis [36]. The method uses a 6th order central difference stencil in the interior, and a 3rd order one sided difference stencil at the boundary is illustrated in figure 9. In the second row from the bottom, the fluid point closest to the boundary have three ghost points on its right side (marked with a dashed line) and three fluid points on its left side (marked with a dashed line). This means that the seven required either ghost or fluid-points are present to be able to approximate both flux derivatives using a sixth order stencil [9].

For the globally fourth order SBP method, at least nine ghost or fluid points are required to approximate the viscous terms. If the 6th order central FDM should be used in the middle, as many as 13 points are required. For too sharp concave boundary configurations and very thin structures, the globally fourth order SBP operator hence lacks the required amount of ghost and fluid points to calculate the viscous flux derivatives and thus the viscous residuals. To illustrate, while conducting simulations of a flexible plate behind a cylinder case in his master thesis, K.Ringstad encountered two such configurations making the simulation impossible to preform using the method. The first one was for concave corners as illustrated in figure 10, and the other for perturbed surfaces as illustrated in figure 11.

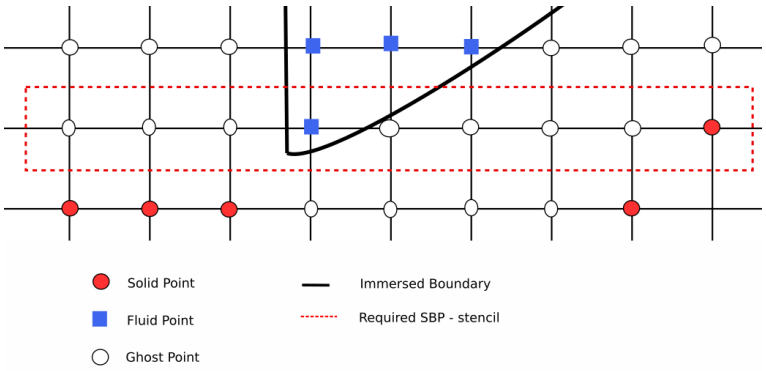

Figure 10: Illustration of the required SBP-boundary operator stencil width being wider than the number of available points [36]

One could think that a simple solution to the problem of lacking enough points to calculate the viscous derivatives would be to add more layers of ghost points. However, there are several issues arising with this approach. The first one is that it does not solve the problem for perturbed surfaces. Another one is when the structure is so thin that extending the layer of ghost point will turn all solid points through a cross section of the structure into ghost points. Adding ghost point layers also means that the innermost layer will lay further away from the boundary, which makes the linear interpolation error during the process of imposing fluid values at the ghost points larger than for the other layers. And as already mentioned in section 3.2, both this linear interpolation and the bi-linear interpolation procedure conducted to find image point and ghost point values are significant sources of discretization errors when used with the higher order SBP method. It is this that makes the use of the 2nd order SBP method an interesting solution to the problem. It will be able to deal with any geometrical configuration using only one layer of ghost points, and the interpolation methods will not serve as bottlenecks for the spatial grid convergence.

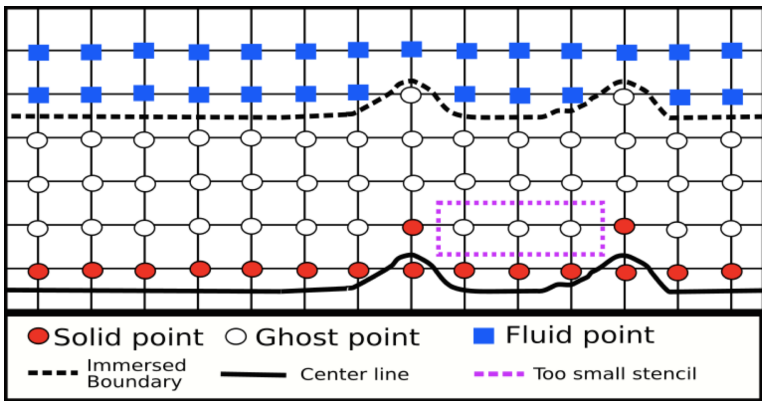

Figure 11: llustration of a perturbed surface creating a situation with too few neighboring ghost points to determine the derivatives of u, v, T in the viscous fluxes at the third layer of ghost points [36]

3.3 Implementation of an elastically mounted cylinder

The RK4 method is solved in parallel for the structure and fluid for the test-case elastically mounted cylinder. This means that for each stage in the RK4 method, the structure is moved according to the fluid flow, and new solid- and ghost points are found to impose the effect the structure has on the fluid. To find the force from the fluid on the structure and thereby its movement, the integral in equation (23) is approximated using the trapezoidal rule in polar coordinates [19]. A schematic representation of the algorithm is provided in appendix A.

3.4 Implementation of a flexible plate with immersed boundary method

The implementation of the ghost point immersed boundary method for the flexible plate behind a cylinder described in the paper by Turek Hron [45] is not straightforward. As explained in section 2.5 the plate is modelled as an Euler-Bernoulli beam. This model assumes an infinitely thin plate. In section 3.1.4 the numerical approach to the displacement of this plate using a finite difference method dividing the infinitely thin plate into joint points with a fixed x-coordinate was elaborated. However, one question remains. How is the finite thickness added and thereby the criteria to find out if a point on the grid is inside or outside the structure, and how is the velocity of the boundary found and thereby the velocity of the ghost points.

The tail consists of $N = 220$ joint points making up the mid line of the plate stretching from the edge of the cylinder at the left end to the trailing edge of the plate. This number of joint points corresponds to a joint point spacing in x-direction equal to $\Delta s_x = 0.0159$. The grid spacing in x direction used in this thesis is equal to $\Delta x = 0.01625$, meaning that the ratio $\frac{\Delta s_x}{\Delta x} = 1.022$. This joint point to grid point spacing in x direction was found by Ringstad [36] to be the most stable. The joint points were connected by natural cubic splines, creating a tail that is smooth not only in itself, but also have a smooth first derivative and a continuous second derivative [20]. Any position on the tail can then be found by a smooth function, $P(x)$, consisting of $N-1$ cubic polynomials, $P_i(x)$, where $i = 1, 2, ..., N-2, N-1$ on intervals between each joint point. This gives the following expression for the y-coordinate of a point on the tail that lies between joint point $\boldsymbol{s}_i = (x_i, y_0 + \phi_i)$ and $\boldsymbol{s}_{i+1} = (x_{i+1}, y_0 + \phi_{i+1})$:

$$P_i(x) = a_i + b_i x + c_i x^2 + d_i x^3, \qquad x \in [x_i, x_{i+1}], \tag{54}$$

where a_i, b_i, c_i and d_i are constants. The end conditions of the natural cubic splines corresponds to setting the constants so that $P_1''(x_1) = P_{N-1}''(x_N) = 0$. This is in accordance with the boundary condition at the free end of the cantilever beam, but at first sight not at the clamped end. However, in the simulations conducted, a 20 joint points were held in place at the clamped end, forcing the second derivative to also become zero close to the cylinder. Note that it is not necessary to clamp as many as 20 points, but to make results more comparable with those by Ringstad [36] using the higher order GPIBM, who also clamped 20 joint points, the simulations presented in this thesis have also clamped 20 points. This clamping using 20 joint points makes the elastic part of the plate onlly 3.9 shorter.

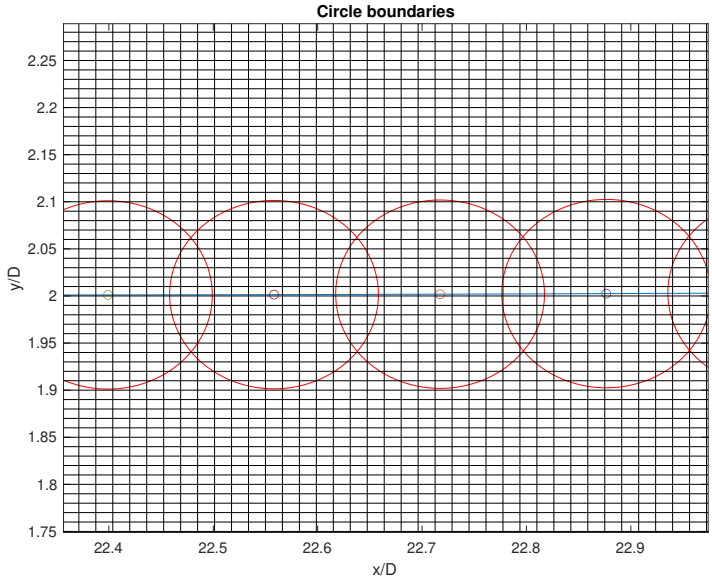

Figure 12: The figure shows how circles (red circles) are drawn around each joint point (small dots) to create a criteria for which nodes on the background grids are inside the tail. In this picture, the tail consists of 220 joint points connected by cubic splines and the grid in the inner block is (401×201) nodes large. Only each tenth joint point and its corresponding circle of radius $h/2$ is drawn.

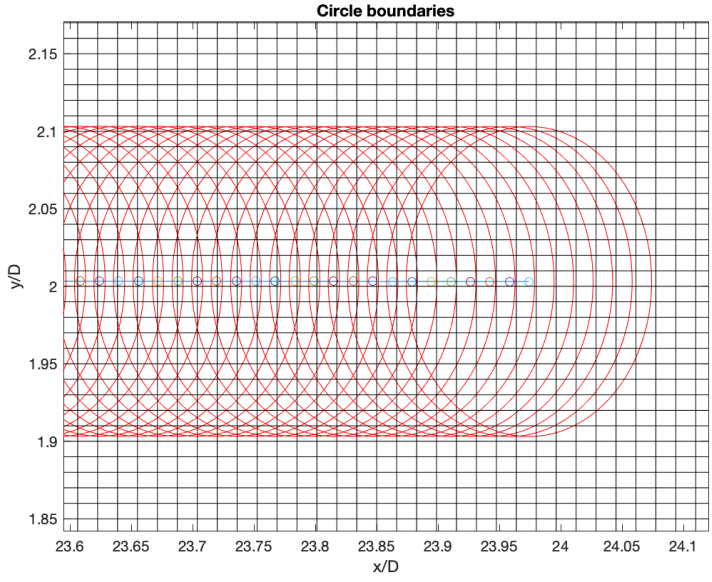

Figure 13: The figure shows the end of the tail when circles of radius $h/2$ around each joint point are used to decide which nodes on the grid are inside the tail. In this picture, the tail consists of 220 joint points connected by cubic splines. The grid used in the inner block is (401×201) nodes large.

All grid points points within a distance r from the center C of the cylinder and a distance less than $h/2$ from the tail mid line should be considered as solid or ghost points. The method for identifying each of these goes as follows. First points within the cylinder with center point C and radius r are first flagged as solid points. Then, all grid points within a distance $h/2$ from any joint point is identified as solid points. At first sight the method used to identify solid points within the tail might seem incomplete, but actually it is a simple consistent way to identify solid points if enough joint points are used. In figure 12 circles around every tenth joint points are drawn, and as can be seen, many solid points lack. But when circles increase to 220, all points that are a distance of $h/2$ are considered solid points, and the criteria works well. Using the circle criteria at the joint point at the trailing edge also implies that the tail is rounded. However, the flow physics around sharp corners is hard to capture without a very fine grid, and rounding is not believed to change the dynamics of the plate too much since the length of the plate is much larger than the thickness. The same procedure of rounding was also done for the same test case by Ringstad in [36] and for an Euler-Bernoulli using an immersed boundary method in by Li et al. [23].

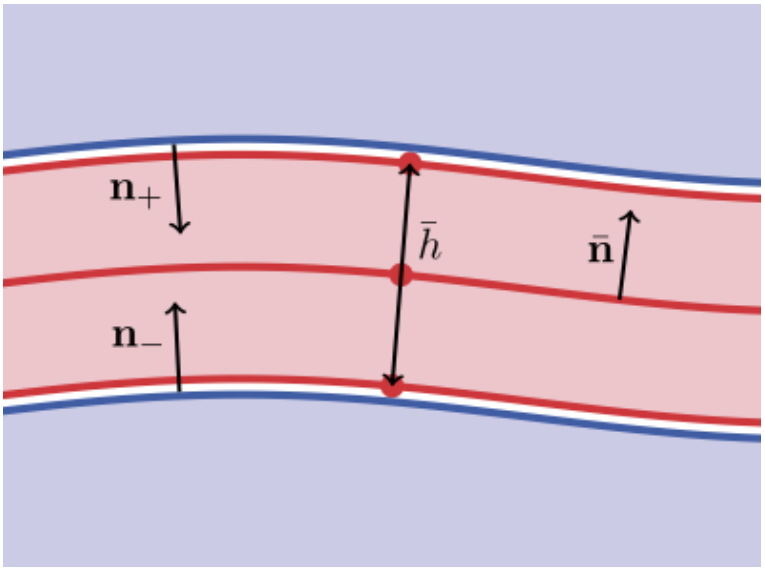

Figure 14: Depiction of an Euler-Bernoulli beam with added thickness h taken from Li et al. [23]. $\boldsymbol{n}_+, \boldsymbol{n}_-$ and $\bar{\boldsymbol{n}}$, denote the normal vector of the upper boundary, lower boundary and mid line. The thickness h is constant in the direction normal to the mid line which in this thesis is represented by a cubic spline.

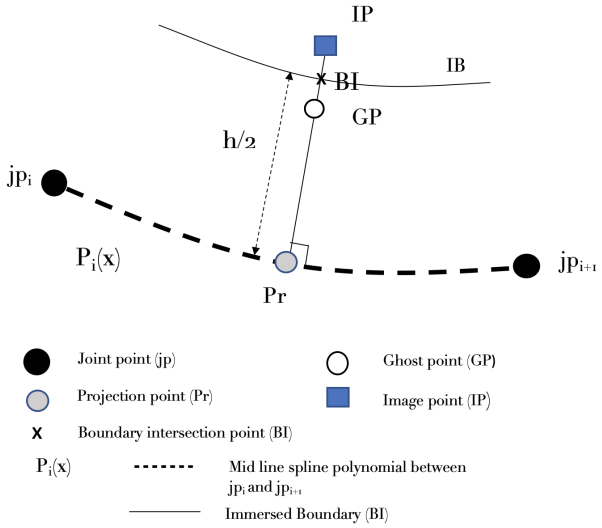

Figure 15: Illustration of projection process to find the image point (IP) of a ghost point (GP) for the flexible plate behind a cylinder test case.

When a point on the grid is identified as a ghost point, the corresponding boundary intersection point (BI) and image point (IP) need to be found. The BI point is the point which a normal probe from the ghost point goes trough, and to simplify the process of finding this point, a trick is used. The boundary can be found by going a distance $h/2$ in the direction of the normal of the mid line curve. Thus by projecting the ghost point onto the mid line curve and then reflect the point a distance $h/2$, the boundary intersection point is found. The process of finding the boundary intersection point and image point for a ghost point (GP) lying between two joint points jp_i and jp_{i+1} connected by a cubic spline $P_i(x)$ is illustrated in figure 15. Let the coordinate of the ghost point be (x_{GP}, y_{GP}) and the coordinate of the the corresponding projection point (Pr) on the mid line curve be equal to $(x, P(x))$. Let a vector $\vec{v} = (x_{GP} - x, y_{GP}) - P(x)$ be a vector starting at the projection point and ending at the the ghost point, and the vector $\vec{t} = (1, P'(x))$ be the tangential vector at the projection point. In order to be the correct normal projection, the dot product $\vec{v} \cdot \vec{t} = 0$ needs to be satisfied, and the following equation can be deduced:

$$F(x) = x_{GP} - x + (y_{GP} - P(x))P'(x) = 0. \tag{55}$$

Due to $P(x)$ being a spline function and the product $P(x)P'(x)$ in equation (55) is a fifth order polynomial, the analytical solution of this equation is almost impossible to find. Thus, the equation was solved numerically using Newton's method with the closest joint point as a first guess. For the function $F(x)$ in (55), the iteration process is:

$$x_{n+1} = x_n - \frac{F(x_n)}{F'(x_n)},$$

where $F'(x) = P''(x)[y_{GP} - P(x)] - P'(x)^2 - 1$. To find the image point, the distance between the ghost point and the boundary intersection point can be added to the boundary intersection point in the direction of $\vec{v}$. Points inside the rounded trailing edge were projected onto joint point N.

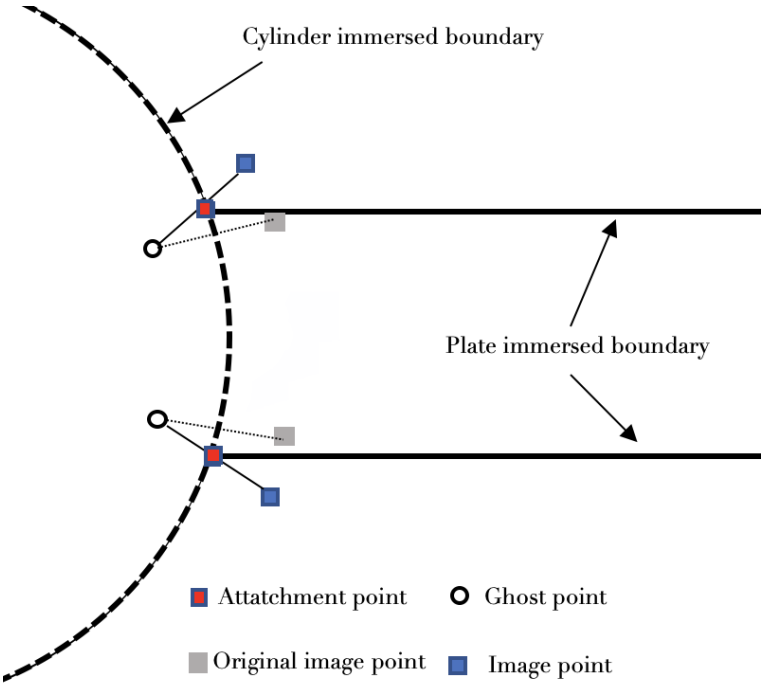

Figure 16: Illustration of how the ghost points near the attachment of the plate at the circular cylinder are treated taken from [36]

One pair of ghost points is occurring within the cylinder, but is reflected into the plate, thus requiring special treatment. As illustrated in figure 16, the image points are instead found by reflection about the attachment points between the cylinder and the plate.

Since the tail is only allowed to move in y-direction, the velocity at the boundary intersection point was set equal to zero. The velocity in y-direction was linearly interpolated between the velocity of the joint points at which the BI points lies in between. Let the BI lie between joint points i and $i+1$. The velocity at these joint points are then $\frac{\partial \phi_i}{\partial t}$ and $\frac{\partial \phi_{i+1}}{\partial t}$, and are found by the Newmark method described in 3.1.4. If d_i and d_{i+1} are the distances between the projection point on the spline curve connecting the joint points i and $i+1$, the velocity at the point BI was set according to $v_{BI} = \frac{d_i}{d_{i+1}} \cdot \frac{\partial \phi_i}{\partial t} + (1 - \frac{d_i}{d_{i+1}}) \cdot \frac{\partial \phi_{i+1}}{\partial t}$. For the pressure, the boundary layer approximation is used, meaning that the pressure gradient at the boundary intersection is zero, and the pressure at the ghost point is equal to that of the image point.

The pressure load δp_i on each joint point i is found equal to the pressure difference between the upper and lower side, i.e. $\delta p_i = p_{i\,upper} - p_{i\,lower}$. The simplest solution to find the pressure at the upper and lower side would be to evaluate the pressure at the boundary intersection point normal to the mid line at the joint points. Since the pressure gradient normal to the surface is equal is equal to zero, the pressure at these points would be well approximated by extending the normal probe a small distance into the fluid domain and evaluate the pressure there. However, this approach led to fast growing instabilities. Thus, the pressure was instead found by summing up the pressure at each ghost point with joint point i as its closest neighbor, and divide by the number of ghost points. The pressure load at the rounded tip 1, was not taken into account.

4 Results and discussion

4.1 Elastically mounted cylinder

The method was tested for the elastically mounted cylinder test case and results were compared to those in the articles by Yang and Stern [51] and Blackburn and Karniadakis [5], and results obtained by Ringstad [36]. Reynolds number and Mach number were equal to Re = 200 and Ma = 0.25 in the present simulations. This means the simulation is in the weakly compressible flow-regime and close to the transitional Reynolds number at which the flow becomes turbulent. Note that the results by Yang and Stern [51] and Blackburn and Karniadakis [5] are obtained for an incompressible flow solver, but the Mach number is low enough so that the compressible effects are assumed not to influence the solution significantly. Cylinder parameters were set to $m^* = \frac{\pi}{4}$, $\rho_s = 1.18$, $\zeta = 0.01$ and $U_* = 5$, the same as for the references.

The simulations were conducted on a $90D \times 40D$ domain, meaning it is larger than the domains used by Yang and Stern and Blackbrun and Karniadakis. According to [51] their domain was large enough to neglect wall effects, and hence also the domain in this thesis should also be. The Navier-Stokes characteristic boundary conditions were used at the inlet and outlet, while symmetry conditions were used for the top and bottom boundaries.

Simulations on three grids of sizes: (441×261), (881×521) and (1044×646) were conducted. In order to give most resolution in the region around the cylinder, the grids consist of nine blocks, three in each direction. Stretching parameters were equal for all grid sizes. In the cylinder block where the grid was Cartesian, and the grid sizes were respectively equal to $D/25$, $D/50$ and $2D/125$. The cylinder was held in place at its equilibrium position at $(20D, 20D)$ until $t' = 520$. After this, it was released and oscillated freely until $t' = 1200$. At that time, the cylinder trajectory did not change and a steady state solution was obtained. The time steps used were $8 \cdot 10^{-3}$ on all three grids, giving a maximum CFL number of approximately 0.25, 0.50, 0.61. Ideally, the time step should have been adjusted so that the CFL number were equal. However, experiments with different time steps showed that it did effect the result in any noticeable way.

Table 2: Table containing results from simulations of an elastically mounted cylinder at $Re = 200$ and $Ma = 0.25$. $\overline{C_D}$ is the average drag-coefficient. $C_L^{'}$ is the peak lift coefficient amplitude. $St = \frac{fD}{u_\infty}$ is the *Strouhal* number, where f represent the vortex shedding frequency. x_c is the center of oscillation measured in offset from the initial cylinder position and u_∞ is the freestream velocity. References for Yang and Stern, Blackburn and Karniadakis and Ringstad can be found in [51] [5] [36], respectivly.

Comparison of results				
Reference	$\overline{C_D}$	$C_L^{'}$	St	x_c
Present 2nd order SBP (441×261) grid	1.7484	0.7574	0.1602	$0.5503D$
Present 2nd order SBP (881×521) grid	1.8884	0.5390	0.1755	$0.5931D$
Present 2nd order SBP (1044×646) grid	1.9117	0.5176	0.1755	$0.60D$
Globally 4th order SBP (881×521)			0.181	$0.616D$
Yang and Stern (fine grid)			0.187	$0.651D$
Blackburn and Karniadakis				$0.62D$

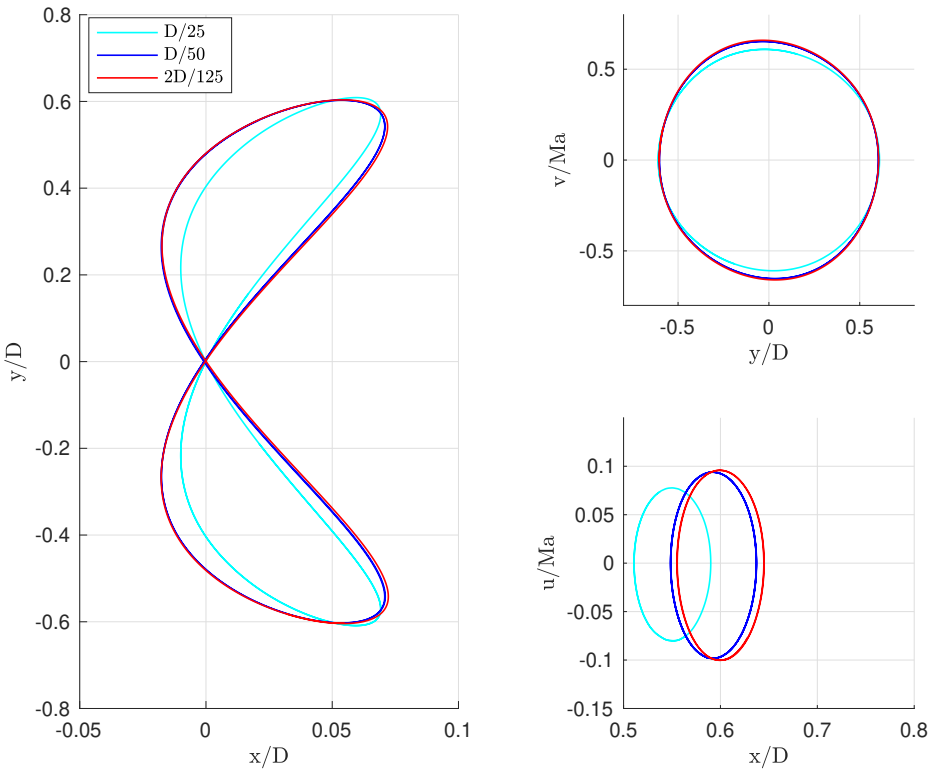

Figure 17: Grid convergence study of the test case elastically mounted cylinder at $Re = 200$ and $Ma = 0.25$ using the 2nd order SBP operator. bright blue: (441×261) grid points and a spacing of $D/25$ close to the cylinder, dark blue: (881×521) grid points and $D/50$ grid spacing close to cylinder, red: (1044×646) grid points and $2D/125$ grid spacing close to cylinder.

At a $Re = 200$, the wake is unstable and a von Karman vortex street appears behind the cylinder. This results in an oscillating drag- and lift coefficient as can be seen in figure 21. The oscillating forces induces cylinder vibrations. In figure 18, the trajectory of the cylinder center from release at $t' = 520$ to $t' = 1200$ for the finest grid is found. It converges into a repeated figure of 8 trajectory at steady state, as can be seen in the grid convergence study in the left sub figure of figure 17. Note that in the left sub figure of 17, the trajectories are moved so that their crossing points are placed at $\boldsymbol{x}_C = (x_c, y_C) = (0, 0)$ in order to make it easier to compare the shape, as is also the case for figures 19 and 25. From the grid refinement study with trajectory plots found in figure 17, it can be seen that displacement in y-direction and the shape of the trajectory has converged, while the displacement in x-direction has not. Both the drag coefficient and hence also the x-coordinate at the crossing point in the trajectory are still increasing as can be seen in table 3. The is probably due to inadequate resolution of the boundary layer, which is a common disadvantage for such Cartesian grid immersed boundary method compared a body-conforming grid [31]. With a body conforming grid, one would be able to use a mesh aligned with the flow field stretching out from the cylinder giving high resolution just where it is needed, as opposed to the present IB method which relies on using the same grid in the whole inner block. Unfortunately, the size of the arrays required to use a finer grid was restricted by the HPC cluster the simulations were run on, and thus a finer grid could unfortunately not be obtained.

Looking at the results in table 2, the Strouhal number seems to have converged. The shedding frequency was found by studying the power spectra obtained by the fast Fourier transform of the lift coefficient and locating the peak frequency. There seemed to be a small interval of frequencies around those given in table 17 making the peek, hence adding some uncertainty to the results. The peak to peak lift coefficient seems to decrease for the three grids. It is not known why this should make intuitive sense. However, the present fine grid results are closest to those in Fig. 4.10 in [36]

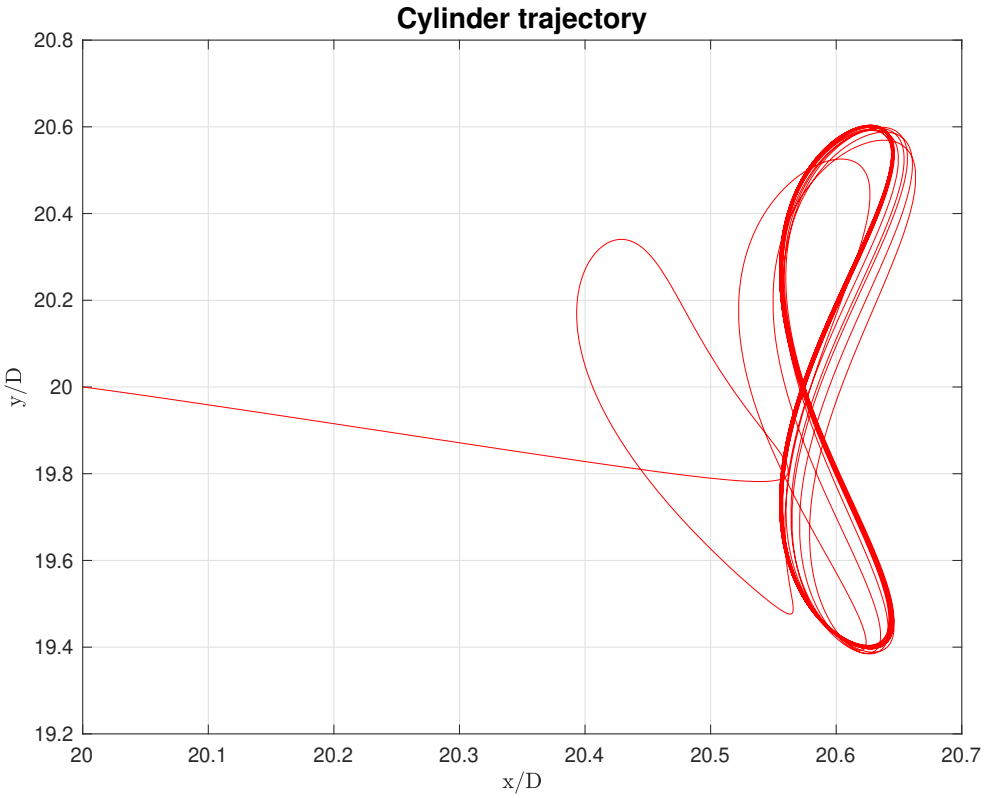

Figure 18: Full cylinder trajectory from the time of release ($t' = 520$) to simulation end ($t' = 1200$) of an elastically mounted cylinder at $Re = 200$, $Ma = 0.25$ and $m^* = \frac{4}{\pi}$ using the present 2nd order SBP method on the fine (1044×646) grid.

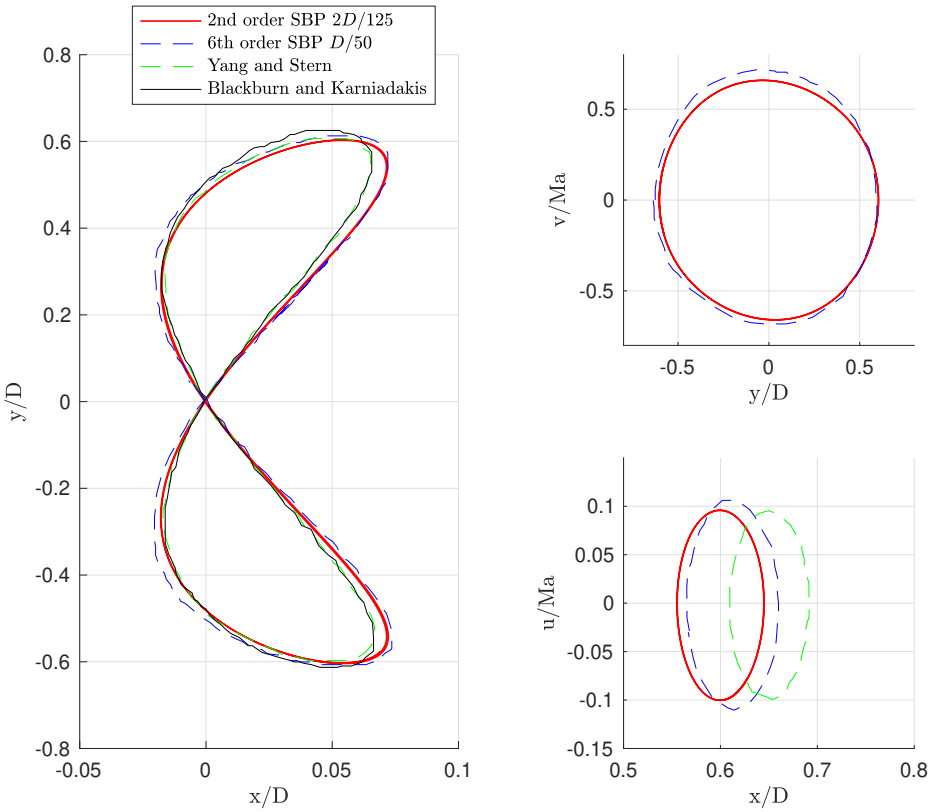

Figure 19: Comparison of cylinder trajectory (left plot), and cylinder velocity components phase plots (right plot) of an elastically mounted cylinder at $Re = 200$, $Ma = 0.25$ and $m^* = \frac{4}{\pi}$. Red solid line: Present 2nd order method on a 1044x646 grid and a $2D/125$ spacing close to the cylinder. Blue dashed line: 6th order SBP [36] method on a (881×521) grid with a $D/50$ grid spacing close to the cylinder. Green dashed line: Yang and Stern [51] results on a fine grid (640×480) grid points) with a grid spacing $D/100$ close to the cylinder. Black dashed line: Blackburn and Karniadakis [5]. Wiggles in the refrence plots occur due to the plot extraction tool.

Comparing the present results to those obtained in literature in table 2 and 19, it can be observed that the displacement in x-direction is greater for all references, with Yang and Sterns [51] being the ones with the largest difference. Ringstad [36] did not either manage to produce exactly matching results using the 6th order SBP method (globally 4th order) on a slightly coarser (881×521) grid with a $D/50$ grid spacing close to the cylinder. Yang and Stern's trajectory and phase plot in the x-direction show a clear grid dependence with the use of their immersed boundary method with a uniform grid around the cylinder [51]. Thus, as mentioned, there is probably some potential for improvement if an even finer grid had been used. When simulating on a coarser and thus more comparable (320×160) large grid with $\Delta = D/50$ grid spacing around the cylinder, Yang and Stern [51] obtained $x_c \approx 0.63D$. When also considering that Yang and Sterns [51] method used for time integration in the fluid solver was of fourth order, their method for spatial disscretization in the fluid solver was of second order, and their method for solving the structural equations was of fourth order, it seems like their method got an advantage over the present GPIBM when it comes to drag predictions.

Looking at the shape of the trajectory in the left sub figure of 19, it can be seen that the present trajectory shape does not match any of the reference trajectories exactly, but is very close to the trajectory found by Ringstad using the 6th order (globally 4th order) SBP method. The resulting trajectories using the SBP method with the ghost point immersed boundary method seem to oscillate in a wider x-interval than the two others. The velocity phase plot in y-direction is almost matching that of the 6th order SBP method (which is exactly equal to that of Yang and Stern), while the shape of the velocity phase plot in x-direction is matching the phase plot of Yang and Stern better than the 6th order method. The computed Strouhal number is lower for the present SBP method than the others, but there remain a small uncertainty around these results because the method used to obtain the vortex shedding frequency for the other methods than the present is not known. All in all, the results do not seem to be too much effected by going down from a globally 4th- order method to a globally 2nd order method, even when comparing results on the same grid. A reason for the small difference in displacement could be that the 2nd order bi-linear interpolation used to approximate the ghost point values (see section 3.2) is a bottleneck on the convergence rate for the higher order GPIBM, which it is not for the present second order method. Another reason for this could be that the results provided by Ringstad in [36] have not properly converged in time, meaning that the simulations should have been run longer to reach steady state.

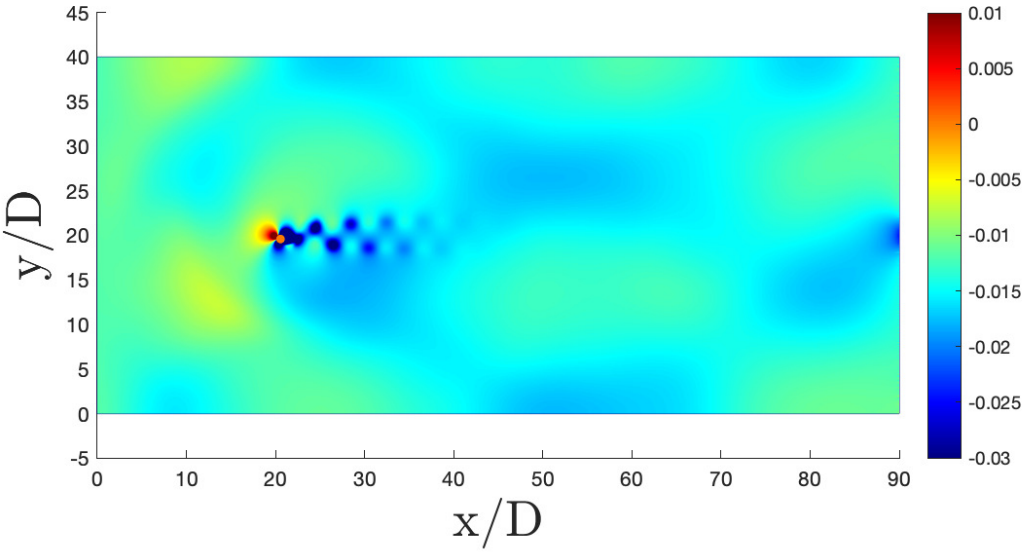

Figure 20: Pressure perturbation contours around an elastically mounted cylinder at $Re = 200$, $Ma = 0.25$ and $m^* = \frac{4}{\pi}$ on the fine (1044×646) grid.

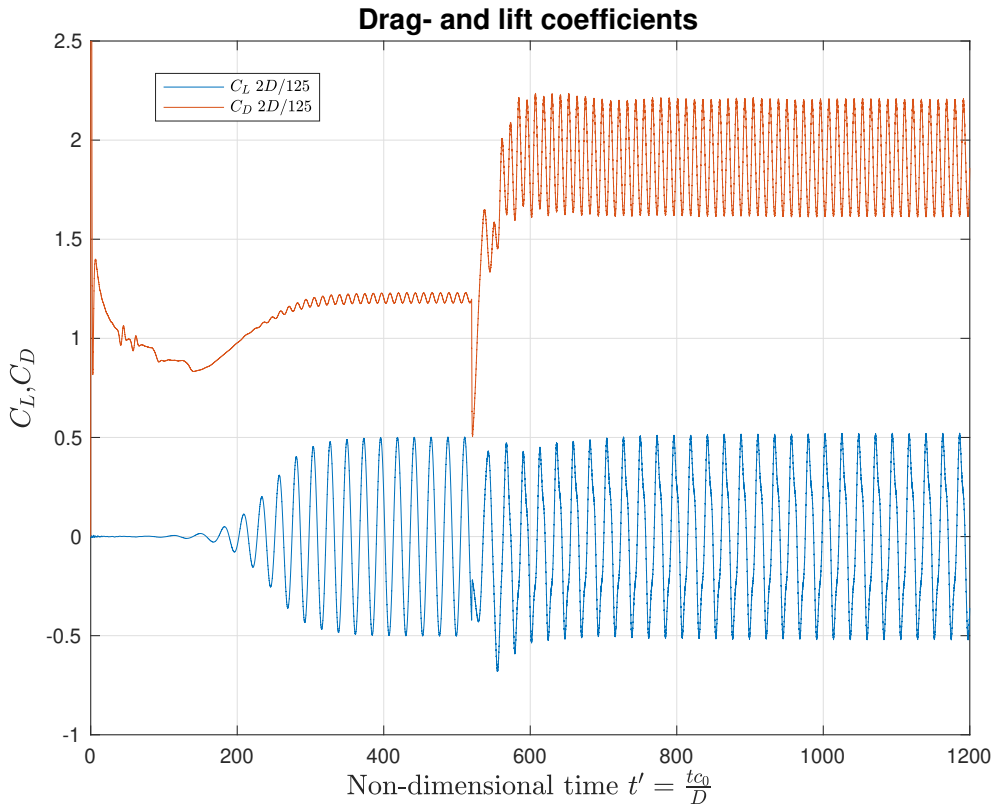

Figure 21: Drag- and lift coefficients on an elastically mounted cylinder at $Re = 200$ and $Ma = 0.25$ using the fine grid (1044×646) grid points).

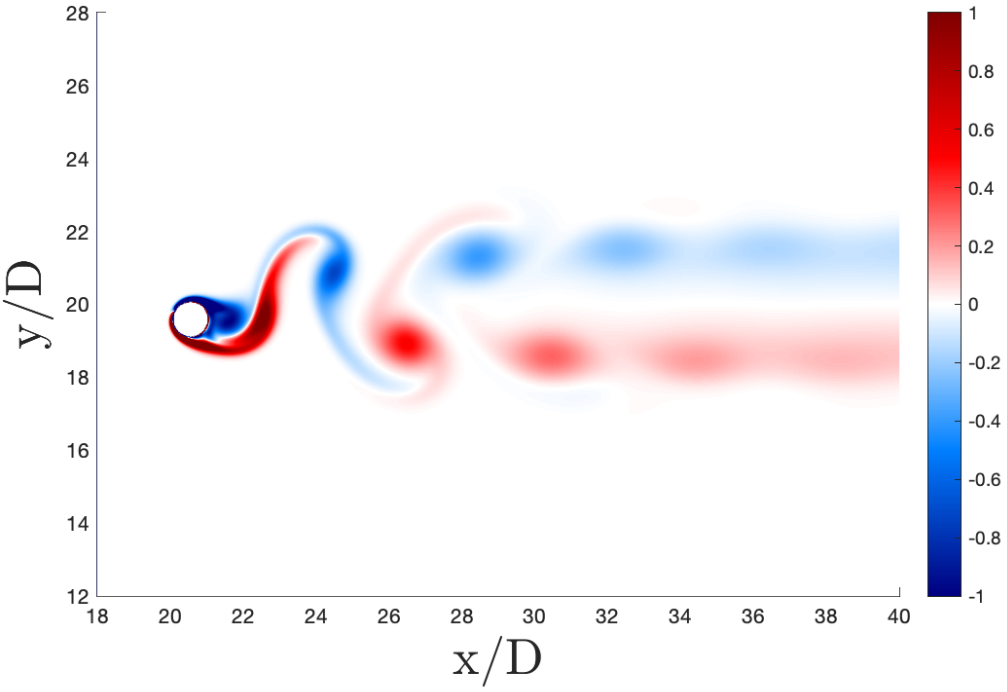

Figure 22: Vorticity contours around an elastically mounted cylinder at $Re = 200$, $Ma = 0.25$ and $m^* = \frac{4}{\pi}$ on the fine (1044×646) grid.

A snapshot of the pressure perturbation contours is found in figure 20. The moving cylinder creates a wake of pressure oscillations due to the von-Karman vortex street. Pressure waves shown as yellow and blue contours are created traveling from the cylinder in all directions and are reflected at the symmetry boundaries. This shows the compressible effect in the simulation. Comparing the pressure contours with those provided by Ringstad [36] for the higher order method, it seems like the pressure contours are sharper for the higher order method. Even tough cylinder displacement results are not too much effected by going down to a second order SBP method, the fluid solver itself seems more effected. The reduction in order might thus make it more difficult to study the acoustics of the flow, which could be important for the flow in the upper airways. The vorticity of the flow field can be calculated from the following formula: $\omega_z = \frac{\partial v}{\partial x} - \frac{\partial u}{\partial y}$. In figure 22 the vorticity contours are plotted when the cylinder has reached the state of repeated 8 figure trajectory. The vortices traveling downstream seem to decay in strength. It is possible that a finer grid would sustain the structure more downstream. Just as for the acoustic effect, reducing the order of the method influence the sharpness of the vortex shedding pattern.

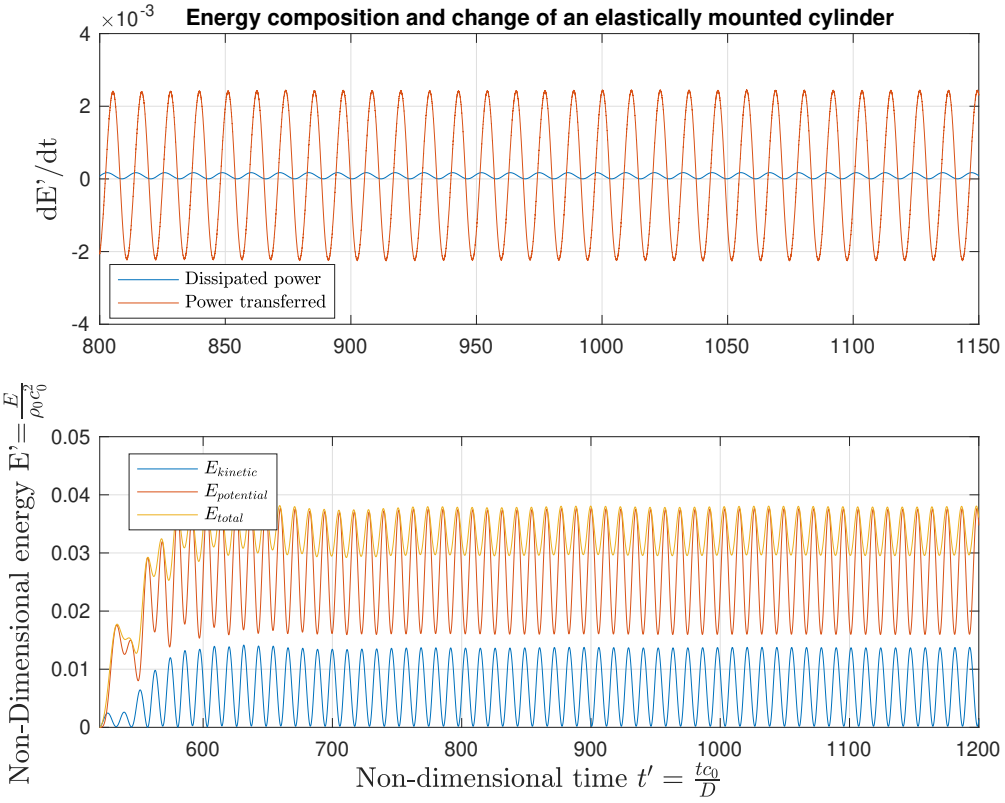

Figure 23: Simulation of an elastically mounted cylinder at $Re = 200$ and $Ma = 0.25$ using the fine grid ((1044 × 646)) grid points). Upper: Dimensionless power added, $\frac{F_D u + F_L v}{\frac{\rho_0 c_0^3}{D}}$, (power transferred) and dimensionless power lost, $\frac{bu^2 + bv^2}{\frac{\rho_0 c_0^3}{D}}$, (dissipated power) by the structure ODE as a function of dimensionless time. Lower: kinetic- potential and total energy of the structure as function of dimensionless time on a (441 × 261) grid (see equation (24)).

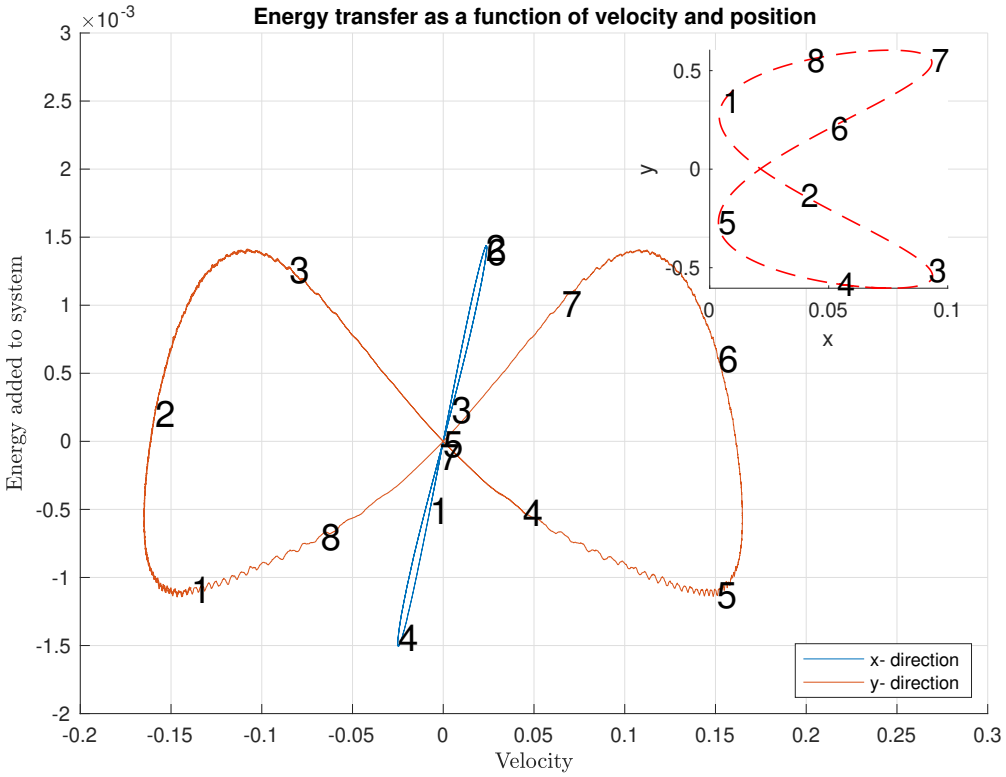

Figure 24: Simulation of an elastically mounted cylinder at $Re = 200$ and $Ma = 0.25$ using the fine grid ((1044×646)) grid points). The main plot shows dimensionless net power added at different cylinder velocities in x- and y-direction. Blue line: $\frac{F_D u - bu^2}{\frac{\rho_0 c_0^3}{D}}$, orange line: $\frac{F_L v - bv^2}{\frac{\rho_0 c_0^3}{D}}$. (Upper right) The corresponding position at different times **1-8** during the cylinder trajectory.

Equation (25) tells that there are two mechanisms leading to energy change of the cylinder, power transferred between the flow and the structure, and energy dissipated in the damper. In the upper part of figure 23 the two components contributing to the energy change are plotted in non-dimensional form. The power transferred is much larger than the power dissipated, which is needed to sustain the motion of the cylinder. Studying the figures carefully, it appears that the peak positive value of the transfer term is slightly larger than the peak negative value, meaning that there is more transferred to the cylinder than what is transferred from the cylinder. This is in accordance with equation (25) and (24) since a similar amount of power as the difference seems to be lost in the damper. In the lower part of figure 23, the total energy of the cylinder and the two components it consists of is plotted. The plot shows that the total energy is equal the sum of the kinetic and potential as stated in (24). The potential energy is larger than the kinetic energy due to the cylinder offset in x-direction creating a constant storage of energy in the spring equal to $E_c = \frac{1}{2} k {x_C}^2$. Figure 24 shows how the energy transfer in both x- and y-directions varies with velocity and place in the obtained periodic trajectory. In the upper right corner, the trajectory of the cylinder in the xy-plane is plotted. The numbers **1-8** indicate where in the trajectory the cylinder is located, meaning the energy transfer as function of velocity can be mapped onto its corresponding position in the cylinder trajectory. The energy transfer seems to be symmetric over one period. This is in agreement with the intuition of what one would expect from such a

system since the majority of the energy is transferred back and forth between the cylinder and the fluid [2]. Note that **1**-**8** are distributed through the whole trajectory, while the motion in x-direction completes two whole periods through the whole 8-figure movement. Starting at point **1**, the cylinder is pushed by the flow field and the potential energy built up in the spring through the crossing point where the net potential energy due to displacement of the spring in y-direction is equal to zero. As more and more potential energy is built up and the energy transfer in both direction peaks, the forces exerted by the spring overcomes that of the flow field as the cylinder passes point **3** and the cylinder changes x-direction. A little bit after that, slightly before **4**, the peak y-displacement is also reached. The potential energy in the spring is then transferred into kinetic energy which is moving the cylinder against the flow field transferring energy from the cylinder to the flow until point **5** in x-direction and the crossing point in y-direction. The cycle then repeats with the same characteristic motion in x-direction and the same motion in y-direction except for a change in sign for the v-velocity. Through careful inspection, it can be seen that the energy transfer in x-direction is highest at point **4** and **8** where the cylinder has just passed its the peak y-coordinate, and slightly after the cylinder move through the crossing point at **2**. The energy transfer in y-direction seems to be strongest around point **1**, **3**, **5** and **7** where the $F_L v$ peaks.

Small oscillations in the energy transfer in y-direction are found in 24 close to the peak velocities. These were also found by Ringstad [36] and Khalili et al. [9] using the globally 4th order SBP method for the with the ghost point immersed boundary method. It was speculated in Khalili et al. [9] that this is a result of the artificial added mass effect mentioned in the introduction creating spurious force oscillations on moving interfaces arising for sharp interface method such as this GP IBM. Seo and Mittal [38] suggested that the effect is a result of violations of geometric conservation laws when fresh fluid points appear and old solid nodes disappear. The problem seems to disappear for finer grids, and for the present method on the finest grid the wiggles are not very prounounced.

4.1.1 Effect of filtering

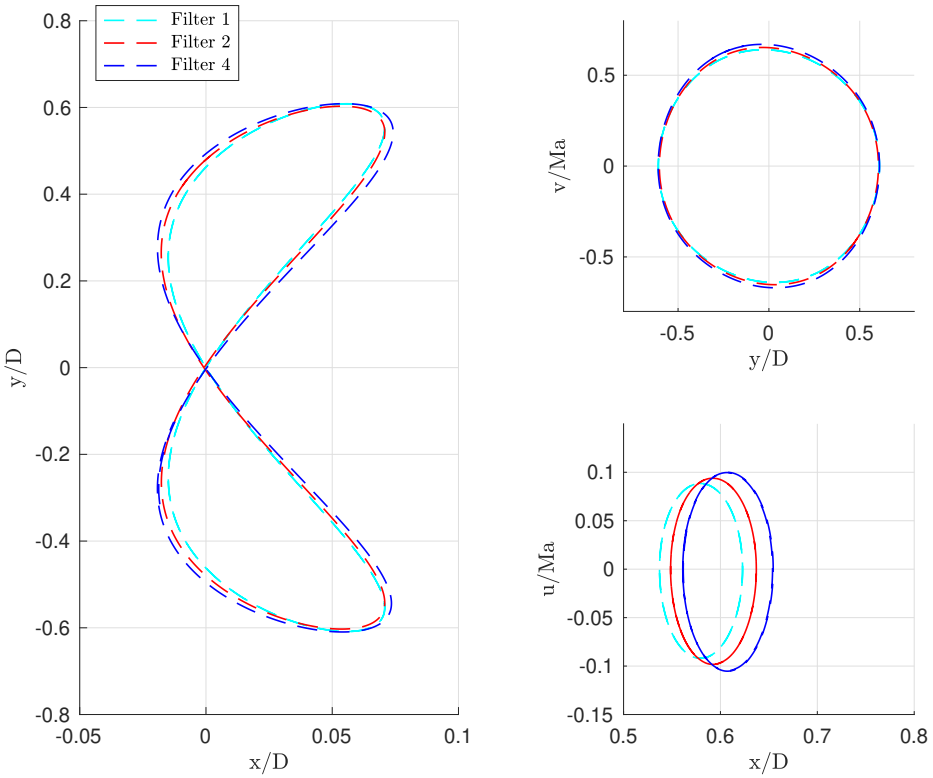

Figure 25: Effect of filtering each nth time step on an elastically mounted cylinder at $Re = 200$ and $Ma = 0.25$. The simulations were done using the 2nd order SBP method on a (881×521) grid. Cyan line: filtering every step. Red line: filtering every other step. Blue line filtering each fourth step.

Table 3: Comparison of center displacement and Strouhal number $St = \frac{fD}{u_\infty}$ for an elastically mounted cylinder at $Re = 200$ and $Ma = 0.25$ filtering every nth time step. Simulations are done on a (881×521) grid.

X-displacement and Strouhal number for different filtering steps		
Filter nth time step	x_c	St
Filter 1	$0.5803D$	0.1679
Filter 2	$0.5931D$	0.1755
Filter 4	$0.6079D$	0.1755

As discussed in section 3.1.2, the filter used to remove dispersed wave modes is also removing non dispersed modes, meaning that the filter is too dissipative. To illustrate the problems that arise, if simulations were conducted on a (441×261) grid without any filtering, the simulation ends up in instability. If the filter was applied each time step on the same grid, no vortex shedding would appear and consequently no vibrations would be induced. To have a stable simulation with vortex

shedding able to induce cylinder vibration, the filter was only applied every second time step. Results from a study where the filter is applied each *nth* time step on a (881×521) grid is found in figure 25 and table 3. The reduced dissipation seems to give a significantly higher x-displacement, and a trajectory more coincident with that found with the 6th order SBP method in figure 19. However, the peak velocity in x-direction found in the lower subplot to the right of figure 25 seems to be higher than that found by Yang and Stern [51]. Any effect on the Strouhal number seems to be gone when the frequency of the filtering is reduced to any other time step. There is thus a trade-off when deciding how often the filter should be applied.
Results using the second order filter every fourth time step (filter 4) in figure 25 seems to be in better accordance with the wave number resolution of the second order SBP method. However, this would require an extra layer of ghost point if it is going to be applied at all nodes where the second order central difference approximation is used. Maybe some special boundary treatment could make the fourth order filter applicable, or that a fourth order filter is used in the interior of the fluid domain where enough fluid or ghost points are available, and that a second order filter is used closer to the boundary. Nevertheless, how much added dissipation is needed is also a question of which grid size is used. For very fine grids, almost all modes are resolved, and maybe a second order filter applied every fourth time step is the best and simplest solution. For simulations where courser grids are used, there would be a need for more experimentation to tune how often the filter should be applied. Furthermore, since the wave modes present in a flow problem will vary, the interval between each filtering will also be different.

4.2 Flexible plate behind a plate

The cylinder of a diameter $D = 0.1[m]$ with an attached plate of length $l = 3.5D$ and thickness $h = 0.2D$ is placed in a 2D channel of height $H = 4.1D$ and length $L = 90D$. The centre of the cylinder is placed at the coordinate $x_0 = 20D, y_0 = 2D$ A depiction of the computational domain of the test case is found in figure 26. Note that in the paper by Turek and Hron [45], the channel is only $25D$ long, and the cylinder centre x-coordinate is $2D$. The extension was done in order to reduce the effect of using a compressible flow solver instead of an incompressible as done in Turek and Hron[45].

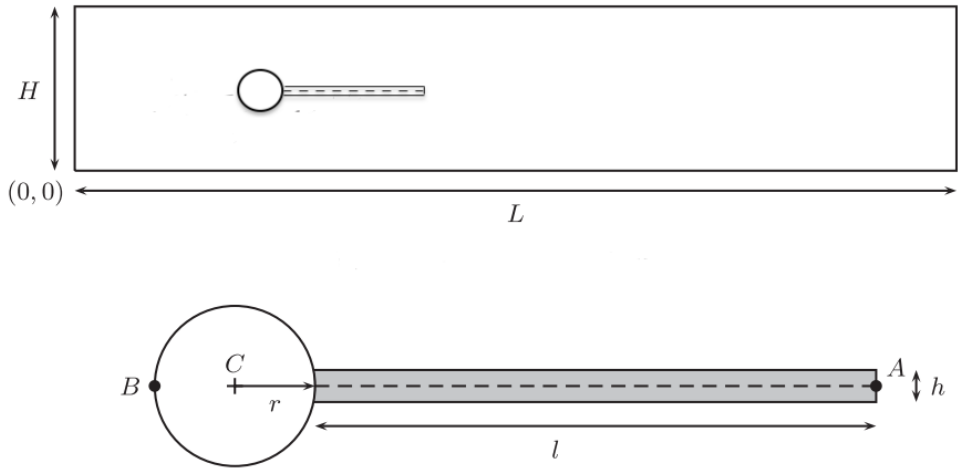

Figure 26: Illustration of computational domain (upper) and structural detail (Lower) of the test case flexible plate behind cylinder [45]. $L = 90D$, $C = (20D, 2D)$, $l = 3.5D$, $h = 0.2D$.

The grid used contains 971 nodes in x-direction and 369 nodes in y-direction. The domain is divided into nine blocks, three in both directions. A grid stretching is used to get high resolution closer to the structure laying in the middle block, which is located between $x = 18D$ and $x = 24.5D$, and $y = 1D$ and $3D$. In the middle block, a uniform grid of size (401×201) was used, giving a grid spacing of $\Delta x = \frac{6.5D}{400}$ and $\Delta y = \frac{D}{100}$. The boundary condition at the walls and structure were no-slip, adiabatic and zero normal pressure gradient. At the outlet, the pressure was set to ambient, i.e. the perturbation pressure was set to zero. The inlet velocity profile was set according to Turek and Hron [45], which in non-dimensional form becomes:

$$u_0(y^*) = 1.5Ma_\infty \frac{4}{(\frac{H}{D})^2} y^*(\frac{H}{D} - y^*), \tag{56}$$

where $y^* = y/D$ is the non-dimensional y-coordinate, $Ma = \frac{\overline{U}}{c_0}$ is the Mach number, where $\overline{U}$ is the mean inflow velocity. As suggested in Turek and Hron [45], the inlet velocity was smoothly increased from zero to u_0 according to:

$$u(0, y, t) = \begin{cases} u_0(y) \left(\frac{1-cos(\frac{\pi}{2}t)}{2}\right), & \text{if } t \leq 2[\text{s}] \\ u_0(y) & \text{otherwise} \end{cases} \tag{57}$$

.

Initially the velocities at other nodes were set equal to zero. When it comes to the time of release of the geometry, there did not seem to be any effect on the tail displacement after a while, and different times were thus used.

In the paper by Turek and Hron [45], different sets of parameters are used in the simulation. Simulations for two of these sets, FSI1 and FSI2, were conducted. A summary of the parameters is found in table 4. The parameters presented in the table are the fluid density ρ_f , the fluid kinematic viscosity ν_f, the undisturbed fluid velocity U_∞, the flow Mach number $Ma_\infty = \frac{U_\infty}{c_0}$, Reynolds number $Re = \frac{U_\infty D}{\nu_f}$, the structure mass density ρ_s, the structure elastic Young's modulus E, and the structure Poisson ratio ν_s. In addition to this, some modifications had to be made in order to adapt the solver intended for gas dynamics (compressible flow) to that of an incompressible. Since the governing equations are solved in non-dimensional form using the speed of sound as a velocity scale, the speed of sound (c_0) was set artificially low to speed up the simulations. For FSI1, the speed of sound was set to $c_0 = 1m/s$ and for FSI2 it was set to $c_0 = 3m/s$. This would increase the Mach number to $Ma_\infty = 0.20$ for FSI1 and $Ma_\infty = 1/3$ for FSI2. However the Mach number should be low enough to make compressible effects negligible [36]. The working medium of the flow-solver was air, and thus both the density of the fluid and the solid were reduced by a factor $\frac{\rho_f}{\rho_{air}}$ so that the gas density is equal to the the air density ρ_{air}, and the solid-fluid density ratio was equal to that provided by Turek and Hron in [45].

Table 4: Parameters set for the plate and fluid models in the benchmark of Turek and Hron [45], except ρ_s and ρ_f which were both set 10^3 times higher in [45] at $10^3[\frac{\text{kg}}{\text{m}^3}]$ [36].

		FSI1	FSI2
ρ_f	$1\frac{\text{kg}}{\text{m}^3}$	1.18	1.18
ν_f	$10^{-3}\frac{\text{m}^2}{\text{s}}$	1	1
U_∞	$1\frac{\text{m}}{\text{s}}$	0.2	1
Ma_∞	-	0.2	1/3
Re	-	20	100
ρ_s	$1\frac{\text{kg}}{\text{m}^3}$	1.18	11.8
E	$10^6\frac{\text{kg}}{\text{ms}^2}$	1.4	1.4
ν_s	-	0.4	0.4

To sum up the results before going trough them, the simulations were prone to instabilities and are therefore difficult to compare top the benchmark results provided by Turek and Hron. However, the results are promising, and to highlight different aspects of them, results for both FSI1 and FSI2 are provided with some modifications. Simulations were conducted with different time steps, different intervals between filtering. In the reference paper, Turek and Hron provide benchmark results for the tip displacement, i.e. the displacement of point A in figure 26, and the sum of drag and lift. Since the Euler-Bernoulli beam model only assumes displacement in y-direction, only the displacement of point A in y-direction is studied in this thesis. Also, when referring to the tip displacement, the point A is the position of the last joint point, not the tip of the rounded edge. For FSI1, Turek and Hron reached a steady displacement of $\phi_A = 0.8209 \cdot 10^{-3}[m]$. For FSI2, the tips oscillates between the peak values $\phi_A = (1.23 \pm 80.6) \cdot 10^{-3}[m]$.

4.2.1 Simulations of FSI1

The results from FSI1 are promising as the tips displacement seem to converge to a steady displacement close to that of Turek and Hron. First, consider the results provided by the simulation applying the filter every 8th time step found in figure 27 to 32. As can be observed in figure 27, the tip first oscillates up to a value close to the reference displacement at $t \approx 7.5$ before these larger oscillations decay and the tip becomes more steady. However, small rapid oscillations start to occur which soon increase in size and the system ends up in instability.

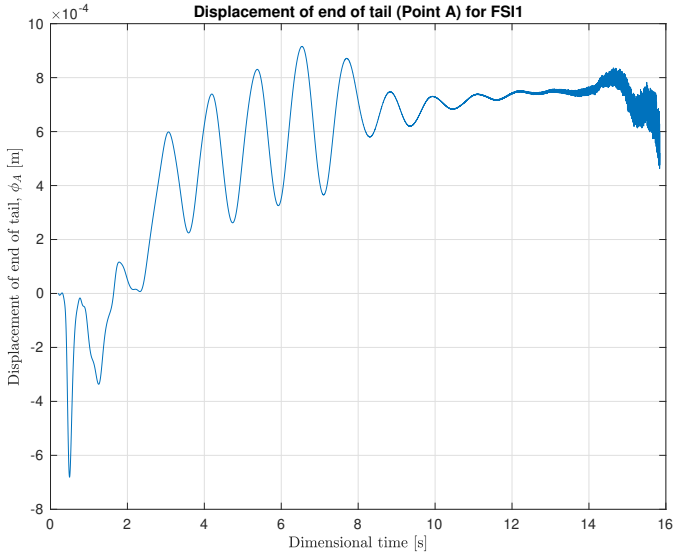

Figure 27: Displacement of end point A for the FSI1 setup using the present 2nd order SBP method. A non dimensional time step o $dt' = 1 \cdot 10^{-3}$ is used, and the second order low-pass filter is applied every 8th time step.

Looking at the full tail displacement in figure 28, it seems like the tail is stretched out and moves up and down when the frequent tip oscillations found in figure 27 first occur. When the tip oscillations start to become pronounced, oscillations in the tail start to show, before they also increase in amplitude as the instability grows. The root of these instability is thought to be the pressure load, which is plotted in figure 36. At first, the pressure load seems to be continuous, but after a while, spikes and oscillations start to show up. This strange pressure load pattern seems to occur before the oscillations in the tail displacement, and grows at a higher rate. Since velocities and pressure loads becomes larger, more and more energy is transferred to the plate. Figure 31 shows how the power transfer is very small at first, but scales with the instability. In figure 30, the pressure contours is are plotted close to the point of instability. Observe the bumps in perturbation pressure close to the plate. The frequently oscillating plate interacts with the flow field, and the instability propagates into the fluid. In figure 32, one can observe the small bumps in the plate creating small eddies which grow in size.

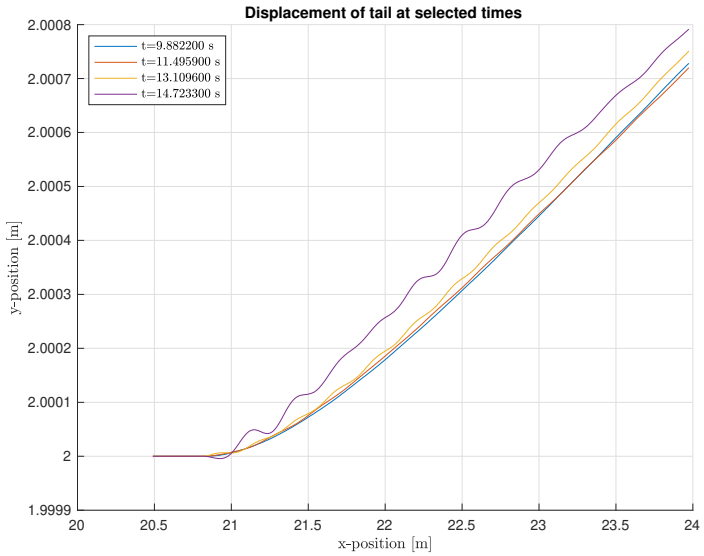

Figure 28: Displacement of tail at selected times for the FSI1 setup using the present 2nd order SBP method. A non dimensional time step of $dt' = 1 \cdot 10^{-3}$ is used and, the second order low-pass filter is applied every 8th time step.

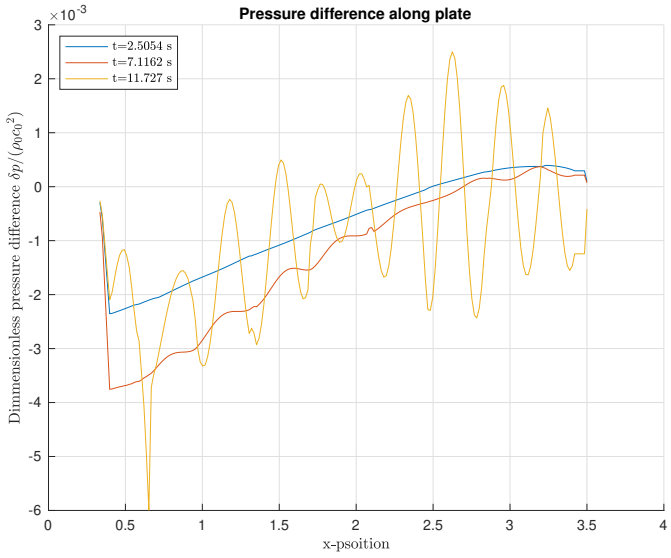

Figure 29: Non dimensional pressure difference along tail at selected times for the FSI1 setup using the present 2nd order SBP method. A non dimensional time step of $dt' = 1 \cdot 10^{-3}$ is used, and the second order low-pass filter is applied every 8th time step.

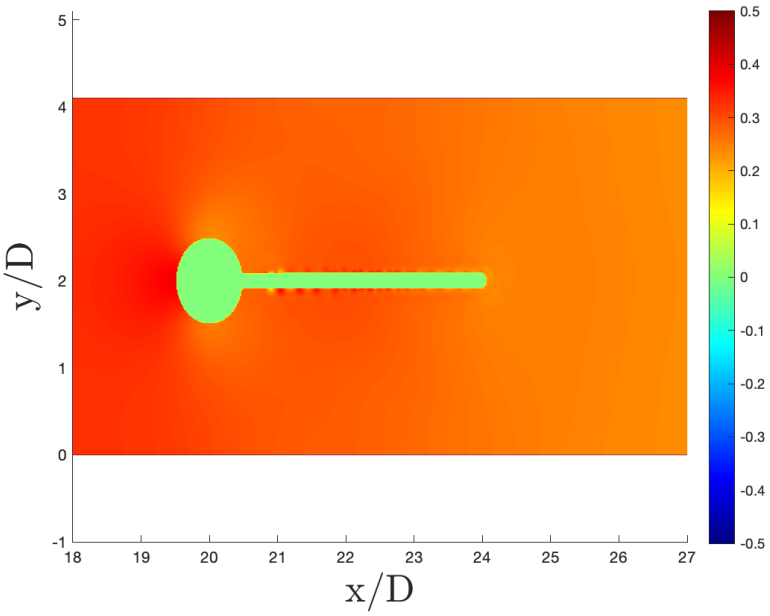

Figure 30: Pressure perturbation contours for the FSI1 setup using the present 2nd order SBP method close to time of instability. A non dimensional time step of $dt' = 1 \cdot 10^{-3}$ is used, and the second order low-pass filter is applied every 8th time step.

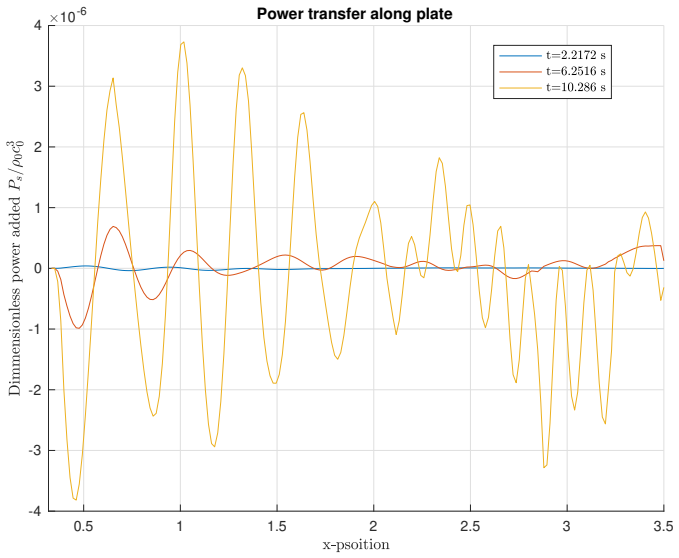

Figure 31: Non dimensional power transfer $P_s = -\delta p \dot{\phi}/(\rho_s c_0^3)$ along tail at selected times for the FSI1 setup using the present 2nd order SBP method. A non dimensional time step of $dt' = 1 \cdot 10^{-3}$ is used, and the second order low-pass filter is applied every 8th time step.

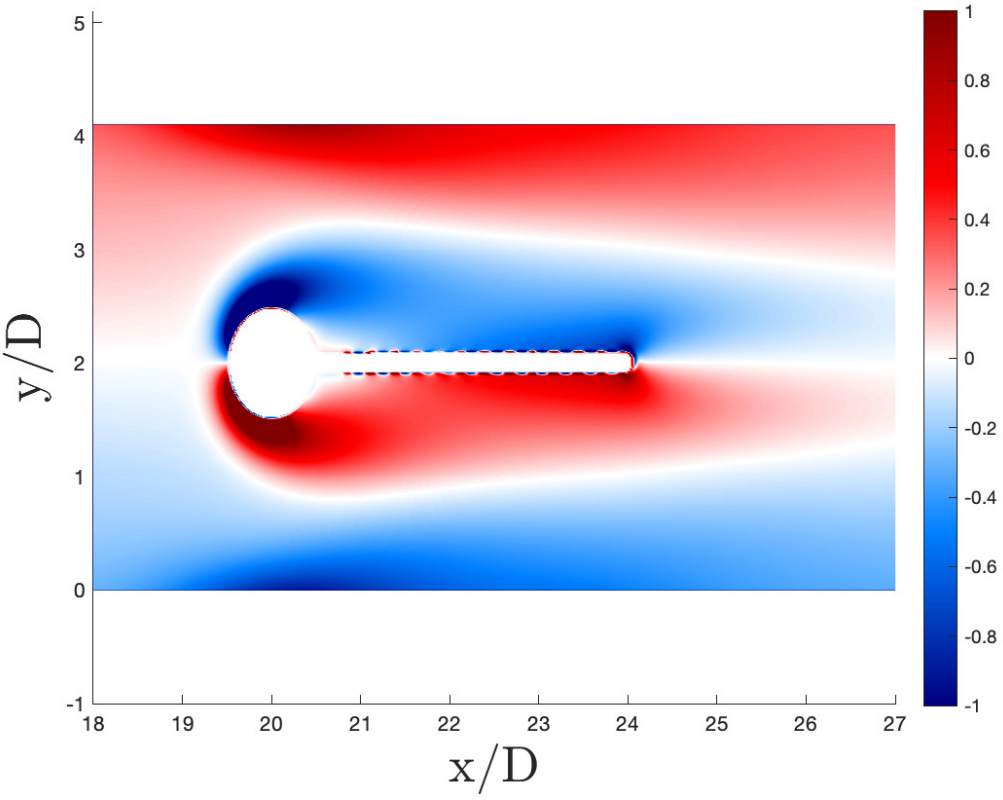

Figure 32: Instantaneous vorticity contours for the FSI1 setup using the present 2nd order SBP method close to time of instability. A non dimensional time step of $dt' = 1 \cdot 10^{-3}$ is used, and the second order low-pass filter is applied every 8th time step.

Reducing the amount of time steps before each filtering does not solve the problem of instability. In figure 33, the tip displacement from two simulations using a non dimensional time step of $dt' = 1 \cdot 10^{-3}$ and $dt' = 0.5 \cdot 10^{-3}$, and the second order filter every 4th time step are shown. Comparing the results in figure 33 with that in figure 28, the instability seems to occur earlier when the interval between each filtering is reduced by a factor of two. Also, the magnitude of the displacement gets smaller, since more energy is removed from the fluid solver due to increased use of filtering. When the time step is halved, the instability seems to occur later, but is still present in figure 33. Note that in figure 33, the tail is released later in the simulation using a time step of $dt' = 0.5 \cdot 10^{-3}$, which probably contributes to the slower growth in tail displacement.

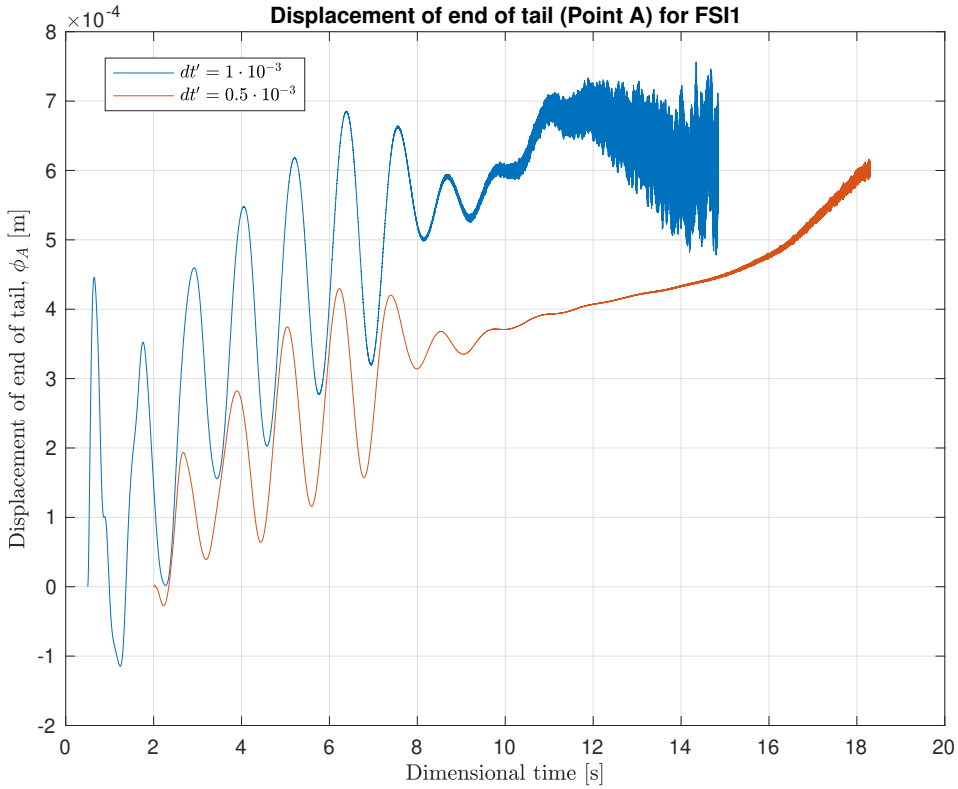

Figure 33: Displacement of end point A for the FSI1 setup using the present 2nd order SBP method. A non dimensional time step of $dt' = 1 \cdot 10^{-3}$ and $dt' = 0.5 \cdot 10^{-3}$ is used, and the second order low-pass filter is applied every 4th time step.

The pressure spikes and oscillations were also found by Ringstad in his master thesis [36] for the same test-case with the same procedure of finding the pressure load and criteria to find points inside the solid domain. For the FSI2 setup, the simulation became unstable following a pattern similar to the one described with growing oscillations. For the FSI1 setup, the procedure seemed to converge, but it is possible that an instability would also be found for this setup. The way of finding the pressure load from the fluid on the joint points by taking the average of the pressure load at the closest ghost points, and interpolate the pressure at nearby joint points to find the pressure at joint points without any "closest" ghost points, was suggested by Ringstad to be the main reason for these spikes and instability. During the work on the present thesis, any attempts on using other methods to find the pressure load on the plate than the one proposed by Ringstad ended up in much faster growing instabilities than the present method. Regardless of this, as mentioned in the introduction, pressure oscillations are normal in sharp interface methods like the ghost point immersed boundary method. In the results from the elastically mounted cylinder test-case in presented in section 4.1, small oscillations did occur in figure 24, and were also found by Khalili et al. in [9]. These so called artificial added mass effects tend to become stronger for lower solid-fluid density ratio $\frac{\rho_s}{\rho_f}$, higher Reynolds number Re, and long slender structures like plate in elastically mounted plate behind a cylinder [42] [18] [38].
To asses the effect of the artificial added mass effect, a simulation using the same parameter setup for FSI1 as found in table 1 but with a ten times larger solid-fluid density ratio, i.e. $\frac{\rho_s}{\rho_f} = 10$,

was conducted. The non-dimensional time step used in the simulation was $dt' = 1 \cdot 10^{-3}$, and the filter was applied every 4th time step. The results are found in figure 34-36. In contrast to the simulations using the same density ratio as Turek and Hron [45], this simulation is not unstable and converge to a tip displacement of $\phi_A = 7.524 \cdot 10^{-3}[m]$. Some pressure spikes seem to arise and stay in the simulation as seen in figure 36, but at one point they apparently stop growing and stay as a part of the steady solution. The displacement along the whole plate found in figure 35 converges to a steady state without any oscillations. In the vorticity contour plot in figure 37, there are no sign of a perturbed surface creating a strange pattern close to the plot. Thus, one could speculate that the instabilities are not solely caused by an inadequate implementation, and all the simplifications done compared to the original test problem.

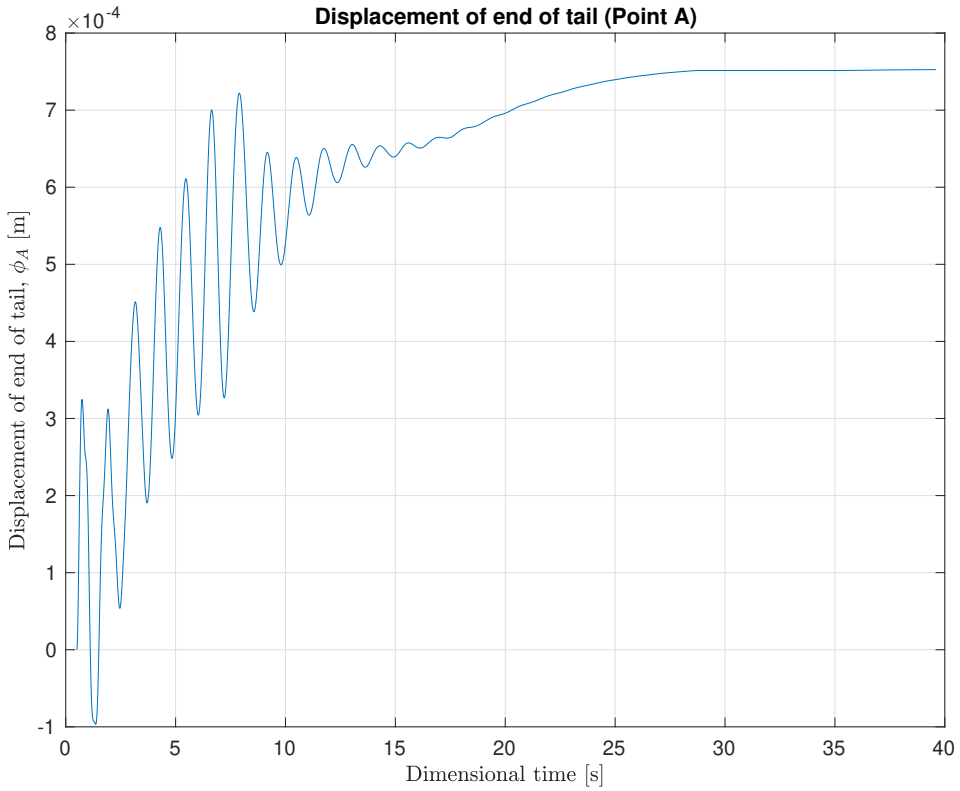

Figure 34: Displacement of end point A for the FSI1 setup with a ten times larger density ratio ($\rho_s/\rho_f = 10$) using the present 2nd order SBP method. A non dimensional time step of $dt' = 1 \cdot 10^{-3}$ is used, and the second order low-pass filter is applied every 4th time step.

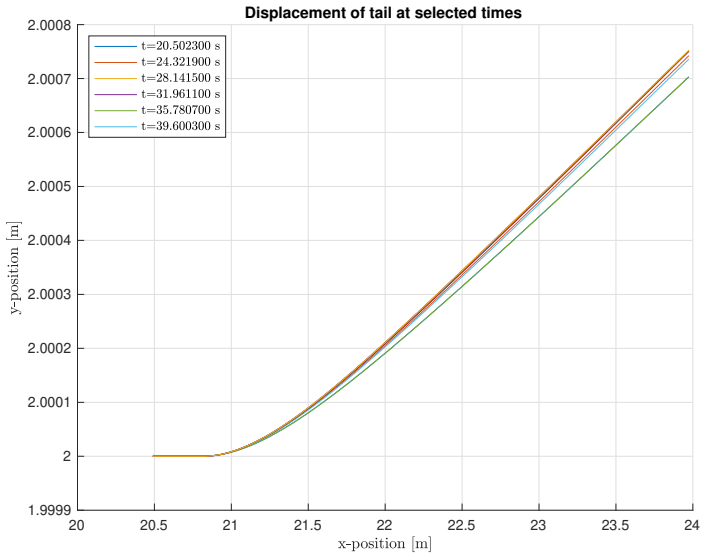

Figure 35: Displacement of tail at selected times for the FSI1 setup with a ten times larger density ratio ($\rho_s/\rho_f = 10$) using the present 2nd order SBP method. A non dimensional time step of $dt' = 1 \cdot 10^{-3}$ is used and, the second order low-pass filter is applied every 4th time step.

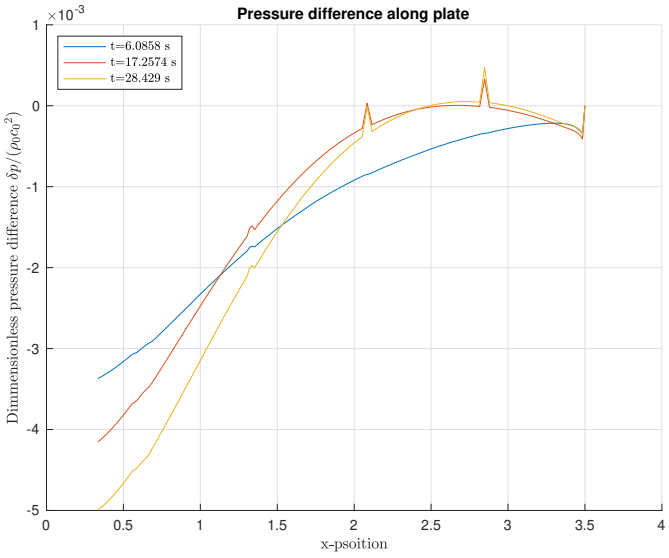

Figure 36: Non dimensional pressure difference along tail at selected times for the FSI1 setup with a ten times larger density ratio ($\rho_s/\rho_f = 10$) using the present 2nd order SBP method. A non dimensional time step of $dt' = 1 \cdot 10^{-3}$ is used, and the second order low-pass filter is applied every 4th time step.

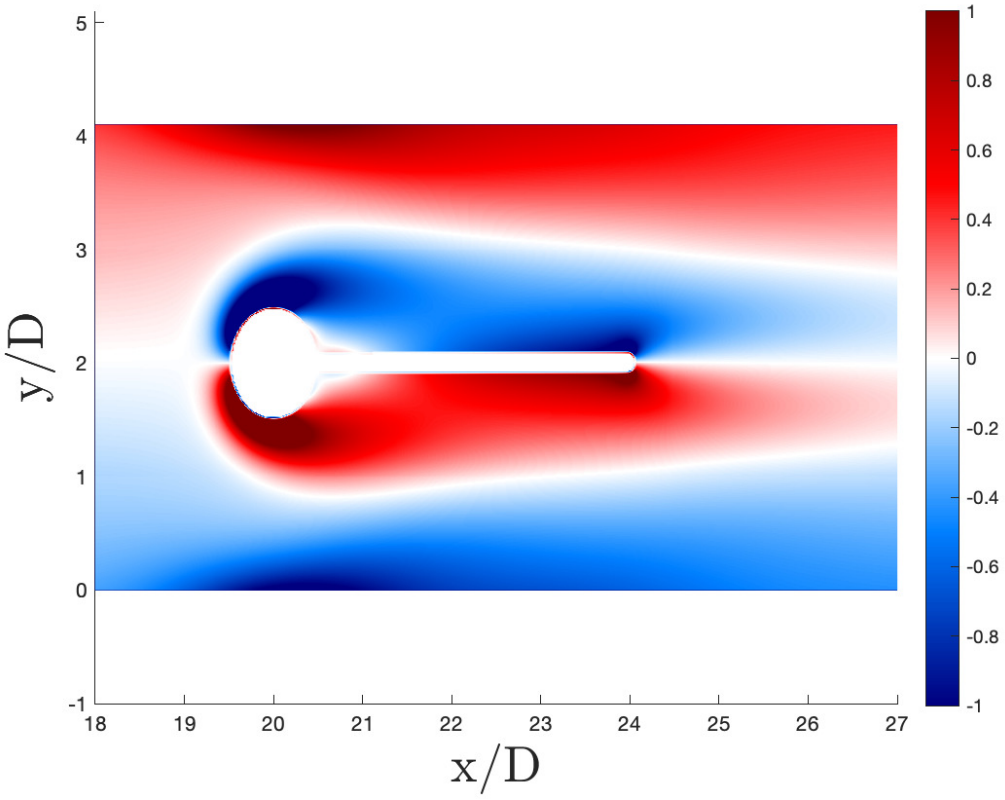

Figure 37: Instantaneous vorticity contours for the FSI1 setup with a ten times larger density ratio ($\rho_s/\rho_f = 10$) using the present 2nd order SBP method close to time of instability. A non dimensional time step of $dt' = 1 \cdot 10^{-3}$ is used, and the second order low-pass filter is applied every 4th time step.

4.2.2 Simulations of FSI2

A simulation using the parameter setup for FSI2 found in table 1 was conducted using a non-dimensional time step equal to $dt' = 3 \cdot 10^{-3}$ and the second order filter every 8th time step. The resulting tip-displacement is found in figure 38. At peak, the tip oscillates between approximately $-0.55[m]$ and $0.59[m]$, which means that it do not reach the displacement of the reference solution by Turek and Hron [45]. Also, the period is approximately $0.3[s]$, which is half of the period of $0.6[s]$ that of Turek and Hron. If it had not been for the instability, the amplitude and period might have grown into the correct one. Using a modified version of the higher order GPIBM with a straight lines connecting the joint points, Ringstad [36] barley obtained a tip displacement close to that of Turek and Hron[45] before instability occurred. A smaller or at least more slowly growing amplitude in the plate displacement is a probable effect of going down to second order, but since there are setup differences and instabilities occurring, no conclusion can be drawn. Nevertheless, results are promising also for the FSI2 simulation setup. Considering that larger deflections also occur, it might be that the Euler-Bernoulli beam model is pushed towards the validity limit, and that this is the reason that the tip displacement amplitude seem to reach a limit at which it stays for a while before decaying, and the simulation stops.

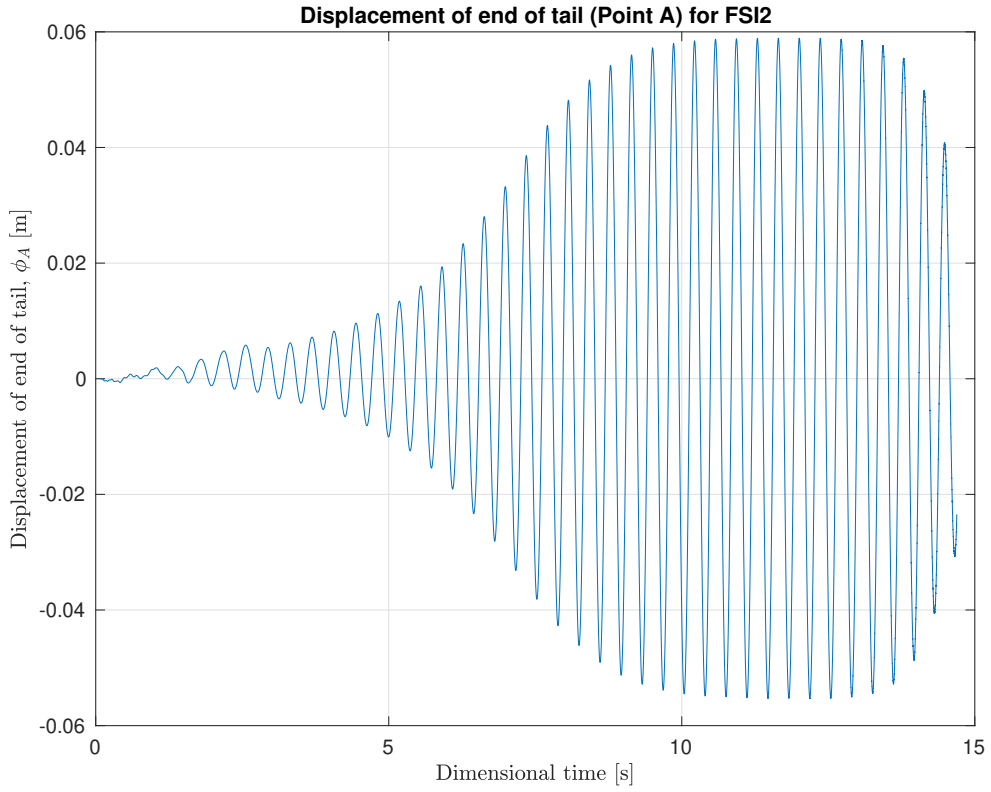

Figure 38: Displacement of end point A for the FSI2 setup using the present 2nd order SBP method. A non dimensional time step of $dt' = 3 \cdot 10^{-3}$ is used, and the second order low-pass filter is applied every 8th time step.

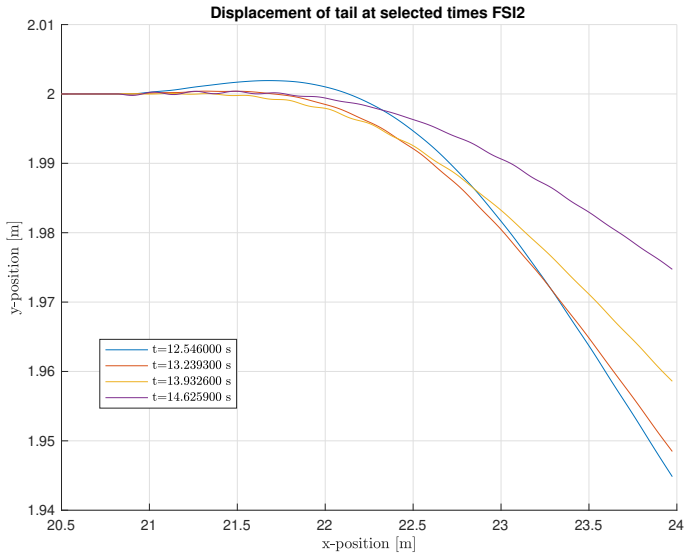

Figure 39: Displacement of plate at selected times for the FSI2 setup using the present 2nd order SBP method. A non dimensional time step of $dt' = 3 \cdot 10^{-3}$ is used and, the second order low-pass filter is applied every 8th time step.

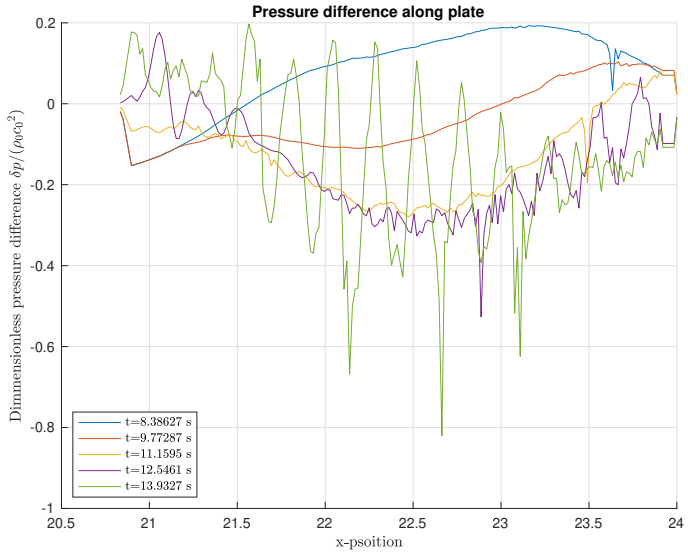

Figure 40: Dimensional pressure difference along tail for the FSI2 setup using the present 2nd order SBP method close to time of instability. A non dimensional time step of $dt' = 3 \cdot 10^{-3}$ is used, and the second order low-pass filter is applied every 8th time step.

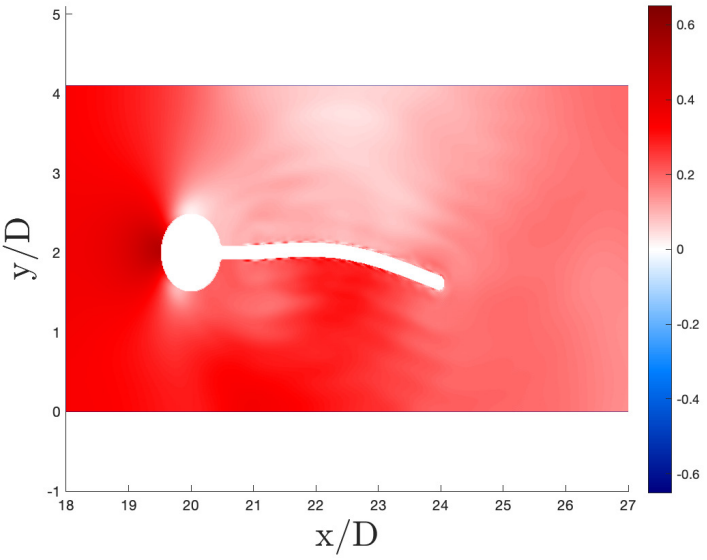

Figure 41: Pressure perturbation contours for the FSI2 setup using the present 2nd order SBP method close to time of instability. A non dimensional time step of $dt' = 3 \cdot 10^{-3}$ is used, and the second order low-pass filter is applied every 8th time step.

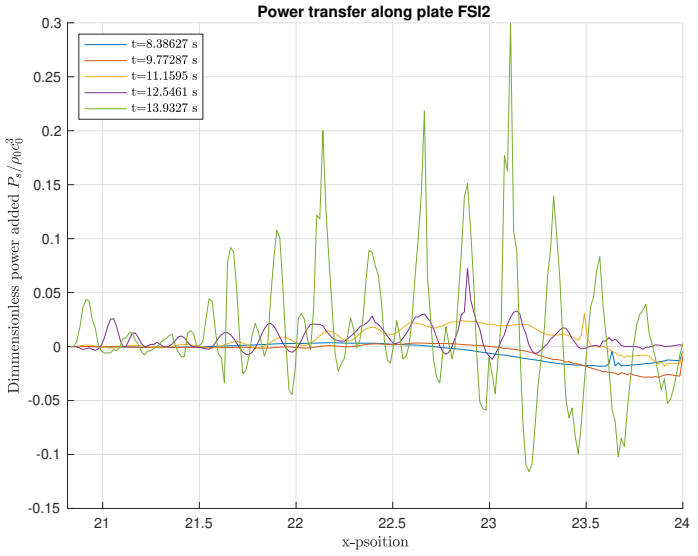

Figure 42: Non dimensional power transfer $P_s = -\delta p \dot{\phi}/(\rho_s c_0^3)$ along tail at selected times for the FSI2 setup using the present 2nd order SBP method. A non dimensional time step of $dt' = 3 \cdot 10^{-3}$ is used, and the second order low-pass filter is applied every 8th time step.

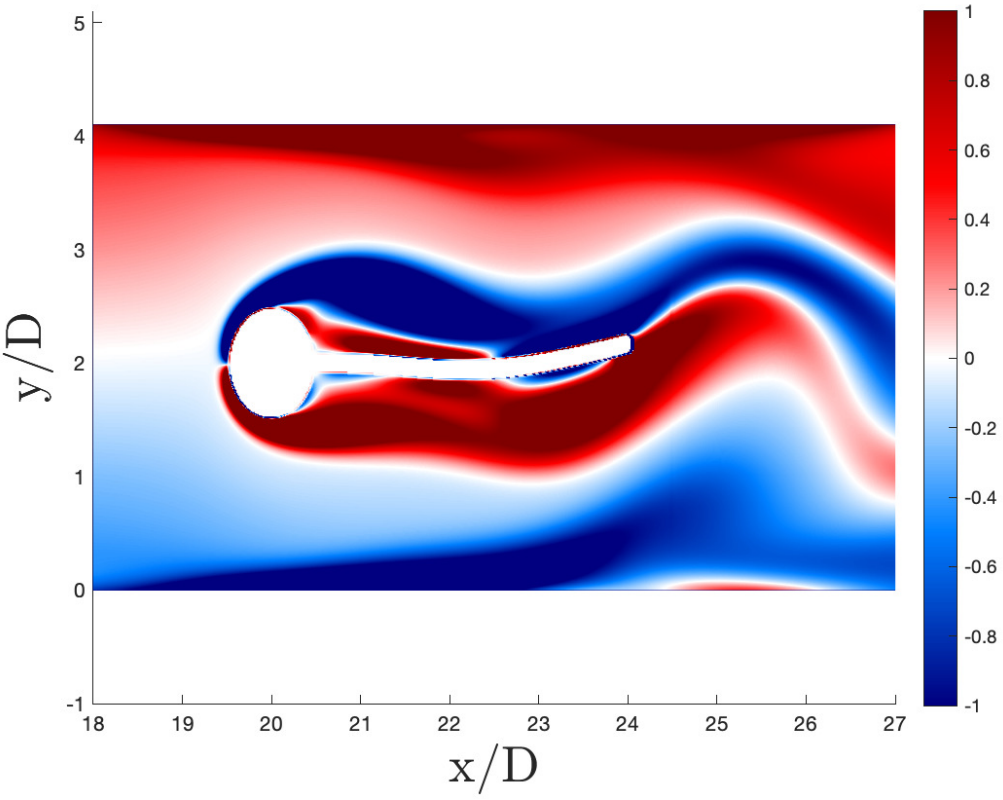

Figure 43: Instantaneous vorticity contours for the FSI2 setup using the present 2nd order SBP method close to time of instability. A non dimensional time step of $dt' = 3 \cdot 10^{-3}$ is used, and the second order low-pass filter is applied every 8th time step.

Comparing figure 40 and 39, just as for the FSI1 simulations, the onset of instability starts with pressure spikes which grow in size and numbers and create oscillations along the tail. The power transfer grows accordingly as seen in figure 42. The pressure spikes are found in the fluid domain creating pressure wiggles along the plate, and waves propagating from the plate out into the domain as seen in figure 41. In the vorticity contour plot in figure 43, the start of a vortex shedding pattern appear behind the trailing edge of the plate due to the high Reynolds number and movement of the plate. Small eddies also appears close to the plate as the instability grows and becomes unstable.

There are many sources of error which would all contribute to deviations between the present results using the ghost-point immersed boundary with the 2nd order SBP method, and the results in Turek and Hron[45]. Since the results did not converge, it is impossible to provide any quantification of what of the simplifications of beam model, solver method, and geometric assumptions done in the implementation presented in section 3.4 would have on the results, but there is room for some speculation. Even though results by Garcia [10] indicated that the Euler-Bernoulli beam model with some error could predict the displacement of the beam, the results are from a one-dimensional beam, and not one of finite thickness. Dixit [8] found that as the slenderness ratio h/L decreases, there are higher beam deflection oscillation frequencies that are not captured by the model. Also, if the beam is damaged, meaning there are cavities along the plate length, the deviation becomes larger. The circle criteria used to find points belonging to the structure might

resemble such cavities, and thereby introduce errors and contribute to the instability. When it comes to the choice of numerical method to solve the Euler Bernoulli beam equation, it is possible that the finite difference method used to approximate spatial derivatives in the plate contributes to some error. In Li et al. [23], a high frequency damping term is added to the Euler-Bernoulli beam equation to avoid spurious wavelengths.
The rounding of the tip would create a smoother flow around trailing edge and reduce the abrupt pressure difference. It is possible that the deflection would become smaller when this feature is added. The shortening of the plate by holding the first 20 joint points in place is also something that influences the result, but should not lead to instability. Simulations using different numbers of joint points were conducted during the work on this thesis, but did only show small changes in the displacement amplitude of the plate not worth further investigation.

4.3 Computations

The simulations were performed on resources provided by the NTNU IDUN/EPIC computing cluster [40]. The cluster has more than 70 nodes and 90 GPGPUs. Each node contains two Intel Xeon cores, at least 128 GB of main memory, and is connected to an Infiniband network. Half of the nodes are equipped with two or more Nvidia Tesla P100 or V100 GPGPUs. Idun's storage is provided by two storage arrays and a Lustre parallel distributed file system.

To speed up the calculations Message Passing Interface (MPI) was used. This was done by dividing the calculation domain into 9 parallel blocks. For each of these blocks a node from the EPIC/IDUN cluster was assigned. A typical simulation of the elastically mounted cylinder on a 881x521=459001 points large grid using a time step of $8 \cdot 10^3$ run to the non-dimensional time of 1200, i.e. 150000 time steps, would require a total time of approximately 12 hours to finish for the present 2nd order SBP method. A typical simulation of a flexible plate behind a cylinder using parameters corresponding to FSI1 on a $(971 \times 369) = 358299$ points large grid and a time step equal to $1 \cdot 10^3$ would take approximately 10 hours, and a simulation using parameters according to FSI2 but with a non dimensional time step of $3 \cdot 10^3$ would take the same amount of time. The computational time would then scale on the time step used, meaning that halving the time step would double the computational time.

5 Conclusions

The main goal of this master thesis was to reduce the order of the existing higher order ghost-point immersed boundary method to make it applicable on concave structures and reduce the number of ghost point layers. This was achieved by implementing a second order SBP method. The method was tested on an elastically mounted cylinder at $Re = 100$ and $Ma = 0.25$, and a flexible plate behind a cylinder at $Re = 20$ and $Ma_\infty = 0.20$, and $Re = 100$ and $Ma_\infty = 1/3$.
For the elastically mounted cylinder, the method produced good results. Cylinder displacement seemed to converge towards the results from Blackburn and Karniadakis [5] and Yang and Stern [51]. If a fine enough grid had been used, it is likely that the results would coincide better. Comparing results obtained using the higher order GPIBM, going down to second order do not seem to effect the cylinder displacement much, but the acoustic waves seem to poorly resolved. An investigation of the energy transfer between the cylinder and the flow was conducted. Results from the investigation was in accordance with the underlying physics and intuition. A study on the effect of choosing different number of time steps between each filtering was conducted. Results showed that the appropriate number of time steps between each filtering is not definite, but that every 2nd or 4th time step might be appropriate for the elastically mounted cylinder test case. The appropriate interval will depend on the wave modes present in the problem and the grid resolution. In the simulations of the flexible plate behind a cylinder test case, an instability occurred. The cause of this instability is likely errors in the implementation of the test-case, and possibly also artificial added mass effects. Since nonphysical spikes and oscillations first show up in the pressure load, the implementation error is probably in the implementation of the pressure load. Despite the instability, results seemed to converge towards the benchmark results by Turek and Hron, and are thus promising. In addition, steady state results were obtained for the FSI1 setup with a ten times higher solid-fluid density ratio.

6 Future outlooks

Some points that the author did not have time to investigate, and suggestions of topics for future work is presented here.

- Even tough the present second order SBP method for the ghost point immersed boundary method was validated on the elastically mounted cylinder test-case, a full grid convergence was not obtained. Thus, finer grids guaranteeing grid convergence should be used on the test case to have a better picture of the potential of the method.
- The method presented in this thesis did not manage to produce stable results for the flexible plate behind a cylinder test case with a parameter setup corresponding to FSI1 and FSI2 presented in 4. Since the instability could be a result of errors in the implementation of the plate model, future work should aim at providing correct results for this test-case since the plate in many ways resemble the shape of the soft palate. If an Euler-Bernoulli model is used, it is recommended that the edges of the plate is resembled by cubic splines shifted a distance $\pm h/2$ normal to the mid-line. Experiments with this were done while working on the master thesis, but there were unfortunately not enough time to produce presentable results.
- An inadequate method to find the pressure load is the most probable cause of the instabilities of the flexible plate. A method of finding the pressure load on each joint point by extrapolating the pressure at the fluid onto the interface point normal to each joint point was investigated. However, this approach also lead to instability. It is possible that the procedure was poorly implemented, thus this method is worth more investigation.
- Another plate model than the very simple Euler-Bernoulli beam model should be investigated. One option is to couple a verified finite element solver of the governing equations of the solid, but also simplifications like the Timoshenko beam model could be worth looking into. Remember that if another beam model is used, the assumption of constant cross section thickness normal to the mid line line of the beam is no longer valid. Thus splines and interface tracking needs to be used.
- If the instabilities occurring for the flexible plate is caused by the artificial added mass effect, a sub-iteration algorithm between each time step mitigating the nonphysical effects in the FSI solver should be implemented giving a strongly coupled FSI.
- The second order explicit low-pass filter used in this thesis is too dissipative and removes non dispersed wave-modes. By instead implementing a fourth order low -pass filter, only dispersed are removed. Note that if the fourth order filter is implemented, some boundary adaption is needed.
- Due to the use of non body-conforming grids, inadequate resolution is a problem for the ghost point immersed boundary method. To get better resolution without refining the whole grid, an adaptive grid refinement should be implemented for the method. This would make the method more competitive with body conforming ALE apraoches for FSI applications, and reduce computational costs.
- To guarantee the SBP property, the injection method to impose boundary conditions should be changed to Simultaneous Approximation Term method.

Bibliography

[1] Elin Aasgrav, Sverre Gullikstad Johnsen, Are Johan Simonsen, and BernhardMüller. CFD simulations of turbulent flow in the human upper airways, 2017. Proceedings of the 12th International Conference on CFD in Oil Gas, Metallurgical and Process Industries, Trondheim, Norway, May 30th - June 1st, 2017.

[2] Einar Aasli. Immersed boundary method for fluid-structure interaction, 2020. Project work NTNU, Norwegian University of Science and Technology.

[3] O. A. Bauchau and J. I. Craig. *Structural Analysis*, volume 163. Springer Netherlands, 2009.

[4] M. Berger, M. Pillei, A. Mehrle, W. Recheis, F. Kral, M. Kraxner, Z. Bardosi, and W. Freysinger. Nasal cavity airflow: Comparing laser doppler anemometry and computational fluid dynamic simulations. *Respiratory Physiology Neurobiology*, 283:103533, 2021.

[5] H. Blackburn and George Karniadakis. Two and three-dimensional simulations of vortex-induced vibration of a circular cylinder. *Proceedings of the Third (1993) International Offshore and Polar Engineering Conference*, page 715–720, 01 1993.

[6] Iman Borazjani, Lijuan Ge, and Fotis Sotiropoulos. Curvilinear Immersed Boundary Method for Simulating Fluid Structure Interaction with Complex 3D Rigid Bodies. *Journal of computational physics*, 227:7587–7620, 2008.

[7] Arnab Chaudhuri, Abdellah Hadjadj, and Ashwin Chinnayya. On the use of immersed boundary methods for shock/obstacle interactions. *Journal of Computational Physics*, 230(5):1731–1748, 2011.

[8] Akash Dixit. Single-beam analysis of damaged beams: Comparison using Euler–Bernoulli and Timoshenko beam theory. *Journal of Sound and Vibration*, 333:4341–4353, 09 2014.

[9] M. Ehsan Khalili, Martin Larsson, and Bernhard Müller. Immersed boundary method for viscous compressible flows around moving bodies. *Computers & Fluids*, 170:77 – 92, 2018.

[10] G. C. Garcia. Investigation of a fluid-structure interaction method for a flexible plate in viscous compressible channel flow, 2016. Project work. NTNU, Norwegian University of Science and Technology.

[11] R. Ghias, R. Mittal, and H. Dong. A sharp interface immersed boundary method for compressible viscous flows. *Journal of Computational Physics*, 225(1):528–553, 2007.

[12] Bertil Gustafsson. *High Order Difference Methods for Time Dependent PDE*, volume 38 of *Springer Series in Computational Mathematics*. Springer, Berlin Heidelberg, 2008.

[13] Seon M. Han, Haym Benaroya, and Timothy Wei. Dynamics of Transversely Vibrating Beams. *Journal of Sound and Vibration*, 225(5):935–988, 1999.

[14] Sverre Gullikstad Johnsen. Virtuosa - virtuell kirurgi i de Øvre luftveiene – nye løsninger for behandling av obstruktiv søvnapne, January 2021. URL: https://www.sintef.no/prosjekter/2020/virtuosa/.

[15] Ehsan Khalili. *Fluid-Structure Interaction and Immersed Boundary Method for the Compressible Navier–Stokes Equations Using High Order Methods*. PhD thesis, NTNU, 2018. URL: https://ntnuopen.ntnu.no/ntnu-xmlui/handle/11250/2486232.

[16] M Khalili, Martin Larsson, and Bernhard Müller. Interaction between a simplified soft palate and compressible viscous flow. *Journal of Fluids and Structures*, 67:85–105, 2016.

[17] Sung Kyun Kim, Yang Na, Jee In Kim, and Seung Kyu Chung. Patient specific CFD models of nasal airflow: Overview of methods and challenges. *Journal of Biomechanics*, 46(2):299–306, 2013.

[18] Woojin Kim and Haecheon Choi. Immersed boundary methods for fluid-structure interaction: A review. *International Journal of Heat and Fluid Flow*, 75:301–309, 2019.

[19] Erwin Kreyszig. *Advanced Engineering Mathematics*. Wiley, Hoboken, NJ, 10 edition, 2011.

[20] Arne Morten Kvarving. Natural Cubic Splines, 2008. Lecture notes TMA4215, Department of Mathematical Sciences Norwegian University of Science and Technology https://www.math.ntnu.no/emner/TMA4215/2008h/cubicsplines.pdf.

[21] M. Larsson. *Welcome to the OSAS page*. 2018. https://osas.no.

[22] Damien Leger, Virginie Bayon, Jean Pierre Laaban, and Pierre Philip. Impact of sleep apnea on economics. *Sleep Medicine Reviews*, 16(5):455–462, 2012.

[23] L. Li, W. D. Henshaw, J. W. Banks, D. W. Schwendeman, and A. Main. A stable partitioned FSI algorithm for incompressible flow and deforming beams. *Journal of Computational Physics*, 312:272–306, 2016.

[24] A. Lintermann, S. Schlimpert, J. H. Grimmen, C. Günther, M. Meinke, and W. Schröder. Massively parallel grid generation on HPC systems. *Computer Methods in Applied Mechanics and Engineering*, 277:131–153, 2014.

[25] Andreas Lintermann. *Application of Computational Fluid Dynamics Methods to Understand Nasal Cavity Flows*, pages 75–84. Springer International Publishing, Cham, 2020.

[26] Hongliang Liu. *Modeling and simulation of the soft palate for improved understanding of the obstructive sleep apnea syndrome.*

[27] Hong Luo, Joseph D. Baum, and Rainald Löhner. A hybrid cartesian grid and gridless method for compressible flows. *Journal of Computational Physics*, 214(2):618–632, 2006.

[28] Kun Luo, Zhenya Zhuang, Jianren Fan, and Nils Erland L Haugen. A ghost-cell immersed boundary method for simulations of heat transfer in compressible flows under different boundary conditions. *International Journal of Heat and Mass Transfer*, 92:708–717, 2016.

[29] Massimo R. Mannarino, Francesco Di Filippo, and Matteo Pirro. Obstructive sleep apnea syndrome. *European Journal of Internal Medicine*, 23(7):586–593, 2012.

[30] Claudio Mattiussi. An Analysis of Finite Volume, Finite Element, and Finite Difference Methods Using Some Concepts from Algebraic Topology. *Journal of Computational Physics*, 133(2):289–309, 1997.

[31] Rajat Mittal and Gianluca Iaccarino. Immersed boundary methods. *Annual Review of Fluid Mechanics*, 37, 2005.

[32] Bernhard Müller. High order numerical simulation of aeolian tones. *Computers Fluids*, 37(4):450–462, 2008. Turbulent Flow and Noise Generation.

[33] N. M Newmark. A method of computation for structural dynamics. journal of the engineering mechanics division. *ASCE Journal of the Engineering Mechanics Division*, 85, 1959.

[34] Charles S Peskin. Flow patterns around heart valves: A numerical method. *Journal of Computational Physics*, 10(2):252–271, 1972.

[35] Dale A. Anderson Richard H. Pletcher, John C. Tannehill. *Computational Fluid Mechanics and Heat Transfer*. 3 edition, 2013.

[36] Knut Emil Ringstad. Fluid-structure interaction in compressible viscous flows. Master's thesis, NTNU, 2018.

[37] Lennart Schneiders, Claudia Günther, Matthias Meinke, and Wolfgang Schröder. An efficient conservative cut-cell method for rigid bodies interacting with viscous compressible flows. *Journal of Computational Physics*, 311:62–86, 2016.

[38] Jung Hee Seo and Rajat Mittal. A sharp-interface immersed boundary method with improved mass conservation and reduced spurious pressure oscillations. *Journal of Computational Physics*, 230(19):7347–7363, 2011.

[39] Jörn Sesterhenn, Bernhard Müller, and Hans Thomann. On the cancellation problem in calculating compressible low mach number flows. *Journal of Computational Physics*, 151(2):597 – 615, 1999.

[40] Magnus Själander, Magnus Jahre, Gunnar Tufte, and Nico Reissmann. EPIC: An energy-efficient, high-performance GPGPU computing research infrastructure, 2019. https://www.hpc.ntnu.no.

[41] Bjørn Helge Skallerud. Virtual Surgery in the Upper Airways - New Solutions to Obstructive Sleep Apnea (VirtuOSA), 2020. URL: https://prosjektbanken.forskningsradet.no.

[42] Fotis Sotiropoulos and Xiaolei Yang. Immersed boundary methods for simulating fluid–structure interaction. *Progress in Aerospace Sciences*, 65:1–21, 2014.

[43] Magnus Svärd and Jan Nordström. Review of summation-by-parts schemes for initial–boundary-value problems. *Journal of Computational Physics*, 268:17–38, 2014.

[44] Eitan Tadmor. A review of numerical methods for nonlinear partial differential equations. *Bulletin (New Series) of the American Mathematical Society*, 49:507–554, 10 2012.

[45] Stefan Turek and Jaroslav Hron. Proposal for numerical benchmarking of fluid–structure interaction between an elastic object and laminar incompressible flow. *Fluid-Structure Interaction: Modelling, Simulation, Optimisation*, 53:371–385, 06 2007.

[46] Hasib Uddin, R M J Kramer, and C Pantano. A Cartesian-based embedded geometry technique with adaptive high-order finite differences for compressible flow around complex geometries. *Journal of Computational Physics*, 262:379–407, 2014.

[47] E. H. van Brummelen. Added mass effects of compressible and incompressible flows in fluid-structure interaction. *Journal of Applied Mechanics, Transactions ASME*, 76(2):1–7, 2009.

[48] Robert Vichnevetsky and John B. Bowles. *Fourier Analysis of Numerical Approximations of Hyperbolic Equations*. Society for Industrial and Applied Mathematics, 1982.

[49] K. Wang, A. Rallu, J.-F. Gerbeau, and C. Farhat. Algorithms for interface treatment and load computation in embedded boundary methods for fluid and fluid–structure interaction problems. *International Journal for Numerical Methods in Fluids*, 67(9):1175–1206, 2011.

[50] Frank M. White. *Viscous Fluid Flow*. McGraw-Hill, New York, 3rd edition, 2006.

[51] Jianming Yang and Frederick Stern. A simple and efficient direct forcing immersed boundary framework for fluid–structure interactions. *Journal of Computational Physics*, 231(15):5029 – 5061, 2012.

Appendix

A Schematic representation of GPIBM implementation for an elastically mounted cylinder

Below, a schematic representation of the ghost point immersed boundary method fluid-structure interaction solver for one time step of the elastically mounted cylinder test case is provided. In the schematic representation, n indicate the time step, N is the time step interval between each filtering , and m indicates the stage in the Runge-Kutta method. This means that $\hat{\boldsymbol{U}}'^{m}$ represents the solution vector at the mth stage of the RK4 procedure.

Pseudo code for classical explicit Runge-Kutta 4-stage algorithm adapted from [36]:

Set the classical Runge- Kutta stage level $m := 1$.

1: **if** $m < 4$ **then**

2: Solve the mass-spring-damper system (29) based on forces at time level $m - 1$ for the intermediate accelerations and velocities $\mathbf{k}_{m-1}$. $m = 0$ corresponds to time level n.
Move boundary according to intermediate time level m based on $\mathbf{k}_{m-1}$.

3: **else**
Find the position and velocity at time level $n + 1$ from equation (41).
Move boundary to time level n + 1.

4: **end if**

5: Determine the ghost points values u_{GP}, v_{GP}, ρ_{GP} and p_{GP} using the boundary conditions (50-53) at three layers of ghost points based on solution $\hat{\boldsymbol{U}}'^{(m)}$. The imposed no-slip velocity corresponds to the intermediate structure velocity at stage m.

6: Compute the convective fluxes ($\boldsymbol{F}'^{c}$ and $\boldsymbol{G}'^{c}$) at all fluid points. Approximate their derivatives in ξ and η direction using the 2nd order SBP operator.

7: Approximate viscous fluxes ($\boldsymbol{F}'^{v}$ and $\boldsymbol{G}'^{v}$) at all fluid and ghost points using the 2nd order SBP operator. Then approximate the derivatives of $\boldsymbol{F}'^{v}$ and $\boldsymbol{G}'^{v}$ in ξ and η direction at all fluid points using the 2nd order SBP operator.

8: Compute the residual $\boldsymbol{R}(\hat{\boldsymbol{U}}'^{(m)})$ based on the approximations of the derivatives of the convective and viscous fluxes at all fluid points.

9: Determine $\hat{\boldsymbol{U}}'^{(m+1)}$ using the classical Runge–Kutta method.

10: Apply the Navier Stokes characteristic boundary condition at inlet and outlet and apply the necessary boundary conditions at the bottom and top boundaries to determine $\hat{\boldsymbol{U}}'^{(m+1)}$ at those boundaries.

11: Set $m := m + 1$.

12: **if** $m < 5$ **then**

13: **goto** 1

14: **else**

15: Compute $\hat{\boldsymbol{U}}'^{n+1}$ at all fluid points.

16: **if** $N \mod n = 0$ **then**

17: Apply second order filter operators in ξ- and η directions at all interior fluid points.

18: **end if**

19: **end if**

B Article delivered to the ICNAAM conference

The article *Immersed Boundary Method For Fluid-Structure Interaction of Viscous Compressible Flow With an Elastically Mounted Cylinder* is under review for the 19th International Conference of Numerical Analysis and Applied Mathematics (ICNAAM).

Immersed Boundary Method For Fluid-Structure Interaction of Viscous Compressible Flow With an Elastically Mounted Cylinder

Einar Aasli[1,a),c)] and Bernhard Müller[1,b),d)]

[1]*Department of Energy and Process Engineering. Norwegian University of Science and Technology (NTNU), Trondheim, Norway*

[a)]einaaas@stud.ntnu.no
[b)]bernhard.muller@ntnu.no
[c)]www.linkedin.com/in/einar-aasli-808179205
[d)]https://folk.ntnu.no/bmuller/

Abstract. A simple but efficient immersed boundary method for simulating fluid structure-interaction problems of viscous compressible flow is validated for an elastically mounted cylinder in a compressible free-stream flow of Reynolds number $Re = 200$ and Mach number $Ma = 0.25$. The elastically mounted cylinder is modelled as a mass-spring-damper-system, resulting in a second order differential (ODE) equation for the structure. Its displacement is investigated. The second order summation by parts (SBP) method is used to approximate the spatial derivative in the compressible Navier-Stokes equations governing the behaviour of the fluid. Time integration in both the structural and the fluid equations is preformed using the classic fourth order Runge-Kutta method (RK4). The fluid-structure coupling happens through the position and velocity of the structure boundary imposed on the fluid and the force of the fluid imposed on the structure. The boundary is moved in each RK4 stage.

INTRODUCTION

Numerical simulations of fluid structure interaction (FSI) have proven to be useful in fields ranging from aerodynamics to biomedical flows. In the Arbitrary Lagrangian-Eulerian (ALE) approach for FSI, the fluid flow described in a Eularien frame of reference is coupled to the structure described in a Lagrangian frame of reference through a body conforming grid. However, this approach requires re-meshing for each time-step, which is time consuming and difficult for advanced geometries and large deformations [8]. Immersed Boundary Methods (IBM) are an alternative approach for FSI problems where the solid moves and deforms on stationary Cartesian background grid, omitting the re-meshing process [8]. Summation by parts (SBP) methods are a group of finite difference methods that guarantee stability. In this paper, a higher order ghost point immersed boundary method (GPIBM) developed by Khalili te al. [3] is reduced to a second order SBP method to allow the interaction with non-convex structures. The second order method is first tested here for oscillations of an elastically mounted cylinder in a compressible flow at Reynolds number $Re = 200$ and Mach number $Ma = 0.25$. The cylinder is attached to a spring and a damper, and its displacement can be described by a mass-spring-damper system.

GOVERNING EQUATIONS

Compressible Navier-Stokes equation

The two dimensional compressible Navier-Stokes equations are solved in a non-dimensional perturbation form. The vector $\boldsymbol{U}'(= [\rho', (\rho u)', (\rho v)'(, (\rho E)']^T$ contains the variables solved for. Here, $\rho' = \frac{\rho - \rho_0}{\rho_0}$ is the non-dimensional perturbation density, $(\rho u)' = \frac{\rho u}{\rho_0 c_0}$ is the non-dimensional perturbation momentum density in x-direction, $(\rho v)' = \frac{\rho v}{\rho_0 c_0}$

is the non-dimensional perturbation momentum density in y-direction, and $(\rho E)' = \frac{\rho E - \rho_0 E_0}{\rho_0 E_0}$ is the non-dimensional perturbation total energy density. ρ_0 and c_0 are the stagnation density and the stagnation speed of sound, respectively. The position vector in non-dimensional Cartesian coordinates is $\boldsymbol{x} = (x/D, y/D)^T$, and non dimensional time is $t' = \frac{tc_0}{D}$, where D is the cylinder diameter [3]. Letting bold symbols denote vectors, the compressible non dimensional Navier-Stokes euqations can then be written in the perturbation flux form [3]:

$$\boldsymbol{U}'_t + \boldsymbol{F}^{c\prime}{}_x + \boldsymbol{G}^{c\prime}{}_y = \boldsymbol{F}^{v\prime}{}_x + \boldsymbol{G}^{v\prime}{}_y, \tag{1}$$

where $\boldsymbol{F}^{c\prime}$, and $\boldsymbol{G}^{c\prime}$ are the non dimensional inviscid perturbation flux vectors in the x- and y-directions respectively, and $\boldsymbol{F}^{v\prime}$, and $\boldsymbol{G}^{v\prime}$ are the non dimensional viscous perturbation flux vectors in the x- and y-directions respectively. Assuming the fluid is air as an ideal gas, the ratio of specific heats and Prandtl number are constants and equal to $\gamma = \frac{c_p}{c_v} = 1.4$ and $Pr = 0.72$ respectively. The viscous stress stress tensor τ_{ij} follows the constitutive law of a Newtonian fluid, where the dynamic viscosity μ is temperature dependent and varies according to Sutherland's law [3]. Transformed coordinates are used to allow grid stretching away from the center Cartesian grid block with the immersed boundary. A detailed description can be found in the PhD thesis by Khalili [3].

Mass-spring-damper system

The GPIBM is tested for a cylinder attached to a spring and damper in a flow-field. The cylinder is allowed to move in x- and y-directions. Its displacement is described by the following second order ordinary differential equation (ODE):

$$\ddot{q} + 2\zeta\left(\frac{2\pi}{U^*}\right)\dot{q} + \left(\frac{2\pi}{U^*}\right)^2 q = \frac{2}{\pi m^*} c_{D,L}(t), \tag{2}$$

where $q = [x_c/D, y_c/D]^T$ is the non-dimensional cylinder displacement, $\dot{q} = \frac{\partial q}{\partial t}$, $\ddot{q} = \frac{\partial^2 q}{\partial t^2}$ and $C_{D,L}$ denotes the vector with the drag and lift coefficients. The other parameters are the non dimensional damping $\zeta = \frac{b}{2\sqrt{km_s}}$, the dimensionless mass $m^* = \frac{\rho_s}{\rho_f}$, the dimensionless free stream velocity $U^* = \frac{U}{f_N D}$. These parameters can be derived from: the mass of the cylinder $m_s = \rho_s D^2/4$, the spring stiffness k ,the damping coefficient b, and the natural frequency of the system $f_N = \frac{1}{2\pi}\sqrt{\frac{k}{m}}$. x and y are non-dimensionalized by the cylinder diameter D and the time t by D/U, giving q and its time-derivatives. Subscript s and f indicate solid and fluid properties. The second order ODE in equation (2) can be rewritten into a set of first order ODEs:

$$\dot{\mathbf{Q}} = \mathbf{G}(t, \mathbf{Q}). \tag{3}$$

DISCRETIZATION

Ghost Point Immersed Boundary Method

The ghost point immersed boundary method developed by Khalili et al. [4], [3] is employed. In this method, the governing equations of the fluid are discretized using a finite difference method on a Cartesian grid. Each grid-point in the computational domain are divided into three categories as illustrated in Fig. 1. First, fluid and solid points are flagged on the basis of which side of the immersed boundary they are located. Then, solid points that are so close to the immersed boundary that they are inside the computational stencil of any of the fluid points adjacent to the immersed boundary are flagged as ghost points (GP). In the present simulation, only one layer of ghost points is used, hence all solid points with at least one fluid point neighbor are flagged as ghost points. The solid's effect on the fluid is imposed through these ghost points by utilizing the boundary conditions to set fluid

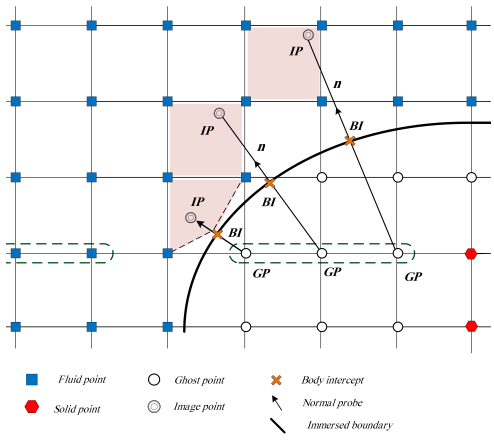

FIGURE 1: Illustration of boundary intersection [3]

properties on them. The process is illustrated ion Fig. 1. A normal probe is extended from each ghost point through the boundary intersection point (BI). By reflecting the ghost point about BI, the image point (IP) is found. Any variable at the IP is found through bilinear interpolation either by using four surrounding fluid points, or by a mix of fluid points and boundary intersection points. The fluid velocities are found through imposing the no-slip boundary condition $(u, v) = \boldsymbol{U}_{wall}$ at BI. Letting u and v be represented a variable ϕ, the following equation for ϕ_{GP} is derived: $\phi_{GP} = 2\phi_{BI} - \phi_{IP}$.

Assuming adiabatic wall condition for the temperature and the boundary layer approximation for the pressure, the Neumann boundary conditions $\frac{\partial T}{\partial n} = 0$ and $\frac{\partial p}{\partial n} = 0$, where n denote the normal direction along the normal probe, need to be fulfilled at BI. For the general Neumann condition $\frac{\partial \phi}{\partial n} = \beta$, this corresponds to: $\phi_{GP} = \phi_{IP} \cdot \Delta l - \beta$, where Δl is the distance between the image point and ghost point. A more detailed description of the method is found in Khalili et al. [4], [3]

Since the cylinder is a rigid body, the fluid-structure coupling is employed through the force acting on the interface from the fluid. This force is $\begin{pmatrix} F_D \\ F_L \end{pmatrix} = \oint_{\partial\Omega} -p\delta_{ij}n_j + \tau_{ij}n_j dA$. This integral is approximated using the trapezoidal rule in polar coordinate around the immersed boundary.

Numerical Methods

Numerical Solution of Compressible Navier-Stokes Equations

The second order SBP method is used to approximate the derivative in the compressible Navier-Stokes equation described in equation (1) [2]. This methods uses a second order central difference approximation in the interior, and a first order one sided difference at the boundaries. If proper boundary conditions (BCs) are employed for the SBP methods, stability is guaranteed by the energy method [2]. The injection method is used to impose the in- and outflow BCs [3]. In the approximation of the viscous terms $\boldsymbol{F}^v{}_x$ and $\boldsymbol{G}^v{}_y$, the central difference method needs to be applied twice. However, this approximation of the viscous term does not dampen waves of wave-number $k = \frac{\pi}{h}$, where h is the grid spacing [5]. To remove these wavelengths, a second order explicit filter is employed every 2nd time step [5]. The time integration is done by using the classic fourth order explicit Runge-Kutta (RK4) method described below for the mass-springer-damper system.

Numerical solution of mass-spring-damper system

The system of ODEs in equation (2) is also solved using the RK4 method. Let Δt denote a full time step The intermediate time step vector then reads $[\Delta t_1, \Delta t_2, \Delta t_3, \Delta t_4]^T = [0, \Delta t/2, \Delta t/2, \Delta t]^T$. Each stage is then evaluated by $\mathbf{k}_m = \mathbf{G}(t^n + \Delta t_m, \mathbf{Q}^n + \mathbf{k}_{m-1}\Delta t_m), \{m = 1, 2, 3, 4\}$. Here, $\mathbf{k}_1$ corresponds to the acceleration and velocity at time t^n, i,e., $\dot{\mathbf{Q}}^n$. From the Runge-Kutta stages, the solution at the new time level is then calculated by: $\mathbf{Q}^{n+1} = \mathbf{Q}^n + \Delta t\left(\frac{1}{6}\mathbf{k}_1 + \frac{1}{3}\mathbf{k}_2 + \frac{1}{3}\mathbf{k}_3 + \frac{1}{6}\mathbf{k}_4\right)$. The Runge-Kutta method of the fluid and the mass-springer-damper system is solved in parallel, meaning that for each stage, the immersed boundary is moved and new values are calculated at the fluid and ghost points.

RESULTS

The simulations were conducted on a $90D$ long and $40D$ wide domain, with symmetry boundary conditions at the lower and upper boundaries. A 1044x646 large grid was used. The cylinder was initially placed at the point $(x_0, y_0) = (20D, 20D)$. Around the cylinder a grid Cartesian grid of spacing $\Delta x = \Delta y = 2D/125$ was used. The non-dimensional structural parameter were set to $m^* = \frac{\pi}{4}$, $\zeta = 0.01$ and $U_* = 5$. The cylinder was held in place until non-dimensional time $t' = 520$ to obtain a fully developed flow field upon release. The time-step was set to $\Delta t' = 8 \cdot 10^{-3}$, which resulted in a maximum CFL number equal to $CFL = 0.61$. The present results are compared with those of Yang and Stern [9], Blackburn and Karniadikis [1], and Rngstad [6]. Ringstad conducted simulations with the same GPIBM with a globally fourth order SBP method that uses a sixth order central difference approximation in the interior. Looking at the left part of Fig. 2, it can be seen that the shape of the trajectory is very similar to that of the 6th order method.

The displacement and velocity in y-direction seem to match well with the completely coinciding velocity phase plots obtained by the 6th order SBP method and Yang and Stern [9]. The crossing point x_c is the displacement at the point where the trajectory crosses itself. Blackburn and Karniadakis obtained a displacement $x_c = 0.62D$, Yang and Stern [9] $x_c = 0.651D$ and Ringstad $x_c = 0.616D$, while the present obtained $x_c = 0.60D$. Comparing x_c and velocity phase plots in x-direction to the references, the x-displacement seems to be under predicted. When it comes to the Strouhal number (Str), Yang and Stern [9] obtained $Str = 0.187$, and Ringstad [6] $Str = 0.1755$, while the present method obtained $Str = 0.1755$. The lower x-displacement and strouhal number is thought to be a result of insufficient grid resolution.

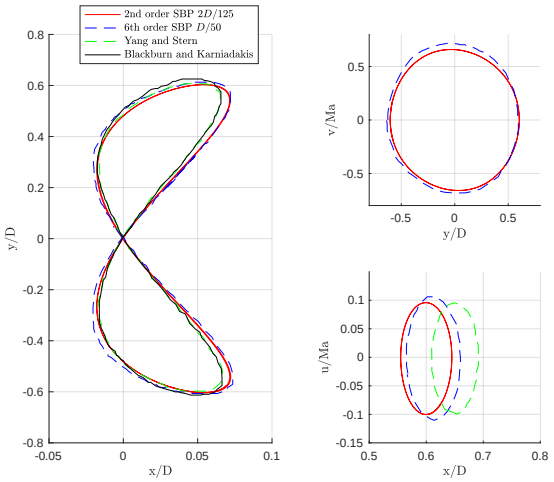

FIGURE 2: Comparison of cylinder trajectory (left plot), and cylinder velocity components phase plots (right plots). Red solid line: Present 2nd order method. . Blue dashed line: 6th order SBP [6] method on a 881x521 grid with a $D/50$ grid spacing close to the cylinder. Green dashed line: Yang and Stern [9] results on a fine grid. Black dashed line: Blackburn and Karniadakis [1]. Waves in the reference plots are due to the plot extraction tool used.

CONCLUSIONS

The present ghost point immersed boundary method with a second order summation by parts approximation has been validated on the FSI problem elastically mounted circular cylinder in freestream flow at Reynolds number 200 and Mach number 0.25. Although finer grids are needed compared with the higher order GPIBM by Khalili et al. [3], the present second order GPIBM only needs one layer of ghost points and can also be applied to FSI of non-convex structures.

Acknowledgments

The authors acknowledge being allowed to use Knut Emil Ringstad's code for higher order IBM as a pattern. The help by senior engineer Jan Christian Meyer at the NTNU HPC group in running the present code on the cluster Idun [7] at NTNU has been appreciated.

REFERENCES

[1] Hugh. Blackburn and George Karniadakis. Two and three-dimensional simulations of vortex-induced vibration of a circular cylinder. *Proceedings of the Third (1993) International Offshore and Polar Engineering Conference*, page 715–720, 01 1993.

[2] Bertil Gustafsson. *High Order Difference Methods for Time Dependent PDE*, volume 38 of *Springer Series in Computational Mathematics*. Springer Berlin Heidelberg, 2008.

[3] Ehsan Khalili. *Fluid-Structure Interaction and Immersed Boundary Method for the Compressible Navier–Stokes Equations Using High Order Methods*. PhD thesis, NTNU, 2018.

[4] Ehsan Khalili, Martin Larsson, and Bernhard Müller. Immersed boundary method for viscous compressible flows around moving bodies. *Computers Fluids*, 170:77–92, 2018.

[5] Bernhard Müller. High order numerical simulation of aeolian tones. *Computers Fluids*, 37(4):450–462, 2008.

[6] Knut Emil Ringstad, M Khalili, and Bernhard Müller. High Order Immersed Boundary Method for Fluid-Structure Interaction of Viscous Compressible Flow with a Rigid Body. pages 184–191, 2020.

[7] Magnus Själander, Magnus Jahre, Gunnar Tufte, and Nico Reissmann. EPIC: An Energy-Efficient, High-Performance GPGPU Computing Research Infrastructure. *arXiv:1912.05848 [cs]*, December 2019.

[8] Fotis Sotiropoulo and Xiaolei Yang. Immersed boundary methods for simulating fluid–structure interaction. *Progress in Aerospace Sciences*, 65:1–21, 2014.

[9] Jianming Yang and Frederick Stern. A simple and efficient direct forcing immersed boundary framework for fluid–structure interactions. *Journal of Computational Physics*, 231(15):5029 – 5061, 2012.

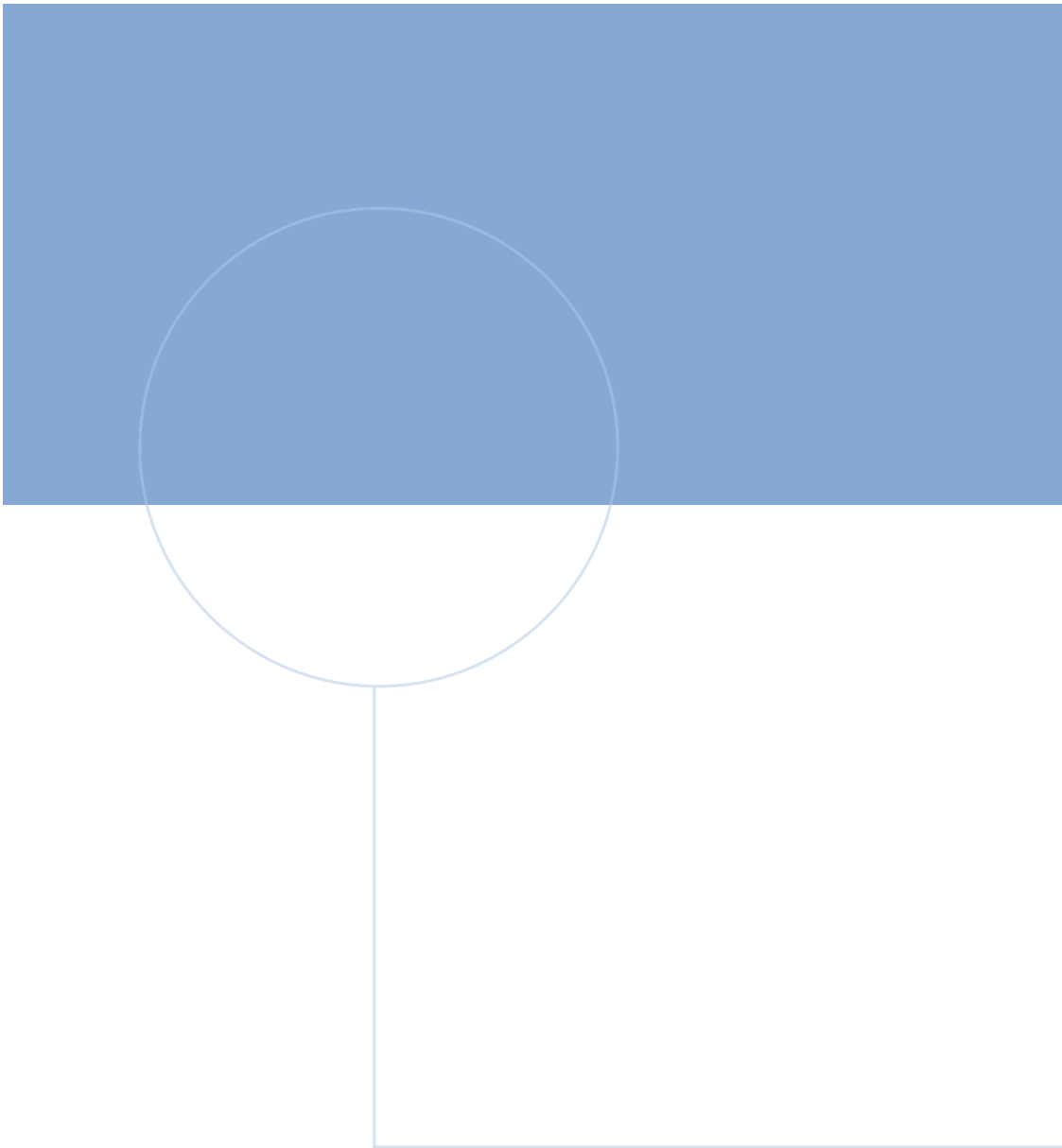

NTNU

Norwegian University of
Science and Technology